UNIVERSITY OF CALIFORNIA SAN DIEGO

Probing Hydroxyl Radical Reactions Using Photoelectron-Photofragment Coincidence Spectroscopy

A dissertation submitted in partial satisfaction of the requirements for the degree
Doctor of Philosophy

in

Chemistry

by

Yanice Benitez

Committee in charge:

Professor Robert E. Continetti, Chair
Professor Alison L. Coil
Professor Elizabeth A. Komives
Professor Kimberly A. Prather
Professor John Weare

2020

The Dissertation of Yanice Benitez is approved and it is acceptable in quality and form for publication on microfilm and electronically:

_____

_____

_____

_____

_____

Chair

University of California San Diego

2020

DEDICATION

Para mis abuelitas

Lourdes Gonzalez Bacelar Nuñez y Maria Guadalupe Hernandez Izquierdo

TABLE OF CONTENTS

LIST OF FIGURES

LIST OF TABLES

ACKNOWLEDGEMENTS

Many people in my life played an important role throughout my educational career. Of these notable people, my advisor, Bob Continetti, has provided me with a lot of guidance throughout the years, and I thank him for the opportunity to do research in his lab. It has been a great privilege to learn from him and to have the opportunity to work on interesting and complicated experimental apparatuses. His troubleshooting abilities are unmatched, and I am definitely a much better scientist because of his mentorship. I will always appreciate his patience with me and the many fruitful discussions. I will miss the happy hours and the group parties, and I will always look fondly at our experience in Israel with Kim!

The Continetti lab members (past and present) became like my SD family these past few years. Members that I overlapped with include Amelia Ray, Rico Otto, Brian Adamson, Michelle Mezher, Katherine Nadler, Daoling Huang, and Ashley Shin and they were all great resources and always willing to extend some of their expertise. When I joined the lab, I worked closely with the senior graduate student, Ben Shen, as he was coupling COAT to Machine C. Ben was a great mentor and made the late nights fun—although I haven't been able to eat Rubio's tacos since then. I look forward to future brunch hangouts when we're all in the same town (after the pandemic). Katharine Lunny and Morgan Miller were from my cohort and I've appreciated learning and growing alongside them. They were also great resources and made lab more entertaining. Katharine and I worked closely on Machine C and throughout the years we developed a great friendship and learned how to work well together. She always gave me inspiration when I needed it most, and I cannot imagine working with anyone else on Machine C. I appreciated the side office chats with Jemma Gibbard and Lunny especially when I wanted a *brief* distraction. Jemma was very kind and immensely helpful in troubleshooting or data analysis. I am glad that we crossed

paths and were able to experience so many beautiful national parks together. I'd also like to thank Joseph Taulane, the lab project scientist, for his mentorship throughout the years and his wealth of knowledge and experience. I will miss being able to run over to his desk and bug him for his help and assistance. For the current group members, Austin Parsons, Eleanor Castracane, Pyeongeun Kim, and Sally Burke, I wish you all the best and I know you will all persevere past this pandemic (PK try to organize fun lab outings when it's safe to do so!).

I would like to thank all of my collaborators these past few years and people throughout the department. Dandan Lu, Hua Guo, and Jun Li provided some excellent theoretical contributions on my 1st first author paper on PPC studies on the OH-CH_4 complex and it was a great collaboration. Thanh Nguyen and John Stanton have also provided some high-level coupled-cluster calculations on $CH_3O^-(H_2O)$ which was important in helping us further interpret our PPC studies on the OH + CH_3OH reaction. I appreciate how promptly our theory collaborators respond to our inquiries and our useful discussions. Yishai Albeck and Daniel Strasser were also great collaborators throughout the years. I appreciate Prof. Strasser's drive for fundamentally understanding any problem and his guidance on the preliminary pump-probe experiments. In the department, I'd like to thank Carmen Alfaro for helping me book my travel and registrations for various conferences. I always enjoyed stopping by to chat about a wide range of topics, especially when I needed time away from the machine. I'd also like to thank everyone at the machine shop, especially Don, Bob, and Luke for always coming through during stressful emergency moments. Out of the department, Mike Godkin from Clark-MXR was a great help in fixing our laser one too many times. His help during troubleshooting sessions was much appreciated.

Of course, I need to thank all my family and friends for supporting me throughout graduate school in so many ways. My mom and dad have always been supportive of me and I appreciate

the freedom they gave me to explore my interests and figure it out. I'm glad I was never too far away from them. My mom served the role not just as my parent but as one of my best friends. My sister, brother, nieces, and nephew always brought joy into my life, and I can't wait to live close by again so we can hang out more. I appreciate my siblings always keeping it real with me and the ease at which we can argue but still respect each other. My San Diego family, tía Rosy, Josabet, Allie, Betsy, Karen, Josue, and Ricky have made my time in SD extra special, and I love how close we have become these past 6 years. I've loved going over to my tía Rosy's house to cook empanadas, gorditas, tamales, chileatole, and all the yummy Mexican food you can think of. Cooking with my family was such an important part of my time in SD, and I am definitely a much better cook coming out of graduate school than I was coming in. Of course, my abuela Lupe and abuela Lourdes were pivotal to my early childhood education and upbringing. I would not be where I am today if it were not for them, and I am eternally grateful that they were my abuelitas. I've also appreciated going through graduate school with my Matt. He made graduate school more fun and was always there for me during my many moments of high stress. I'm so thankful we found each other, what are the odds? I'd also like to thank some notable friends who have helped me in many ways throughout my educational career so far, they include Karla Gomez, Monica Lopez, Jorge Chairez, Franklin De Paz, Karla Chamarro, Allie Chen, Pauline Olsen, Sebastian Val, and Chris Campos. Lastly, but definitely not least, I need to thank my little dog, Peanut. He has absolutely no idea how much he has meant to me these past 12 years, but I'm so thankful that he was with me through my whole education from finishing high school, to undergrad, to grad school. I am fortunate that I had a little friend with me every step of the way.

Chapter 3 is a reprint of the material as it appeared in Benitez, Y.; Lu, D.; Lunny, K. G.; Li, J.; Guo, H.; Continetti, R. E., Photoelectron-Photofragment Coincidence Studies on the Dissociation Dynamics of the OH-CH_4 Complex, *J. Phys. Chem. A* **2019**, 123(23), 4825-4833. Some of the supplemental figures were incorporated into the text. The dissertation author is the primary author. The corresponding authors are the dissertation advisor, R. E. Continetti, and Jun Li.

Chapter 4 is in preparation for publication: Benitez, Y.; Parsons, A. J.; Lunny, K. G.; Continetti, R. E., Dissociation Dynamics of the $OH^-(C_2H_4)$ Complex. The dissertation author is the primary author. The corresponding author is the dissertation advisor, R. E. Continetti.

Chapter 5 is in preparation for publication: Benitez, Y.; Nguyen, T. L.; Parsons, A. J.; Stanton, J. F.; Continetti, R. E., Probing the Exit Channel of the $OH + CH_3OH \rightarrow H_2O + CH_3O$ Reaction by Photodetachment of $CH_3O^-(H_2O)$ Complex. The dissertation author is the primary author. The corresponding author is the dissertation advisor, R. E. Continetti.

VITA

2008-2012 Associate of Science, Santa Monica College

2012-2014 Bachelor of Science, University of California Davis

2014-2020 Research Assistant, University of California San Diego

2016 Master of Science, University of California San Diego

2020 Doctor of Philosophy, University of California San Diego

PUBLICATIONS

Benitez, Y.; Parsons, A. J.; Lunny, K. G.; Continetti, R. E., "Dissociation Dynamics of the $OH^-(C_2H_4)$ Complex," *In preparation*.

Benitez, Y.; Nguyen, T. L.; Parsons, A. J.; Stanton, J. F.; Continetti, R. E., "Probing the Exit Channel of the $OH + CH_3OH \rightarrow H_2O + CH_3O$ Reaction by Photodetachment of $CH_3O^-(H_2O)$ Complex." *In preparation*.

Benitez, Y.; Lu, D.; Lunny, K. G.; Li, J.; Guo, H.; Continetti, R. E., "Photoelectron-Photofragment Coincidence Studies on the Dissociation Dynamics of the $OH\text{-}CH_4$ Complex," *Journal of Physical Chemistry A* 2019, 123, 23, 4825; https://doi.org/10.1021/acs.jpca.9b02441

Shen, B. B.; Lunny, K. G.; Benitez, Y.; Continetti, R. E., "Photoelectron-Photofragment Coincidence Spectroscopy with Ions Prepared in a Cryogenic Octopole Accumulation Trap: Collisional Excitation and Buffer Gas Cooling." *Frontiers in Chemistry*, 2019, 7, 295; https://doi.org/10.3389/fchem.2019.00295

Albeck, Y.; Lunny, K. G.; Benitez, Y.; Shin, A. J.; Strasser, D.; Continetti, R. E., "Resonance-Mediated Below-Threshold Delayed Photoemission and Non-Franck-Condon Photodissociation of Cold Oxyallyl Anions," *Angewandte Chemie International Edition*, 2019, 58, 5312; https://doi.org/10.1002/anie.201900386

Lunny, K. G.; Benitez, Y.; Albeck, Y.; Strasser, D.; Stanton, J. F.; Continetti, R. E., "Spectroscopy of Ethylenedione and Ethynediolide: A Reinvestigation," *Angewandte Chemie International Edition*, 2018, 57, 5394; https://doi.org/10.1002/anie.201801848

Shen, B. B.; Benitez, Y.; Lunny, K. G.; Continetti, R. E., "Internal Energy Dependence of the Photodissociation Dynamics of O_3^- Using Cryogenic Photoelectron-Photofragment Coincidence

Spectroscopy," *The Journal of Chemical Physics*, 2017, 147, 094307; https://doi.org/10.1063/1.4986500

FIELDS OF STUDY

Major Field: Physical Chemistry

Studies in Physical Chemistry
Professor Cheuk-Yiu Ng and Professor William M. Jackson, University of California, Davis

Studies in Physical Chemistry
Professor Robert E. Continetti, University of California, San Diego

ABSTRACT OF THE DISSERTATION

Probing Hydroxyl Radical Reactions Using Photoelectron-Photofragment Coincidence Spectroscopy

by

Yanice Benitez

Doctor of Philosophy in Chemistry

University of California San Diego, 2020

Professor Robert E. Continetti, Chair

The hydroxyl radical plays a critical role in several contexts including combustion, atmospheric chemistry, and low-temperature extraterrestrial environments. OH has been observed in the interstellar medium and is important in the gas phase chemistry of interstellar clouds. Additionally, the hydroxyl radical is the dominant oxidizer of volatile organic compounds in the atmosphere. Here, the reactions between OH and simple alkanes, alkenes, and alcohols were investigated as these bimolecular reactions can expand fundamental understanding of gas phase reaction dynamics.

Photoelectron-photofragment coincidence (PPC) spectroscopy was used to characterize the energetics and dynamics of the $OH + CH_4 \rightarrow H_2O + CH_3$ reaction initiated by photodetachment of the $OH^-(CH_4)$ anion complex. PPC measurements at a photon energy of 3.20 eV yielded stable and dissociative channels. Interpretation of the experimental results was supported by quantum chemistry and quasiclassical trajectory calculations showing that most of the trajectories yield slowly recoiling $OH + CH_4$ reactants while some are trapped in the entrance channel van der Waals well.

Extending the study to hydroxy radical reactions with the simplest alkene, ethylene, yielded similar dissociative photodetachment dynamics (DPD) to PPC studies on $OH^-(CH_4)$. The dominant channel was DPD to $OH + C_2H_4 + e^-$ with a low kinetic energy release (KER) of the dissociating fragments, consistent with weak repulsion between the $OH + C_2H_4$ reactants near the transition state. To model the DPD process, an impulsive model was used to account for rotational energy partitioning in C_2H_4 photofragments and showed good agreement with the experimental results.

PPC studies probing the $OH + CH_3OH \rightarrow H_2O + CH_3O$ reaction had the best Franck-Condon overlap with the exit channel. High-level coupled cluster calculations of the stationary points on the anion surface show that $CH_3O^-(H_2O)$ is the stable minimum. Photodetachment leads to $H_2O + CH_3O + e^-$ products with both direct dissociative photodetachment as well as resonance mediated processes observed on the neutral surface. The partitioning of total kinetic energy in the system indicates that water stretch and bend excitation is induced in DPD, and evidence for long-lived complexes consistent with production of vibrational Feshbach resonances in the exit channel is reported.

Chapter 1: Introduction

1.1. Background

Gas phase reaction dynamics is one of the oldest fields in molecular physics and physical chemistry and has been a growing field for the past 90 years.[1-3] The advent of the vacuum pump in the early 1900s was a key invention which led to the development of the first molecular beam or "molecular rays" in 1911 by Dunnoyer—thus began a revolution in 20th century physics and chemistry leading to the first measurement of the Maxwell speed distribution, by Stern, proving the kinetic theory of gases, and the notable Stern-Gerlach experiments, which provided the first discrete measurement of the component of the intrinsic spin angular momentum of an electron.[4, 5] Of course, many important experiments followed which will not be discussed here, but one of the most significant consequences in chemistry was the ability to understand fundamental processes occurring on an atomic or molecular level. Aside from other insights, employing molecular beam methods helped to elucidate fundamental processes involving the dynamics and mechanisms of elementary reactions.[4, 6] This was a huge breakthrough in beginning to understand the signatures of various gas phase species interacting with other species by means of collisions.[7] For the first time, key observables from these small transient species were being measured including reaction rate coefficients, product energies, and branching ratios.

These observables continue to be important in understanding fundamental reaction dynamics. In chemistry, we are interested in controlling reactions and understanding the mechanisms by which they occur. Considering seemingly simple questions: what happens when you break a bond, what makes molecules "wiggle", or what the potential energy landscape is for various reactions, enables rigorous study of reaction dynamics of transient species. It follows that the most important regions of a reaction surface are the transition state and those reactive

intermediates that are short-lived due to the nature of their chemical stability (on the order of a vibrational period or less) and are often difficult to study.

The interplay between experiment and theory continues to expand our understanding of elementary reactions especially as we move towards studying increasingly complex systems with more degrees of freedom.[8, 9] As such, growth in this field is driven by the direct and quantitative comparisons between experiment and theory. For a bimolecular reaction, the nuclear dynamics can be described by the Born-Oppenheimer (BO) approximation which separates electronic and nuclear motion. This approach results in a BO potential energy surface (PES) which serves as a foundation for understanding reaction dynamics even when the BO approximation breaks down near electronic degeneracies (non-adiabatic effects).[10, 11] Advances in electronic structure theory and the fitting of *ab initio* electronic structure points has made it possible to construct highly accurate global PESs for many body systems with 3N-6 degrees of freedom (where N is the number of atoms in a chemical system).[12, 13] Additionally, advances in computing power has contributed to the growth of quantum dynamical approaches making full quantum dynamics calculations possible.[14-17] The dissociation dynamics for these systems with more degrees of freedom represents a significant challenge for theory and carrying out meaningful experiments help to provide further benchmarks for studying increasingly complex reactions.

Understanding elementary or bimolecular reactions is imperative to understanding the world around us. Radical-molecule and ion-molecule reactions play an essential role in understanding both atmospheric and combustion chemistry.[18, 19] The complexities in combustion chemistry lead to significant insight into the chemistry occurring in flames and the most important reactive intermediates and products involved.[20] It is also important in understanding climate change through evaluation of the chemical reactions that occur in the various layers of our

atmosphere under different energy regimes. One of the dominant radical species in the atmosphere is the short-lived hydroxyl radical, OH. The highly reactive hydroxyl radical initiates photo-oxidation in the troposphere and is an important carrier in combustion processes.[19] Namely, the reactions between OH with methane, CH_4, ethylene, C_2H_4, and methanol, CH_3OH are of interest and will be discussed further in the chapters that follow. For now, we shift our focus to our approach in probing the dynamics of these systems.

1.1.1. Hydroxyl Radical Reactions

The hydroxyl radical plays a critical role in reactions involving volatile organic compounds in combustion, atmospheric chemistry, as well as in low-temperature extraterrestrial environments.[19, 21] OH has also been observed in the interstellar medium and is thought to be important in the gas phase chemistry of interstellar clouds.[22] As a result, the reactions between OH and simple alkanes, alkenes, or alcohols have been studied both experimentally and theoretically and were investigated in this research program. These reactions are representative of radical-molecule reactions that form a weakly bound complex, or van der Waals complex (vdW), without an energy barrier. Weakly bound vdW complexes are a class of reactive intermediates that are difficult to study and finding ways of capturing their dynamics is of key interest.

In the case of the neutral reactions of OH + CH_4/C_2H_4, the major pathway at low temperatures is dominated by electrophilic addition of OH with the hydrogen oriented towards the tetrahedral face of CH_4 or the π bond of C_2H_4, respectively. At higher temperatures, the vdW complex can either dissociate to the reactant channel OH + CH_4/C_2H_4 or it can proceed to the product channel through hydrogen abstraction (C_2H_4 can also isomerize). The dissociation dynamics of these systems will be discussed in Chapters 3 and 4. The reaction OH + $CH_3OH \rightarrow H_2O + CH_3O$ differs slightly in that the pre-reactive complex helps to facilitate quantum

mechanical tunneling through the H-abstraction barrier leading to the product channel, H_2O + CH_3O—an unexpected and surprising result which has inspired many experimental and theoretical studies in recent years.[23] Our approach to study this reaction resulted in probing the exit channel products and will be discussed in Chapter 5.

1.1.2. Experimental Techniques for Studying Hydroxyl Radical Reaction Dynamics

Radicals and reactive intermediates are short-lived complexes, with the hydroxyl radical having a lifetime of < 1 second in the Earth's atmosphere[24] thus making it difficult to study and produce in the free state.[25] If unperturbed by collisions, radicals do not spontaneously decompose, therefore studying these species in a vacuum provides the best environment for probing reactions involving free radicals. A classical approach to studying reaction dynamics is via bulk kinetic-based measurements of reaction rates influenced by mass- and heat- transfer processes.[26] The shift towards a microscopic view of chemical dynamics for understanding not just bound states of molecular systems but dissociative and metastable states, involved in photoexcitation processes, has led to a growing body of experimental approaches.[27] Some modern experimental techniques include molecular-beam scattering, state-resolved spectroscopy, ultra-fast laser spectroscopy, ion-beam, and ion-imaging techniques for characterizing transient gas-phase species.[2, 28-30]

A general experiment includes 1) the initial state preparation of the reactants, 2) initiating the reaction, and 3) analyzing the products. To prepare reactants for reaction dynamics experiments, the goal is to control the internal quantum states of the system, requiring knowledge of the translational, rotational, vibrational, and hyperfine temperatures. Various techniques can be used to "cool" these internal degrees of freedom. To cool the translational degrees of freedom, one approach is through supersonic expansions where a gas expands from a high-pressure region into a vacuum through a small orifice.[31] Other translational techniques include laser cooling,

evaporative cooling, and deceleration.[32] Additionally, for ions, vibrational and rotational degrees of freedom can be cooled through buffer gas collisions in a radio frequency (RF) trap.[33] The next consideration involves selecting the right species of a specific mass and/or conformation. This can be achieved through mass spectrometry or time of flight mass spectrometry. Following the preparation and selection of the reactants, it is time to initiate the reaction. Some examples include crossed molecular beam methods,[30, 34] collisions in an ion trap, or crossing molecular or ion beams with a probe laser beam. Analyzing the products then involves methods for detecting particles. Ion detection techniques using sensitive microchannel plates (MCPs) and charge pickup techniques for amplifying and quantifying products allow us to probe transient gas-phase reaction dynamics processes. Additionally, for the velocity mapped imaging technique, the products collected yield velocity and angular information of the recoiling fragments which can be extracted post-experiment during data analysis.[35] The advancement of these detection techniques will continue to drive and advance experimental approaches in gas phase reaction dynamics.

1.2. Photoelectron Spectroscopy

Anion photoelectron spectroscopy is a powerful tool to study vibrational and electronic spectroscopy of both negative ions and the resultant neutral formed upon photodetachment.[36, 37] The technique involves crossing a mass-selected anion beam with a fixed-frequency laser (in the visible or near-UV wavelength region) this leads to photodetachment of an electron from the precursor anion which can then be collected and energy analyzed. A general expression for this process can be described as follows:

$$ABC^- + h\nu \rightarrow ABC + e^- \quad (1.1)$$

The photodetached electron contains valuable information relating to the nature of the orbital (or electronic state) from which it was detached and the neutral state(s) accessed thus allowing the investigation of electronic and vibrational properties for the molecule of interest. The kinetic energy of the photodetached electron can be described by the following expression:

$$eKE = E_{h\nu} - AEA - E_{int}(fragment) + E_{int}(anion) \quad (2.2)$$

Where eKE is the electron kinetic energy, $E_{h\nu}$ is the photon energy, AEA is the adiabatic electron affinity, and $E_{int}(fragment)$ and $E_{int}(anion)$ are the internal energy (electronic, vibrational, rotational, etc.) of the neutral and anionic species, respectively. A common way to represent the above expression in photoelectron spectroscopy is by the electron binding energy which is independent of photon energy, eBE = hν – eKE. This approach to studying gas-phase reaction dynamics relies heavily on systems containing stable anions, or a positive electron affinity, and on the production of stable neutral molecules within the BO approximation and molecular orbital (MO) theory.[37] Anion photodetachment also allows for probing the transition state of a neutral reaction by preparing precursor anions resembling the TS regions on the neutral PES. This technique yields valuable information on the electronic symmetry of a photodetachment transition, photoelectron angular distributions (PAD)s, as well as knowledge of the precursor anion and neutral geometries.

The yields of the photoelectrons as a function of eKE forms the photoelectron spectrum, and this intensity distribution provides knowledge of the relative geometries of both the anion and the neutral structures. Because electronic motion is much faster than nuclear motion, photodetachment can usually be described within the Franck-Condon approximation. Following the BO approximation, the wavefunctions for nuclear and electronic components can be

separated.[10] It follows that the intensity yield, I, as a function of eKE corresponds to the overlap of the vibrational wavefunctions of the anion, $\psi_{v'}$, and the neutral, $\psi_{v''}$. The Franck-Condon (FC) factor, $|\langle\psi_{v'}|\psi_{v''}\rangle|^2$, is the probability for vibrational transitions between the anion and neutral states. A schematic illustrating this process can be seen in Figure 1.1.

Photoelectron spectroscopy provides a relatively straightforward approach to access the neutral surface and it has relaxed selection rules since there are no dipole-forbidden transitions, however it generally holds that $\Delta l = \pm 1$. The photodetachment process is then governed by the ability to overcome the electron binding energy (eBE) of the system with a given photon energy, E_{hv}. Since this technique falls under the weak light-matter coupling regime, photodetachment occurs via single-photon processes. It is then important that the initial state of the anion be known as unaccounted internal energy contributions in the anion can lead to misinterpretations in the data due to spectral congestions. Cryogenically cooling precursor anions to ensure that the precursor anion is in its ground vibrational state can help ensure that no observed hotbands are present in the spectra. Given these considerations, the energy resolution of anion photoelectron spectroscopy is quite good with peak widths of ~10 cm^{-1} and 2-3 cm^{-1} for molecular systems using zero electron kinetic energy (ZEKE) spectroscopy and slow photoelectron velocity-map imaging spectroscopy of cryogenically cooled anions (cryo-SEVI), respectively.[38, 39] However, due to the nature of the coincidence experiments, discussed in Section 1.4., due to the uncertainty principle, high resolution photoelectron energies cannot be achieved. Nevertheless, these approaches have advanced photoelectron spectroscopy and our fundamental understanding of gas phase reaction dynamics.[38, 39]

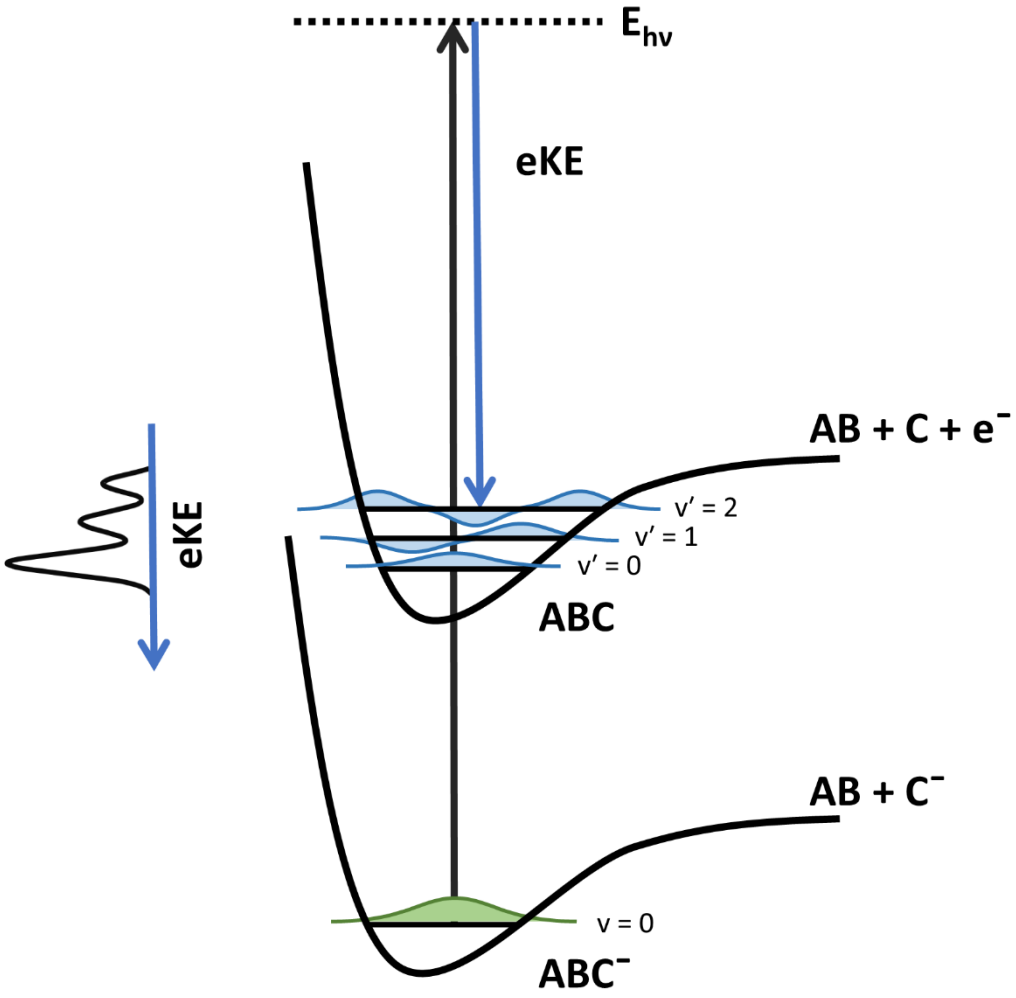

Figure 1.1. Photoelectron spectroscopy schematic. The anion, ABC^-, in its ground vibrational state absorbs a photon and accesses a stable neutral product. The photodetached electron carries away the resultant energy (shown in blue). The intensity of the peaks in the photoelectron spectrum (shown on the left) correspond to the Franck-Condon overlap between the anion and the neutral.

1.3. Photofragment Translational Spectroscopy

The technique of translational spectroscopy cannot be described without considering the role and use of mass spectrometry. Mass spectrometry has been used since the 1920s by Aston to study the dissociation of molecular ions.[40, 41] It was discovered that as the parent molecular ion dissociates, internal energy can be converted into translational energy in the dissociated fragments.[7] Translational spectroscopy thus relies on mass spectrometric tools and the generation of a fast molecular or ionic beam.[6, 42] The useful feature of these beams is that they typically remain in the condition or state in which they were produced during the effective beam lifetime until otherwise perturbed. An example of this process is shown in Figure 1.2.

When dissociation of the molecular or ionic beam is induced either by photons, electrons, or collisions, a detector some distance downstream can be used to measure the position of the fragments separated by a distance, R, along the face of the detector as well as the flight time difference of the fragments. This laboratory frame of reference can then be transformed into the center-of-mass frame of the molecular system providing the kinematics of the dissociation process.[43] In a dissociative photodetachment (DPD) event, the kinetic energy release (KER) of the resultant fragments is given by

$$KER = E_{h\nu} - eKE - \Delta D°(ABC^-) - AEA(C^-) - E_{int} \qquad (3.3)$$

Where $E_{h\nu}$ is the photon energy, $\Delta D°(ABC^-)$ is the bond dissociation energy of the anion, $AEA(\mathrm{C}^-)$ is the adiabatic electron affinity of the specified anion fragment, and E_{int} is the internal energy partitioned into the neutral fragments.

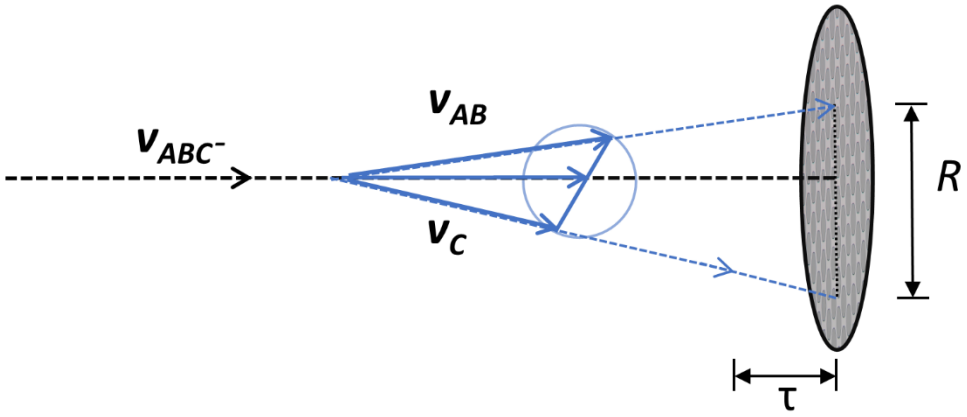

Figure 1.2. Principle of the fast beam translational spectroscopy detection method. A time- and position-sensitive MCP-based detector is used to detect dissociation products AB and C. The flight time difference between the two fragments with velocities v_{AB} and v_C is given by τ. R is the distance between the two fragments that strike the detector. These two quantities, τ and R, help to determine the kinematics of the system in the center-of-mass frame.

The ability to study dissociation processes with this technique provides significant insight into chemical dynamics through conservation of linear momentum and mass conservation. In the dissociation process, the resultant energy can be partitioned into internal degrees of freedom of the recoiling fragments providing insight into the dynamics evolving on the potential energy surface. The measured product energies upon DPD allows for the identification of all accessible pathways and helps to elucidate competing mechanisms.

1.4. Photoelectron-Photofragment Coincidence Spectroscopy

The combination of photoelectron and photofragment techniques leads to a full kinematically-complete picture of a dissociation process. Photoelectron-photofragment coincidence (PPC) spectroscopy, developed in this laboratory, helps characterize transient gas phase species by measuring energy partitioning of reaction pathways (non-dissociative and/or dissociative) induced by the photodetachment of mass-selected precursor anions.[44, 45] This technique is powerful because we can identify the nascent neutral products in coincidence with the corresponding photodetached electron allowing us to gain further insights into the reaction dynamics of a given system. Since the production of a precursor cluster anion frequently resembles the geometry of the transition state on a neutral PES, this technique affords the ability to map onto the neutral potential energy surface while also identifying the neutral products formed. Additionally, these experiments help serve as benchmarks for theoretical calculations.[46]

Since each electron event is measured in coincidence with a resultant photoneutral, $1e^-$ + 1 particle, and/or photofragments, $1e^-$ + 2 momentum-matched particles, these two processes can be distinguished from each other. PPC is a powerful tool which allows a reaction process to be

determined that would otherwise be inferred if only considering photoelectron spectroscopy or translational spectroscopy techniques alone.

In considering the DPD of a system, it is useful to consider a simple schematic of this process as illustrated in Figure 1.3. Upon absorption of a photon, an electron is photodetached from the precursor anion in its ground vibrational state and is mapped onto a neutral potential energy surface. If the portion on the neutral surface is repulsive, the kinetic energy release (KER) of the photofragments can be determined. If the photofragments contain excitation along a given vibrational mode it can also be identified. There are indirect DPD processes that have been described previously,[47-49] however, it will not be discussed at length. The studies reported here focus on direct dissociative photodetachment processes of weakly bound clusters yielding slowly recoiling photofragments. However, the involvement of metastable states in the dissociation dynamics for the systems studied in this program, discussed in later chapters, do play a significant role. In particular, Feshbach resonances, which are metastable states that have enough energy to dissociate but do not because the energy is stored in internal degrees of freedom, are found to mediate the reaction dynamics involved near the transition state portion of the neutral reaction accessed upon photodetachment.

The kinetic energies of all the products in a dissociation event can be plotted in a coincidence plot called a photoelectron-photofragment coincidence spectrum where the eKE is plotted versus the KER of the resultant neutral products. Figure 1.4 shows how this plot appears given the corresponding schematic for a DPD process. The diagonal features correspond to kinetic energy maxima (KE_{max}) thresholds defined by the following expression:

$$KE_{max} = E_{h\nu} - \Delta D°(ABC)^{-} - AEA(C^{-}) - E_{int}(frag) + E_{int}(anion) \qquad (4.4)$$

In most of the studies carried out in the research reported here, $E_{int}(anion)$ is assumed to be zero as the precursor anions are formed in their ground vibrational states. However, accurate KE_{max} thresholds can be set if a vibrational mode of the precursor anion is excited in a controlled manner. The next chapter will expand on these sections and describe the basis of the experimental apparatus used here to study gas-phase reaction dynamics of transient species.

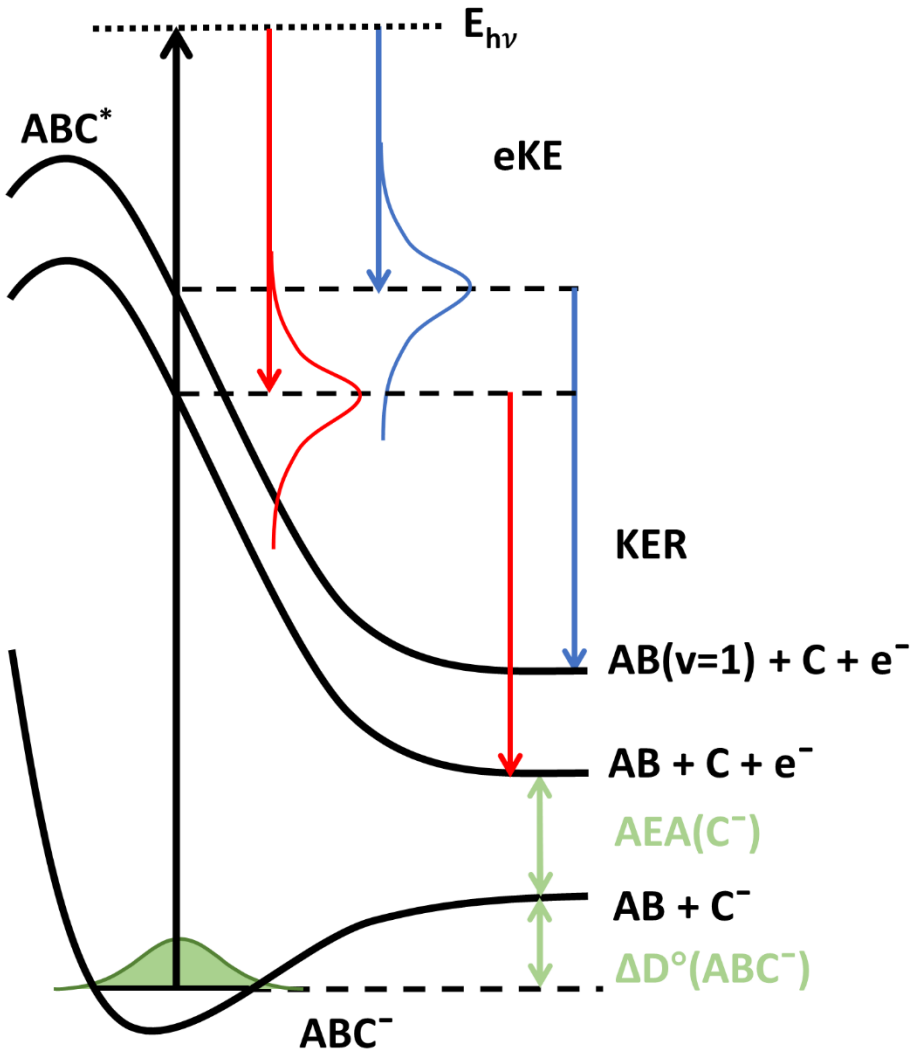

Figure 1.3. Dissociative photodetachment schematic. An anion, ABC-, absorbs a photon, $E_{h\nu}$, and accesses two dissociative states AB + C + e- and AB(v=1) + C + e- where the latter has 1 quanta of excitation in a vibrational mode of AB. Both electrons and resultant neutral fragments are collected in coincidence on an event-by-event basis.

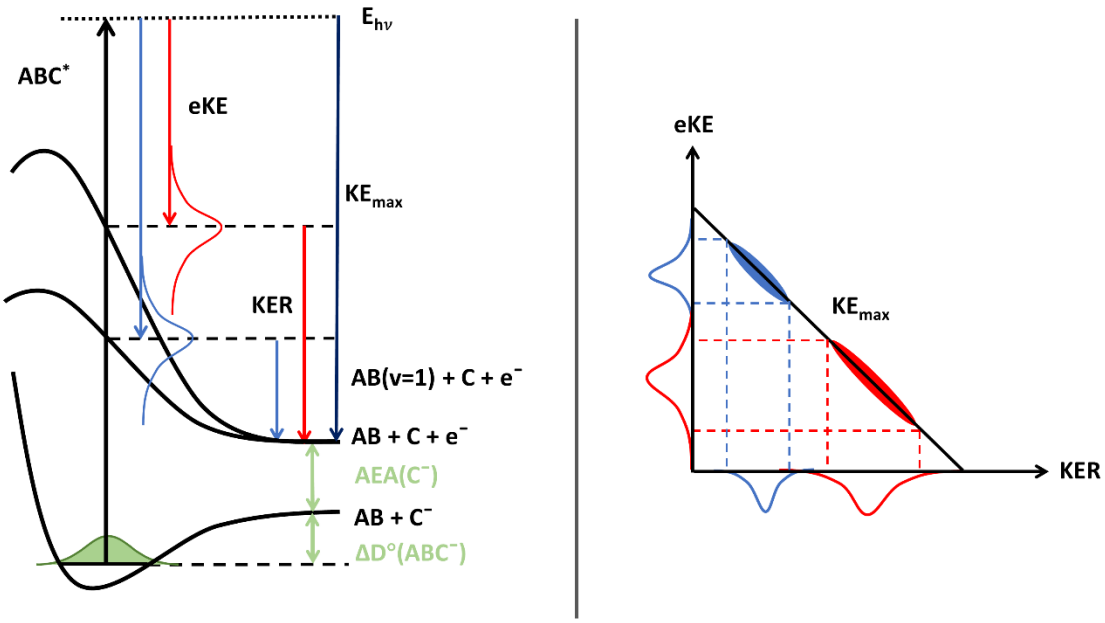

Figure 1.4. Direct dissociative photodetachment schematic and its corresponding photoelectron-photofragment coincidence (PPC) plot. In this example, an anion absorbs a photon, E_{hv}, and accesses the same channel via two different potential energy surfaces. These can be distinguished from each other in the PPC plot shown on the right. The KE_{max} threshold is the total resultant energy, eKE + KER.

1.5. References

1. Levine, R. D.; Bernstein, R. B., *Molecular Reaction Dynamics and Chemical Reactivity*. Oxford University Press: New York, 1987

2. Casavecchia, P., Chemical reaction dynamics with molecular beams. *Reports on Progress in Physics* **2000,** *63* (3), 355-414.

3. Hartmann, J.-M.; Boulet, C.; Robert, D., I - Introduction. In *Collisional Effects on Molecular Spectra*, Hartmann, J.-M.; Boulet, C. Robert, D., Eds. Elsevier: Amsterdam, 2008; pp 1-7.

4. Herschbach, D. R., Molecular Dynamics of Elementary Chemical Reactions (Nobel Lecture). *Angewandte Chemie International Edition in English* **1987,** *26* (12), 1221-1243.

5. Pauly, H., *Atom, Molecule, and Cluster I: Basic Theory, Production and Detection of Thermal Energy Beams*. Springer-Verlag Berlin Heidelberg: 2000; p XVI, 344.

6. Carrington, A., Review Lecture. Spectroscopy of molecular ion beams. *Proceedings of the Royal Society of London. A. Mathematical and Physical Sciences* **1979,** *367* (1731), 433-449.

7. Los, J.; Govers, T. R., Collision-Induced Dissociation of Diatomic Ions. In *Collision Spectroscopy*, Cooks, R. G., Ed. Springer US: Boston, MA, 1978; pp 289-356.

8. Pohl, R.; Antognini, A.; Nez, F.; Amaro, F. D.; Biraben, F.; Cardoso, J. M. R.; Covita, D. S.; Dax, A.; Dhawan, S.; Fernandes, L. M. P.; Giesen, A.; Graf, T.; Hänsch, T. W.; Indelicato, P.; Julien, L.; Kao, C.-Y.; Knowles, P.; Le Bigot, E.-O.; Liu, Y.-W.; Lopes, J. A. M.; Ludhova, L.; Monteiro, C. M. B.; Mulhauser, F.; Nebel, T.; Rabinowitz, P.; dos Santos, J. M. F.; Schaller, L. A.; Schuhmann, K.; Schwob, C.; Taqqu, D.; Veloso, J. F. C. A.; Kottmann, F., The size of the proton. *Nature* **2010,** *466* (7303), 213-216.

9. Continetti, R. E.; Guo, H., Dynamics of transient species via anion photodetachment. *Chem. Soc. Rev.* **2017,** *46* (24), 7650-7667.

10. Born, M.; Oppenheimer, J. R., On the Quantum Theory of Molecules. *Ann. Physik* **1927,** *84*, 457-484.

11. London, F., *Z. Elektrochem.* **1929,** *35*, 552.

12. *Advances in Chemical Physics*. John Wiley & Sons, Inc.: 1988; Vol. 154.

13. Fu, B.; Shan, X.; Zhang, D. H.; Clary, D. C., Recent advances in quantum scattering calculations on polyatomic bimolecular reactions. *Chemical Society Reviews* **2017,** *46* (24), 7625-7649.

14. Guo, H., Quantum dynamics of complex-forming bimolecular reactions. *International Reviews in Physical Chemistry* **2012,** *31* (1), 1-68.

15. Otto, R.; Ma, J.; Ray, A. W.; Daluz, J. S.; Li, J.; Guo, H.; Continetti, R. E., Imaging Dynamics on the $F + H_2O \rightarrow HF + OH$ Potential Energy Surfaces from Wells to Barriers. *Science* **2014,** *343* (6169), 396.

16. Zhang, D. H.; Guo, H., Recent Advances in Quantum Dynamics of Bimolecular Reactions. *Annual Review of Physical Chemistry* **2016,** *67* (1), 135-158.

17. Li, J.; Zhao, B.; Xie, D.; Guo, H., Advances and New Challenges to Bimolecular Reaction Dynamics Theory. *The Journal of Physical Chemistry Letters* **2020,** *11* (20), 8844-8860.

18. Warneck, P., Tropospheric Chemistry. In *Encyclopedia of Physical Science and Technology (Third Edition)*, Meyers, R. A., Ed. Academic Press: New York, 2003; pp 153-174.

19. Clemitshaw, K. C., Tropospheric Chemistry and Composition | Hydroxyl Radical. In *Encyclopedia of Atmospheric Sciences (Second Edition)*, North, G. R.; Pyle, J.; Zhang, F., Eds. Academic Press: Oxford, 2015; pp 232-238.

20. Glassman, I.; Yetter, R. A.; Glumac, N. G., *Combustion*. Elsevier Science: 2014.

21. Monks, P. S., Gas-phase radical chemistry in the troposphere. *Chem. Soc. Rev.* **2005,** *34* (5), 376-395.

22. Acharyya, K.; Herbst, E.; Caravan, R. L.; Shannon, R. J.; Blitz, M. A.; Heard, D. E., The importance of OH radical–neutral low temperature tunnelling reactions in interstellar clouds using a new model. *Molecular Physics* **2015,** *113* (15-16), 2243-2254.

23. Canosa, A., Gas phase reaction kinetics of complex organic molecules at temperatures of the interstellar medium: The $OH + CH_3OH$ case. *Proceedings of the International Astronomical Union* **2019,** *15* (S350), 35-40.

24. Isaksen, I. S. A.; Dalsøren, S. B., Getting a Better Estimate of an Atmospheric Radical. *Science* **2011,** *331* (6013), 38.

25. Herzberg, G., *The Spectra and Structure of Simple Free Radicals: An Introduction to Molecular Spectroscopy*. Cornell University Press: Ithaca, New York, 1971.

26. Levich, V. G., Theory of Macroscopic Kinetics of Heterogeneous and Homogeneous-Heterogeneous Processes. *Annu. Rev. Phys. Chem* **1967,** *18*, 153–176.

27. Steinfeld, J. I.; Francisco, J. S.; Hase, W. L., *Chemical Kinetics and Dynamics*. Prentice Hall: 1999.

28. Zare, R. N., Laser Control of Chemical Reactions. *Science* **1998,** *279* (5358), 1875.

29. Yang, X., State-to-State Dynamics of Elementary Bimolecular Reactions. *Annual Review of Physical Chemistry* **2007,** *58* (1), 433-459.

30. Pan, H.; Liu, K.; Caracciolo, A.; Casavecchia, P., Crossed beam polyatomic reaction dynamics: recent advances and new insights. *Chem. Soc. Rev.* **2017,** *46* (24), 7517-7547.

31. van de Meerakker, S. Y. T.; Bethlem, H. L.; Meijer, G., Taming molecular beams. *Nature Physics* **2008,** *4* (8), 595-602.

32. Metcalf, H. J.; van der Straten, P., Laser cooling and trapping of atoms. *Journal of the Optical Society of America B* **2003,** *20* (5), 887-908.

33. Wester, R., Radiofrequency multipole traps: tools for spectroscopy and dynamics of cold molecular ions. *Journal of Physics B: Atomic, Molecular and Optical Physics* **2009,** *42* (15), 154001.

34. Herschbach, D. R., Reactive Collisions in Crossed Molecular Beams. **1962**.

35. Thompson, J. M. T.; Vallance, C., 'Molecular photography': velocity–map imaging of chemical events. *Philosophical Transactions of the Royal Society of London. Series A: Mathematical, Physical and Engineering Sciences* **2004,** *362* (1825), 2591-2609.

36. Neumark, D. M., Probing chemical dynamics with negative ions. *The Journal of Chemical Physics* **2006,** *125* (13), 132303.

37. Sanov, A.; Mabbs, R., Photoelectron imaging of negative ions. *International Reviews in Physical Chemistry* **2008,** *27* (1), 53-85.

38. Kitsopoulos, T. N.; Waller, I. M.; Loeser, J. G.; Neumark, D. M., High resolution threshold photodetachment spectroscopy of negative ions. *Chemical Physics Letters* **1989,** *159* (4), 300-306.

39. Weichman, M. L.; Neumark, D. M., Slow Photoelectron Velocity-Map Imaging of Cryogenically Cooled Anions. *Annual Review of Physical Chemistry* **2018,** *69* (1), 101-124.

40. Aston, F. W., LIX. The mass-spectra of chemical elements. *The London, Edinburgh, and Dublin Philosophical Magazine and Journal of Science* **1920,** *39* (233), 611-625.

41. McGowan, W.; Kerwin, L., On The Application of Aston Bands and Appearance Potential Measurements to Ion Collision Studies. *Canadian Journal of Physics* **1963,** *41* (2), 316-342.
42. Gardner, L. D.; Graff, M. M.; Kohl, J. L., Fast beams apparatus for the study of photodissociation processes. *Review of Scientific Instruments* **1986,** *57* (2), 177-184.

43. de Bruijn, D. P.; Los, J., Time and position-sensitive detector for dissociative processes in fast beams. *Review of Scientific Instruments* **1982,** *53* (7), 1020-1026.

44. Continetti, R. E., Photoelectron-photofragment coincidence studies of dissociation dynamics. *International Reviews in Physical Chemistry* **1998,** *17* (2), 227-260.

45. Continetti, R. E., COINCIDENCE SPECTROSCOPY. *Annu. Rev. Phys. Chem.* **2001,** *52* (1), 165-192.

46. Continetti, R. E.; Guo, H., Dynamics of transient species via anion photodetachment. *Chemical Society Reviews* **2017,** *46* (24), 7650-7667.

47. Ray, A. W. Dissociation Dynamics of Transient Molecules Studied by Photoelectron-Photofragment Coincidence Spectroscopy. University of California, San Diego, San Diego, 2016.

48. Shen, B. B. Preparation of Hot and Cold Ions for Photoelectron-Photofragment Coincidence Spectroscopy. University of California, San Diego, San Diego, 2018.

49. Lunny, K. G. Investigation of Reactive Oxides and Radical Dynamics by Photoelectron-Photofragment Coincidence Spectroscopy. University of California, San Diego, San Diego, 2019.

Chapter 2: Experimental Methods and Data Analysis

This chapter focuses on the experimental apparatus used for studying gas-phase reaction dynamics of transient species.

2.1. Photoelectron-Photofragment Coincidence Spectrometer

The experimental apparatus described here is the photoelectron-photofragment coincidence spectrometer, also known as Machine C.[1-3] As mentioned in the previous chapter, PPC spectroscopy couples photoelectron and translational spectroscopy techniques. A fast anion beam is generated and different mass-to-charge, m/z, anion species in the beam can be separated by time of flight (TOF). First, the anions of interest are generated and prepared in their ground vibrational state. Following this, the anions can be accelerated resulting in a fast ion beam that can then be focused and steered into an ion storage to be interrogated by a laser. The resultant products are then collected and analyzed. The following sections will discuss in more detail these aspects of the experiment. A schematic of this experimental setup can be seen in Figure 2.1. comprising of the various differentially pumped chambers.

2.1.1. Anion Source

The main goal in generating precursor anions for this program was to prepare anions in their ground vibrational state in large enough quantities for study. It is critical to know what the starting conditions are for the parent anion as it improves the ability to assign spectra, vary the internal energy in the anions in a known and controlled manner, and allow the study of more complex systems.[4] Initially, a translationally cold molecular beam is generated via supersonic expansion.[5] The molecular beam is formed by passing a gas from a high-pressure region (usually 30-50 psig) into vacuum (~10^6 Torr) via a piezoelectric pulsed valve with a small orifice such that

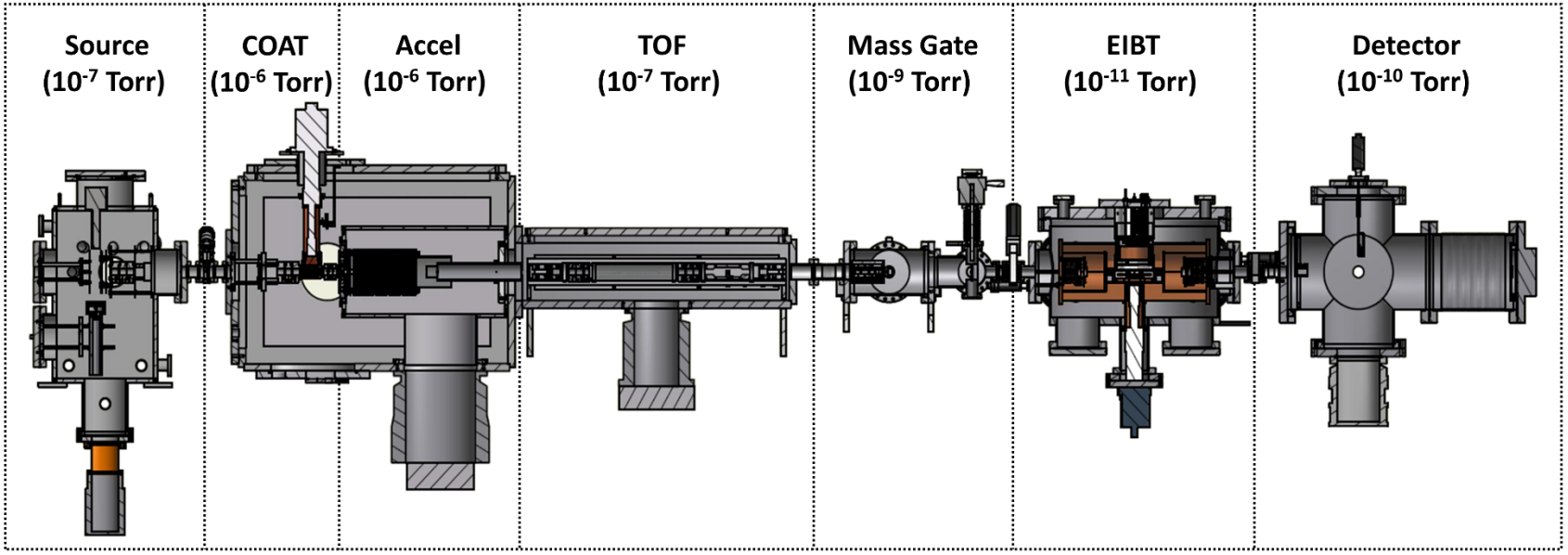

Figure 2.1. Schematic of the Photoelectron-Photofragment Coincidence Spectrometer.

the mean free path of the gas is much smaller than the orifice diameter. The molecules exiting the valve collide with each other in the high-density region of the expansion causing adiabatic cooling of all degrees of freedom and yielding a supersonic expansion. The energy lost through collisions is converted into kinetic energy leading to a directed beam with typical densities of 10^{13} molecules cm^{-3} with translational temperatures of several Kelvin (rotational temperatures are on the same order).[5]

The pulsed valve is pulsed at 10 Hz with 150-250 μs pulse width during which the beam passes through a pulsed coaxial discharge held at 500-600 V causing the species in the beam to ionize via collisions. This process can reintroduce unwanted internal energy in the resultant ion beam and, as a result, a number of improvements have been made to the experimental setup to help in cooling the total degrees of freedom of the precursor anions (discussed in the next section). An electron beam that counter-propagates the ion beam is also used to help stabilize operation of the discharge. The ions are then extracted along the beam axis using a Wiley-McLaren mass spectrometer[6] that focuses the packet of ions in space and time into a cryogenic octopole accumulation trap (COAT).

2.1.2. Cryogenic Octopole Accumulation Trap

The implementation of COAT has led to many advantages in the generation of cold anions for PPC study.[3, 7] A detailed description of this setup has been previously described and will be briefly described here.[8] COAT is a radio frequency (RF) octopole ion trap based on a similar design by Wester and coworkers.[9, 10] It uses buffer gas cooling at cryogenic temperatures to cool the external and internal degrees of freedom of precursor anions down to several K. It has 8 rods arranged in a circular pattern and each rod has an RF voltage that is 180 degrees out-of-phase from each adjacent rod. This oscillating RF field confines the trapped ions in the radial direction. The

rods are surrounded by three shaping electrodes which allows for the anions to be trapped closer towards the exit side of the trap. The anions are confined axially via endcaps by switching the entrance endcap from ground to a repulsive potential upon anion entry into COAT. The exit endcap remains at a repulsive potential and is switched after 40 ms, allowing the trapped anions to be extracted. While the anions are trapped in COAT, their internal degrees of freedom are cooled through collisions with a < 10 K thermalized buffer gas. The buffer gas used is typically He or 20% H_2 in He with the latter being the optimal gas for producing colder anions.[3]

COAT is mounted on the 2nd stage of a Sumitomo RDK-205D 4K Cryocooler cold head. The trap also has radiative shielding to protect against black body radiation, cooled by the 1st stage of the cold head. The buffer gas is introduced via a pulsed Gerlich-type valve through a copper tube allowing for precooling of the buffer gas prior to injection into COAT. The background pressure in the COAT chamber is ~2.6×10^{-6} Torr without buffer gas and increases to 3-5×10^{-6} Torr with buffer gas (exact pressure varies depending on the precursor anion of interest). The Gerlich valve is calibrated using an ethanol bath and backing the valve with ~30 psig of an inert gas such that a slow stream of bubbles are generated at a driving voltage of 20-30 V.

COAT can also be operated at room temperature (RT) or not used depending on the experiment performed. When COAT is not used, the anions pass through and are instead focused and steered towards the acceleration stage. Operating COAT at RT allows for usage of other buffer gases that would otherwise condense onto the trap at lower temperatures and provides a controlled way to produce thermalized anions at 300K. It also provides another means of producing precursor anions of interest in the future by association reactions in the trap. Temperature control of the rf trap will also prove to be a powerful tool for generating precursor anions of interest expanding the range of molecules and clusters that can be studied with PPC spectroscopy. Additionally, IR

excitation of cold anions produced in COAT will allow for enhanced control of the initial products for studying how excitation of certain vibrational modes enhances reactivity or affects branching ratios, as described in a previous thesis from this group.[11]

2.1.3. Acceleration/Time-of-Flight/Mass Gate

After the ions are trapped and cooled in COAT for 40 ms, they are extracted and accelerated by a stack of 31 electrodes comprised of a voltage divider set by a resistive network allowing for a constant voltage ramp from ground to full potential (~7 kV). 11 of these plates contained within the stack are modified such that the apertures are larger and they can be independently controlled as an einzel lens configuration to help focus the ion beam as it is accelerating up to full potential. After the ions pass through the acceleration plates, they enter a 30 cm cylindrical metal tube with a 3 mm and 5 mm entrance and exit aperture, respectively. This tube is held to the same potential as the previous electrode and is switched to ground with a high-voltage (HV) switch (Behlke HTS 101-01). Re-referencing the ions to ground is critical for safe operation of the experiment as it removes the need to float electrodes at high voltage downstream. Upon exiting the HV switch tube, the ion packet is collimated with a temporal length of ~2-4 μs. Different ion species in the ion packet all have the same kinetic energy and can be separated from each other in time based on their m/z and the path length traveled. The resultant ion packet is governed by the length of the HV switch tube which sets, in part, the resolution of the TOF mass spectrometer.

The TOF chamber is comprised of 2 sets of einzel lenses and 2 sets of vertical and horizontal deflectors for focusing and steering a collimated ion beam through the mass gate (MG) chamber. A "Bakker-style" chopper[12] at the entrance of the MG chamber can be used to select a narrow cross section of the ion packet to remove anions of neighboring m/z from the ion packet. This chopper contains two parallel plates, one is switched to potential while the other is held at

half that potential. The voltage is switched when the ions are centered between the two electrodes. This chopper is not used during experiments and typically only serves to help identify species in the ion packets through a TOF mass spectrum. Following this chopper is a high voltage einzel lens and a set of vertical and horizontal deflectors to focus and steer the ion beam into the next chamber. An ion detector can be translated in and out of the ion beam used to help optimize ion intensity.

2.1.4. Electrostatic Ion Beam Trap

The mass-selected precursor anions are loaded into the electrostatic ion beam trap (EIBT) which stores fast (keV) ion beams (based on an ion storage trap by Zajfman and co-workers).[13] The ions can be stored from hundreds of ms up to several seconds. Collimated ion beams of a given energy are reflected in a stable oscillating trajectory (dependent on its beam energy and m/z) between two electrostatic mirrors and is equivalent to a one-dimensional storage ring. The implementation of the EIBT[2, 14] has proven to generate better resolved data at higher acquisition rates. This was achieved by coupling the low-repetition rate source of 10-20 Hz to the kHz data acquisition rates required for these PPC experiments.

The EIBT consists of an entrance and exit stack of mirrors, bunching electrode, and a pick-up electrode. The entrance mirror is comprised of a set of electrodes with a potential ramp from -11 kVs to ground via an external voltage divider network followed by a focusing lens to help keep the ion beam collimated. The exit mirror and lens are held at potential throughout the duration of the data collection. The entrance mirror and lens are switched to potential by Behlke HTS 201-03-GSM and HTS 151-03-GSM switches, respectively. Once the precursor anions enter the trap and pass through the entrance mirror stack, they induce a charge on a pickup electrode instrumented with a charge-sensitive preamplifier (Amptek CoolFET A250CF) which helps to determine the switching time for the entrance mirror stack. The EIBT is mounted on a closed-cycle He

refrigerator (Austin Scientific, CryoPlex 1020) cooled to ~20 K and enclosed in radiation shields to help reduce black body radiation.

Over the course of the ion storage period, synchronization with the pulsed laser can help to ensure high ion density and temporal overlap between the oscillation ion packet and the laser. This is achieved by applying a small RF field (~1 V amplitude) along the beam axis which matches the fundamental or 2^{nd} harmonic oscillation frequency of the oscillating precursor anions of interest. This helps to limit the spatial spread of the ion beam in the EIBT while also helping to facilitate fast data collection by selecting for optimal crossing of anions with the pulsed laser in the direction of the neutral particle detector.

Usage of the bunching electrode is not necessarily required for PPC experiments and instead the apparatus can be operate under a multi-mass mode (described in more detail elsewhere).[2, 15] Rather than select one species of a given m/z, a packet of ions in a given m/z range can be trapped and crossed at each data acquisition cycle leading to multiple sets of PPC data collected simultaneously for multiple species during an experimental cycle. In multi-mass mode, it is possible to detect ~6 different m/z species in a 900 ns neutral particle time-of-arrival (TOA) window. These data can then be differentiated during data analysis by selecting specific neutral species by the TOA and examining the photoelectrons in coincidence.

The interaction region of the ions and the laser is centered in the field free region of the EIBT. The electron detector is mounted perpendicularly over this field free region where photodetached electrons can be extracted orthogonal to the ion beam. Upon photodetachment, the resultant neutral fragment(s) are no longer influenced by the surrounding electric fields and can proceed through the EIBT chamber into the next and final chamber.

2.1.5. Detector Chamber

The detector chamber consists of a multi-particle neutral detector (discussed in section 2.4.2.) and an ion detector. The neutral particle detector is mounted in line with the beam path on a vertical translator which can be optimized to the neutral beam path. The ion detector consists of a chevron stack of two 1" diameter MCPs with a stainless-steel anode and a fast preamplifier (Ortec VT120). This detector is mounted above the beamline and an ion deflector deflects the ions entering the chamber towards it for TOF measurements allowing for mass determination. Once the precursor anion has been mass-selected, the ion intensity can be optimized by scanning source timings and electrode potentials in the source, COAT, Accel, TOF, and MG chambers.

2.2. Vacuum System

As discussed in the previous chapter, the first molecular beam experiments carried out in the early 1900s were a consequence of the invention of the vacuum pump. Many improvements have been made since which makes it possible for the experiments discussed here to be performed. The fast ion beam, critical for these experiments, is collimated with minimal translational energy spread, and so long as there is sufficient pumping power in the chambers, the ion beam will remain in the same condition thus increasing its effective lifetime until otherwise perturbed. These perturbations can arise from collisions with a background gas so mean free path considerations need to be accounted for when designing these experiments (maximum distance a molecule can travel before colliding with another molecule).

Although maintaining high vacuum is critical for most of the PPC spectrometer, the source regions rely on relatively higher pressures to prepare the necessary precursor anions for study. The ion discharge source in the source chamber relies on collisions of the species in the supersonic

expansion for generating anions and the turbomolecular pumps (TMPs) that are used need to have a suitable pumping speed to expel the gas coming through the pulsed valve nozzle. This is important because if the gases are not being pumped out fast enough at the 10 Hz repetition rate of the nozzle, the higher pressure in the chamber can lead to a decreased mean free path of the anion beam leading to unwanted collisions with the background gas and affecting the production of the desired precursor anion. This point will be addressed in the appendix in the discussion of the dual pulsed valve anion source. Additionally, the high-pressure conditions in the COAT chamber are necessary since the preparation of internally cold anions is achieved through a controlled environment of buffer gas collisions in the rf trap at cryo- or room temperatures.

One of the most sensitive chambers that requires ultrahigh vacuum and where the bulk of the anion trajectory occurs is the EIBT chamber. The anions travel approximately 1-meter round trip with typical anion oscillation frequencies on the order of hundreds of kHz, therefore sufficiently large mean free paths (10^5-10^6 m) are required if the anions are to be stored for several seconds. The ability to differentially pump each chamber towards progressively lower pressures from the source chamber to the EIBT and detector chambers helps in achieving the necessary conditions for optimal operation of the PPC spectrometer. It also provides a practical route for performing maintenance on any one chamber without needing to compromise the vacuum in a neighboring chamber.

The source chamber is pumped by an Edwards nEXT 240D TMP with a pumping speed of 240 l/s and it is backed by an Edwards XDS35i scroll pump (35 m^3/h). Background and operational pressures in this chamber are ~10^{-7} and ~10^{-5}-10^{-4} Torr, respectively. A TMP with a higher pumping speed might be favorable for this chamber when using a dual pulsed valve setup (discussed in Appendix A), however, when using one pulsed valve for generating ions, this pump

is adequate. This chamber is isolated from the COAT chamber via a pneumatic beamline gate valve, allowing for frequent necessary maintenance.

The COAT, acceleration, and TOF chambers are each pumped separately however they connect through small orifices and are backed by the same Edwards XDS35i scroll pump. As such, pressure increases in the COAT chamber caused by buffer gas cooling ($3x10^{-6}$ Torr operating pressure) do not influence the pressures in the acceleration and TOF chambers (10^{-8}-10^{-7} Torr). COAT, acceleration, and TOF chambers are evacuated by magnetically levitated TMPs with pumping speeds of 3200 L/s (Edwards STP XA3203C), 2200 L/s (Edwards STP-A2503PV), and 800 L/s (Edwards STP-A803WAV-U), respectively. It should be noted that most of the experiments discussed in the following chapters were collected with these TMPs, however, they were replaced with new TMPs (discussed in Appendix B).

Following the COAT/Accel/TOF chambers, all chambers are separated by pneumatic beamline gate valves. The smallest chamber, the MG chamber (10^{-9} Torr), is pumped by two TMPs, Pfeiffer TMU 260 (210 L/s pumping speed) and an Edwards EXT 250H (250 L/s pumping speed) to help reduce the gas load before the EIBT chamber (10^{-11} Torr). The EIBT chamber is pumped by a 2500 L/s cryopump (Oxford Instruments, Cryo-Plex 8) and a home-built 3000 L/s titanium sublimation pump (the latter is only used to degas the chamber). The detector chamber is pumped by a magnetically levitated 400 L/s Edwards EXT255H TMP which is backed by a 250 L/s Osaka TG420MCAB TMP. Both the MG and detector chambers are backed by the same Edwards nXDS 10i scroll pump. The EIBT chamber is isolated from this scroll pump through a manual valve and is only used to rough out the EIBT chamber when pumping down. A vacuum diagram of this instrument can be seen in Figure 2.2.

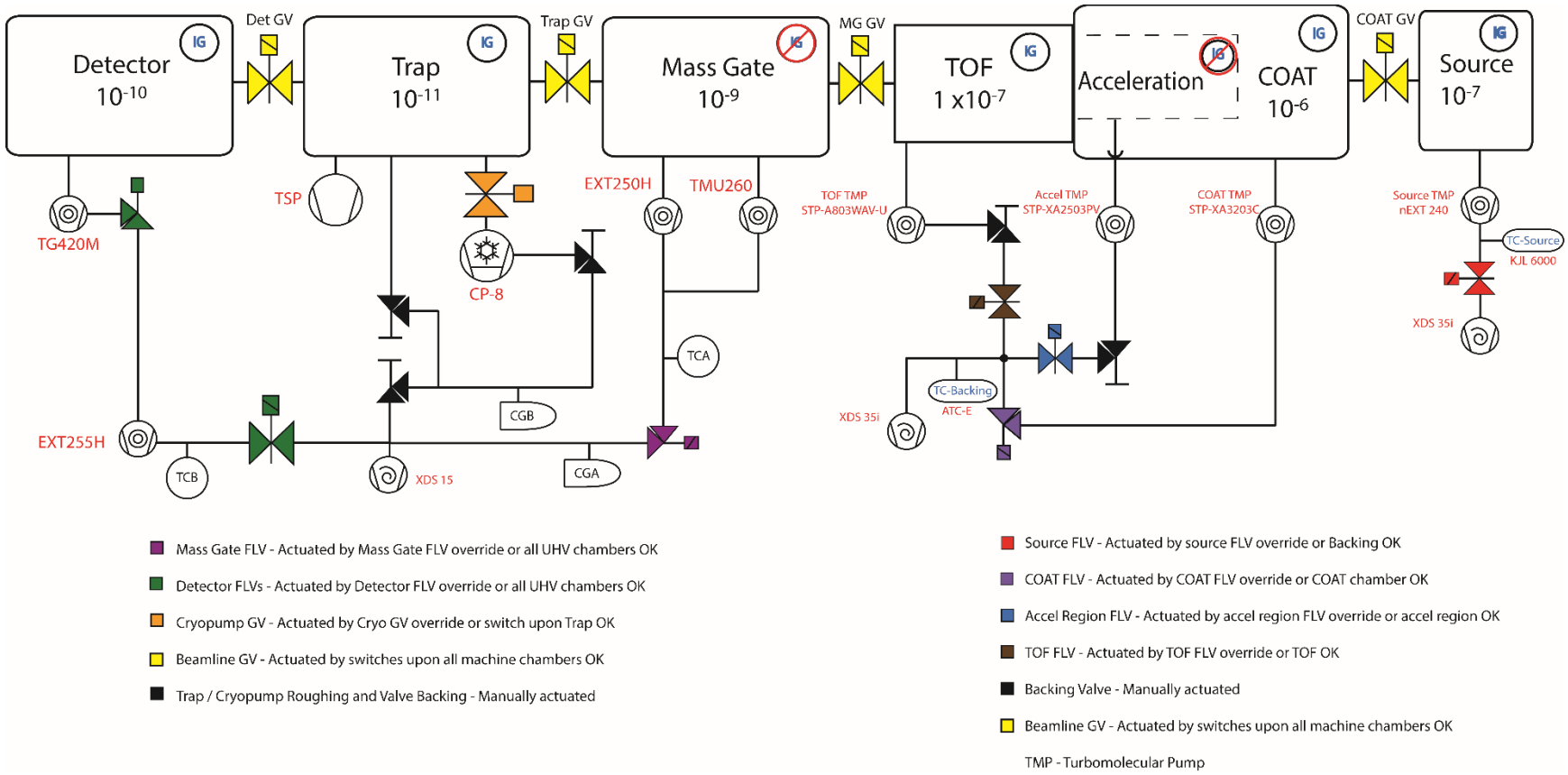

Figure 2.2. PPC spectrometer vacuum system logic.

2.3. Laser System

PPC spectroscopy requires a high duty cycle data acquisition due to the low coincidence measurement rates that are necessary to avoid false coincidence events.[16] High temporal resolution is also necessary for proper recording of electron events in PPC measurements. Given these considerations, a short-pulse pico- or femto-second laser with a high oscillation frequency is used for these PPC experiments.

The laser system used for most of these experiments was a solid-state titanium sapphire picosecond regenerative amplifier (Clark MXR CPA-2000) with a fundamental output of 775 nm light, 1.2 ps pulse width, and 400 μJ/pulse at a repetition rate of 1037 Hz. The laser system has a two-layer vertical structure where the bottom level is the laser pulse stretcher and the top layer is the laser pulse compressor. This apparatus uses a chirped-pulse amplification technique to create ps laser pulses > 100 μJ/pulse. This is achieved by using dispersive gratings to first stretch, or lengthen, short laser pulses before amplification and then compress the laser pulses to return the pulse to its original pulse width after amplification.[17] This technique helps to ensure the power inside the amplifier cavity remains low enough to avoid damaging the laser optics which can have negative effects on the performance of the laser.

The picosecond regenerative amplifier used to amplify the Ti:Sapphire output contains a series of lasers and optical systems. A mode locked[18] diode-pumped fiber laser produce picosecond seed pulses at 43.58 MHz repetition rate. These seed pulses are then temporally stretched and injected at 1037 Hz into the Ti:Sapphire regenerative amplifier cavity. The Ti:Sapphire rod is pumped by a high-power (5-8 Watts) Q-switched Nd:YAG laser (532 nm output) and the seed pulse passes through the rod multiple times. When the maximum energy in the cavity is reached, the pulse is ejected using a Pockels cell (fast-polarization rotator) and the dump propagates towards

the compressor where the resultant output is a short ps 775 nm (1.60 eV) laser pulse at 1037 Hz. This fundamental output can be frequency doubled (388 nm, 3.20 eV) or tripled (258 nm, 4.80 eV) using a beta-Barium-Borate (BBO) crystal or used directly for PPC measurements. The desired laser beam is redirected towards the EIBT chamber and aligned so that it passes through the interaction region. A 40-50 cm focal length lens or a 2.5:1 telescope can be used to focus or collimate the beam, respectively, down to ~1 mm diameter beam spot size. At higher photon powers, collimating the laser and installing baffles on the entrance and exit sides of the vacuum chamber are necessary to limit the high background noise.

The Clark MXR CPA-2000 system described above was eventually updated to a new model, Clark MXR CPA-2010, but the operating principle remains the same. The older CPA-2000 system was converted into a femtosecond system with 200-300 fs pulse width by swapping out the stretcher grating to a femtosecond grating and removing the birefringent filters (BRFs) in the regen cavity that is only necessary for shaping picosecond pulses.

2.4. Detectors

The two detectors used for PPC measurements collect time and position information over the full 4π solid angle distribution of the photodetached electrons or the recoiling photofragment(s). Both the photoelectron detector and the neutral particle detector (described in more detail in the following sections) use a z-stack of MCPs which amplifies each detected event via a cascade of electrons yielding an electron cloud of ~10^7 electrons.[19] This electron cloud then impinges on an anode which records the position of the event. The electron detector uses velocity map imaging (VMI) with a wedge-and-strip anode[20, 21] to determine the kinetic energies of the photodetached electrons. The neutral particle detector uses a four-quadrant crossed delay-line anode[22] to determine the kinetic energy release in the center-of-mass frame of the recoiling

photofragments. The time and position for all electrons and neutrals produced upon interrogation with a laser are recorded on an event-by-event basis.

2.4.1. Photoelectron Detector

Photoelectrons are extracted orthogonal to the laser and ion beam in the interaction region. As the anions oscillate in the EIBT, they enter a field-free region. When the electrons are photodetached, the electrons are mapped onto the electron detector through a set of electrostatic lenses consisting of a repeller (-30 V), extractor (0V), and a focusing lens (160-170 V). To counteract the influence that the repeller has on the ion trajectory in the trap, a corrector electrode of opposite polarity is used to maintain a stable trajectory over the course of the EIBT trapping period. The extracted electrons pass through a copper cylinder that provides a field-free region prior to striking the z-stack of MCPs. The electrons are accelerated to -400 V dictated by the front plate and the potential on the back plate (~4800 V). This enclosure helps to eliminate field distortions from the surrounding fields in the interaction region. The photoelectron detector is also housed in a magnetic shield (mu metal) to shield the electron trajectories from static or low-frequency magnetic fields.

The timing resolution, z axis, is limited due to the influence the focusing elements has on the electron trajectories as well as the short TOF. The spatial resolution, important for VMI, depends on sharply focusing the electrons on the face of the MCPs as well as having a long enough flight path for electrons of different velocities to be resolved.[23] Considerations to improve the current electron detector resolution should involve an increase to the electron TOF.

The wedge and strip anode is used for detecting position information of the photodetached electrons. This anode has been described previously[20, 24] so will only be described briefly here.

The anode contains 3 conductors known as a wedge, strip, and zig-zag. An electron cloud from the MCPs impinges on the anode where the positions could then be determined by charge division. The areas of each conductor vary making it possible to determine where the center of the electron cloud is detected. The wedge tapers along the x direction and the strip increases in width along the y direction. The zig-zag conductor fills the space between the wedge and strip conductors and serves for charge normalization. A drawing of this can be seen in Figure 2.3. The following equations are used to calculate the x and y positions through charge division between the different shaped electrodes.

$$x \propto \frac{Q_w}{Q_w + Q_s + Q_z} \tag{2.1}$$

$$y \propto \frac{Q_s}{Q_w + Q_s + Q_z} \tag{2.2}$$

2.4.2. Multi-particle Time and Position Sensitive Neutral Detector

While the electron detector described above is suitable for detecting one electron event, it cannot yield position information for > 1 particle events. As a result, a multiparticle neutral detector known as the quadrant crossed delay line (QXDL) is used to detect two momentum-matched particles in coincidence with a photodetached electron. This detector has been described previously.[22, 25] Briefly, photofragments that strike a z-stack configuration of MCPs causes a cascade of electrons and the resultant electron cloud impinges on a crossed delay line anode composed of a grid of wires attached to serpentine delay lines in the x and y directions shown in Figure 2.4. The center position of an electron cloud is determined by measuring the time it takes for the imparted charge on each electrode to travel along both directions. The difference in time

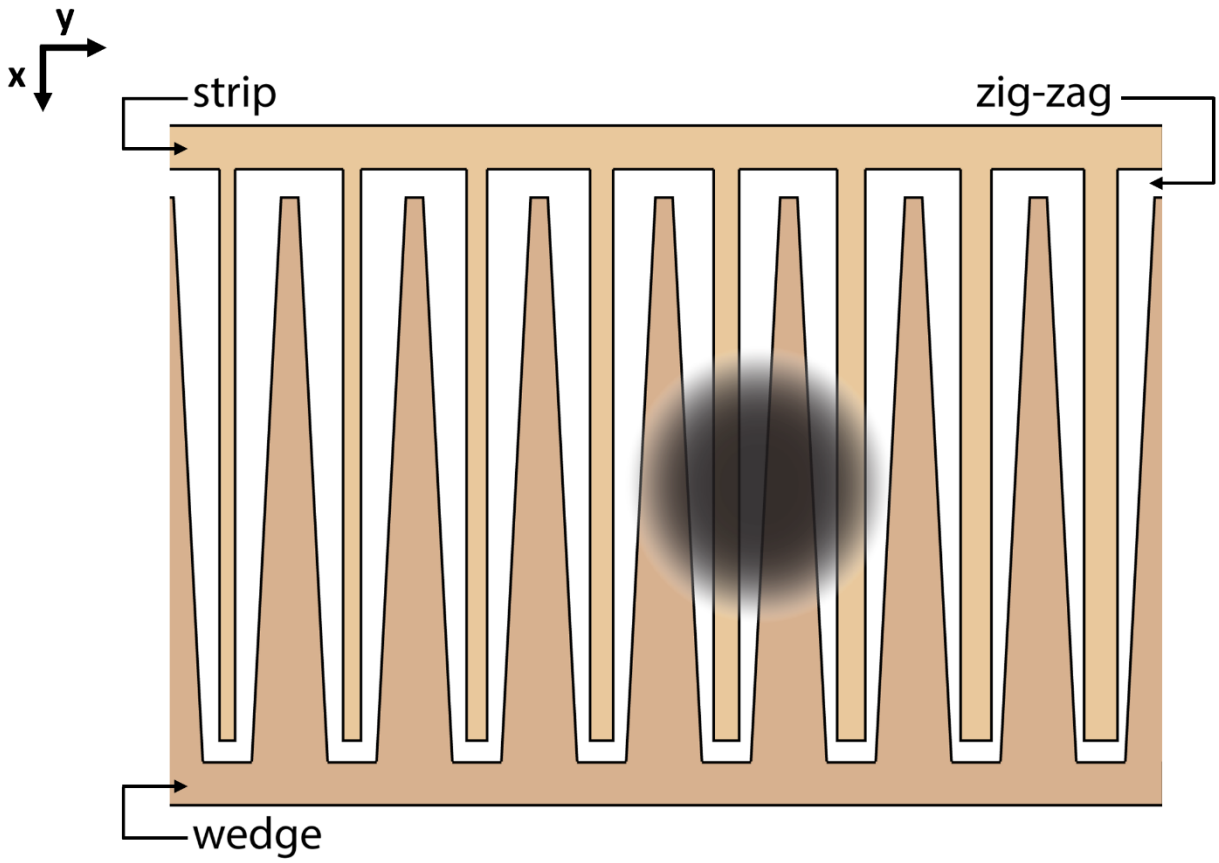

Figure 2.3. Example of the wedge, strip, and zig-zag anode. This illustrates an electron cloud impinging on the anode covering > 1 period of the conductors. (W/S/Z conductors not drawn to scale).

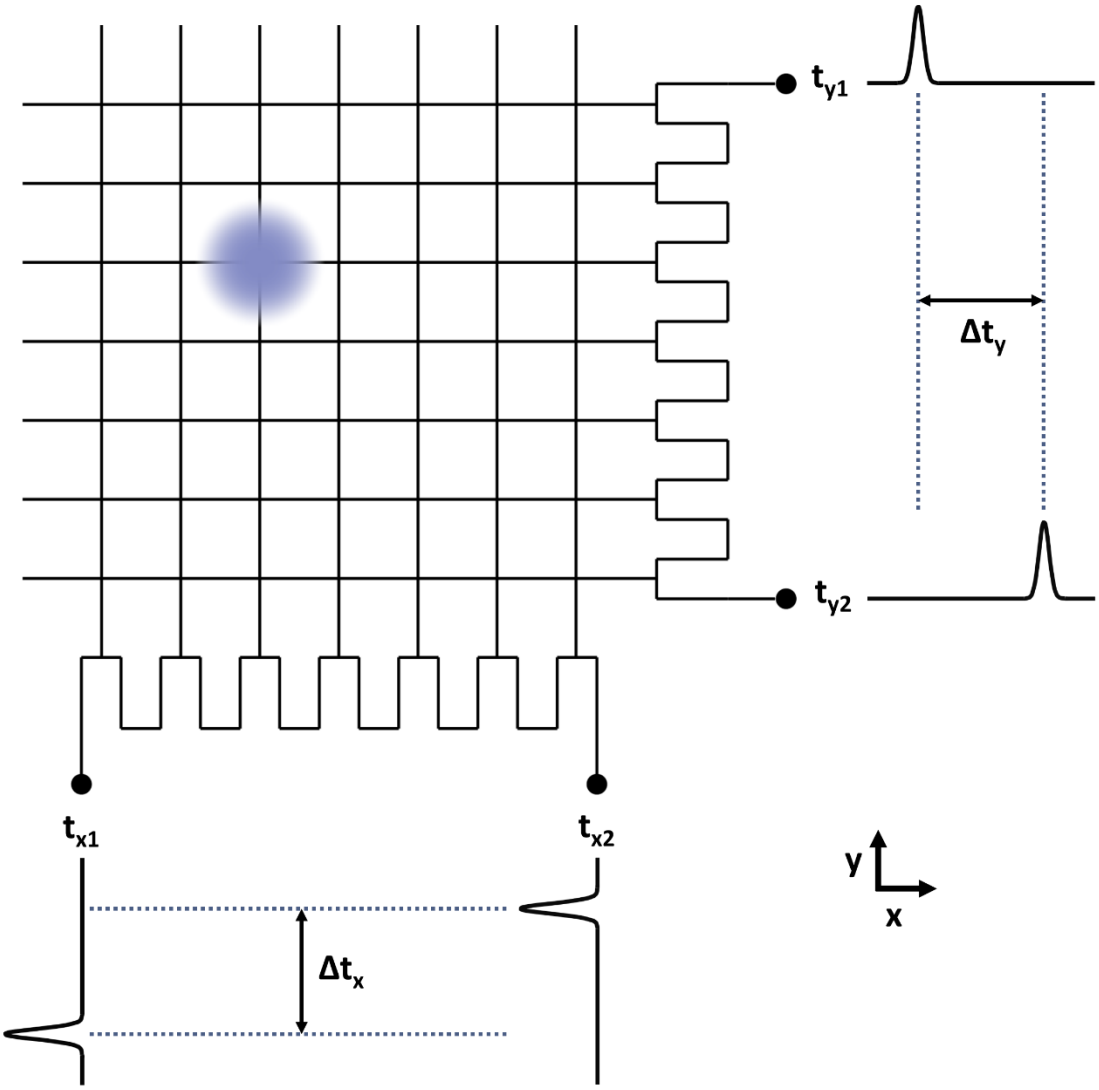

Figure 2.4. Crossed delay-line (XDL) anode schematic. An electron cloud caused by a neutral fragment striking the MCPs impinges on the XDL. The charge is collected at both ends of the serpentine delay lines for the x and y coordinates. The time difference, Δt, yields particle position information.

for both the x and y delay lines can be determined. The following expression is an example for the x direction:

$$\Delta t_x = t_{x1} - t_{x2} = \left(\frac{\frac{l}{2} + x}{v_{eff}}\right) - \left(\frac{\frac{l}{2} - x}{v_{eff}}\right) \tag{2.3}$$

Where l is the length of the serpentine strips, x is the position of the electron cloud alond the x direction, and v_{eff} is the effective velocity of the charge. Rearranging the expression above gives the distance x as:

$$x = \frac{v_{eff} \cdot \Delta t_x}{2} \tag{2.4}$$

The y position is determined in the same way. This technique allows for the detection of two particles impacting the same set of delay lines. The QXDL contains four crossed delay lines allowing for the detection of two particles per quadrant.

2.4.3. Data Acquisition

Following detection of events on the electron and neutral particle detectors, a series of signals are transferred to various sensitive electronics and digitizers. In regards to the electron detector, each signal picked up by the wedge, strip, and zig-zag conductors are amplified using charge-sensitive preamplifiers and each signal is then digitized by a 13-bit Ortec AD413 peak-sensing analog-to-digital converter (ADC). The time of arrival of the electron cloud is measured off the wedge signal with a capacitively coupled fast preamplifier (Ortec VT120) to a constant fraction discriminator (CFD Ortec 935) triggered at 20% of the peak height and serves as a stop signal triggered by a photodiode signal. The CFD receives a start signal from a photodiode that

measures the output of the laser system and serves as the start of the electron TOF. The difference between the start and stop signals are converted to a voltage that is proportional to the difference between the two signals by using a time-to-amplitude (TAC, Ortec 566) and corresponds to the electron TOF. Following the TAC, the signal is sent to another channel on the AD413.

The QXDL collects signals from either side of the serpentine delay lines in both the x and y directions therefore measuring 4 signals in each quadrant allowing up to 8 particles to be detected in coincidence. The signals from each delay line are amplified by a fast preamp and input into custom-designed two-hit TACs (Siegmund Scientific). Each of the 8 double-hit TACS receive a start and stop signal corresponding to the two signals measured on either side of the delay lines in the x or y direction. The valid output signal (determined by setting an adequate gate window to receive the species of interest at the appropriate time-of-arrival) is then digitized using two 8-channel 12-bit peak sensing ADCs (LeCroy Model 3351). The toa for the neutral particles are determined by a TDC (LeCroy Model 3371) that measures a start and stop signal from the x-coordinate TACS. (The start time is determined by a digital pulse set by some delay after the photodiode start signal trigger.) The total charge for each quadrant and the total charge from the MCPs are also amplified and digitized by another ADC (LeCroy 3351). The laser shot information is also recorded using a Hexscaler (Kinetic Systems 3615) which records events by trapping time (usually a 100ms-1s window).

The gating for the various ADCs, TDCs, and TACs is controlled by two digital delay generators (SRS DG535) that are triggered by the laser photodiode signal. These converted signals are then processed by a Computer-Automated Measurement and Control, CAMAC, controller (all housed in a CAMAC crate) which sends the information to the data acquisition PC via a PP004 PC interface adapter to USB. The logic of these signals can be seen in Figure 2.5. The data

acquisition program is written using LabVIEW and outlined more clearly in Chris Johnson's thesis.[14]

2.5. Data Analysis

The raw data collected is saved to a hard drive on a PC and includes the roughly discriminated data containing valid charge events and histograms from the wedge, strip, and zig-zag as well as x, y, and t information from the QXDL generated by the LabVIEW program. The raw data needs to be processed to extract position and timing information of all collected events needed to perform calculations yielding relevant velocity vectors and electron and neutral coincidence data. This information is obtained using a data analysis code written in Interactive Data Language (IDL).

2.5.1. Data Discrimination

All neutral and electron events registered as valid events are recorded and then discriminated. The neutral events are registered as valid if they contain valid x, y, and t information while the electron events must have valid wedge, strip, and zig-zag charges along with a valid time. These events can be discriminated by the multiplicity of events such as electron only, N-neutral particles only, N-particles in coincidence, and N-particles with an electron. These events are grouped and can then be further analyzed in a program in IDL. At this point, the relevant data multiplicity of interest can be sorted for and called into the data analysis program. Each channel can be discriminated further by setting appropriate upper- and lower- level software discriminator limits to remove contributions from bad data or other neutral species events collected in the same timing window.

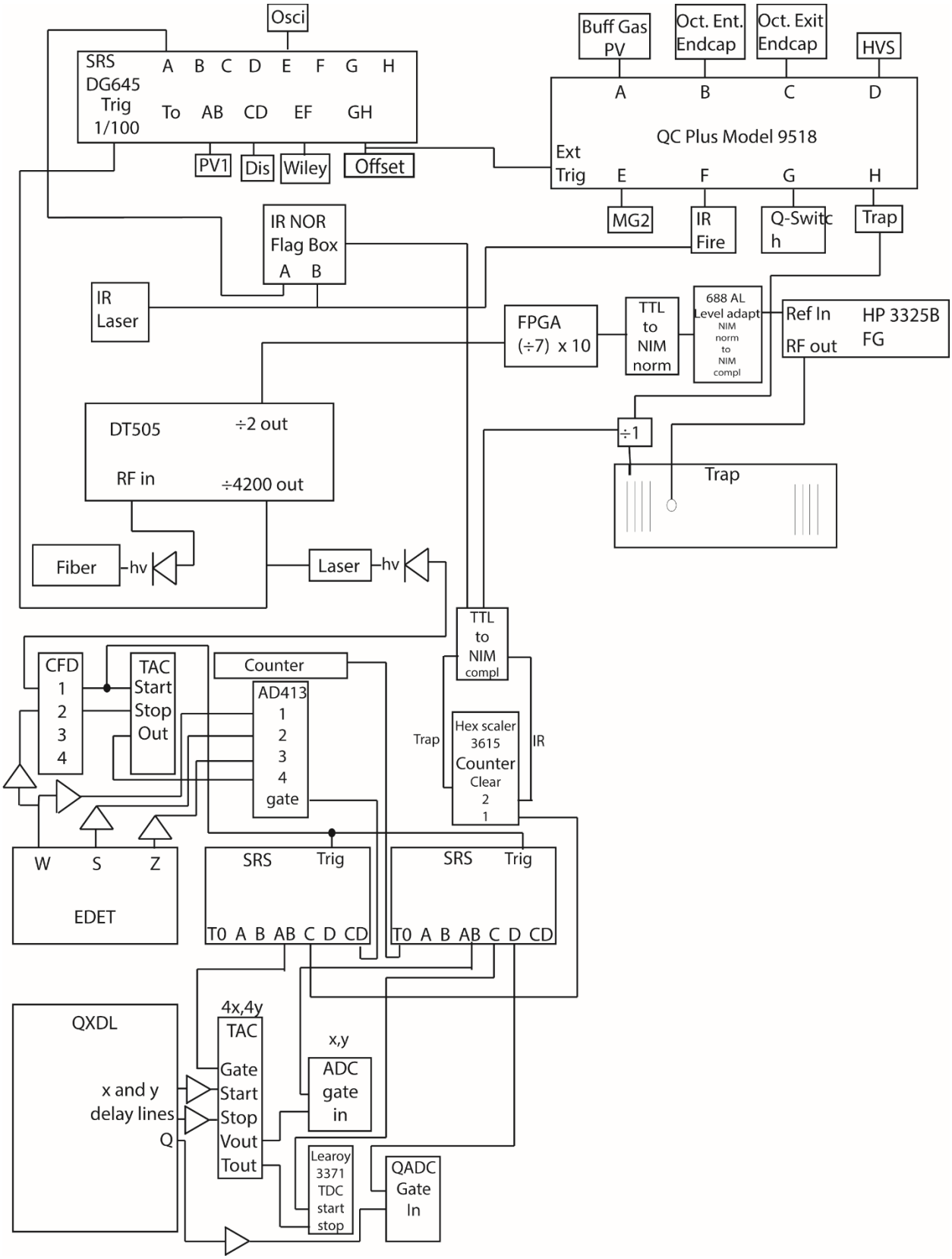

Figure 2.5. Timing signal logic for the PPC spectrometer

2.5.2. Photoelectron Kinetic Energy Calibration

After discrimination of the data, as discussed above, the position and time information can be determined from a series of calibration factors and relations. As mentioned in section 2.4.1., the position information is determined from charge division between the wedge, strip, and zig-zag conductors. Although each are measured independently, these elements are capacitively coupled and therefore, there are calibration factors known as cross-talk factors (CWS, CZW, and CSZ) that need to be determined. There are a series of combinations of these cross-talk factors that have been documented elsewhere but will only be listed here as p_{x1}, p_{y1}, p_{x2}, p_{y2}, p_{x3}, p_{y3}. Additionally, other calibration factors include detector additive constants (DAC) and detector multiplicative constants (DMC). With the inclusion of these corrections and charge divisions between the 3 conductors, the x and y positions of each electron cloud event on the anode can be determined by the following equations:

$$x = DAC_x + DMC_x \frac{\left(Q_w/_{Q_{tot}} - C_{ZW}\right) \cdot p_{x1} - \left(Q_s/_{Q_{tot}} + C_{SZ}\right) \cdot p_{x2}}{p_{x3}} \tag{2.5}$$

$$y = DAC_y + DMC_y \frac{\left(Q_s/_{Q_{tot}} - C_{SZ}\right) \cdot p_{y1} - \left(Q_x/_{Q_{tot}} + C_{ZW}\right) \cdot p_{y2}}{p_{y3}} \tag{2.6}$$

Where Q_w, Q_s, and Q_{tot} are the wedge, strip, and total ($Q_w + Q_s + Q_z$) charge, respectively. The electron time of arrival must also be determined and this is also done by using DAC and DMC factors:

$$TOF = DMC_t \cdot t_e + DAC_t \tag{2.7}$$

Where t_e corresponds to the time of arrival of the photodetached electron on the anode. These calibration factors and offsets can then be adjusted and calibrated from known electron affinities

and electronic transitions from species like O^- and O_2^-. It should be noted that additional corrections are made in determining the x, y, and t velocity vectors to account for focusing effects of the VMI setup which distorts the otherwise spherical distribution of recoiling photoelectrons. After which the electron kinetic energy (eKE) can be calculated:

$$eKE = {}^1/_2\, m_e(v_x^2 + v_y^2 + v_z^2) \tag{2.8}$$

2.5.3. Neutral Fragment Kinetic Energy Calibration

The calibration for the QXDL is much more straightforward than that of the electron detector. The calculations described here are for 2-body dissociation processes which are the processes of interest in this thesis. As previously noted, the QXDL consists of 4 quadrants each with separate delay lines allowing for the detection of up to 2 particles per dissociation event for a total of 8 particles. The position information is obtained from time measurements as opposed to charge information from the W/S/Z anode detector thus eliminating crosstalk factors between the conductors and simplifying the expressions for determining x and y positions on the QXDL. These positions are calculated for each quadrant by the following equations:

$$x = DMC_x \cdot x_{TAC} + DAC_x \tag{2.9}$$

$$y = DMC_y \cdot y_{TAC} + DAC_y \tag{2.10}$$

Where DMC_x and DMC_y are multiplicative factors, x_{TAC} and y_{TAC} are values taken from the TAC, and DAC_x and DAC_y are additive constants. The multiplicative and additive constants are manually adjusted following a calibration procedure using the DPD of O_4^- which has a known KER.[24] The time of arrival of the fragment is a little more involved but in general can be determined by the following expression:

$$t = DMC_t \cdot [(t_{TDC} + DAC_t) + t_{DL} \cdot x] \quad (2.11)$$

Where t_{DL} is a constant that accounts for the time delay between the fragment impact on the detector (picked up by the x delay line) and the timing at the end of the delay line. After determining the laboratory-frame time and positions, the fragment velocities can be calculated by the following expressions:

$$v_x = x/TOF_{CM} \quad (2.12)$$

$$v_y = y/TOF_{CM} \quad (2.13)$$

$$v_z = v_{beam} \cdot (TOF - TOF_{CM}) \quad (2.14)$$

Where TOF_{CM} is the TOF for the center of mass and v_{beam} is the ion beam velocity. The flight path of 1.31 m from the interaction region to the QXDL is used to determine TOF_{CM} so dissociations that occur along the beam path will have a slightly different flight path distance, however, for KER < 1 eV this deviation is negligible and not considered in the velocity calculations here.

To determine the CM vector, the masses of the fragment particles must be guessed then conservation of momentum can be enforced for each event. The kinetic energy release (KER) for two fragments can then be determined by the following equation:

$$KER = \frac{1}{2}\sum_{i}^{2} m_i \cdot v_i^2 \quad (2.15)$$

Where m_i is the mass and v_i is the velocity vector of the *ith* fragment.

2.5.4. Gating

After the position, time, and subsequent energy calculations are performed, the data set must then be gated in various ways to reduce noise contributions, enhance the resolution of data for proper analysis, and select for specific data sets. Events that are registered in the data acquisition program as valid events may consist of bad data points due to false coincidences. False coincidences are a result of various factors such as border events (a particle hits the intersection of two quadrants on the QXDL and is registered as 2 events) and correlations of two neutrals from different photodetachment events. Spherical and centroid gating for stable and dissociative events also helps to remove contributions from different mass species contained in the same data sets and enforces electron correlations to the selected neutral(s) of interest. Additionally, if there are large differences in the CM spectrum, different fragmentation channels can be gated from other dissociation channels of the same parent species. Charge gating can also be performed to discriminate against 1 and 2 particle events on the QXDL, however, this has not been shown to improve the quality of the data analysis in this program.

Unlike the QXDL, the photoelectron detector is only capable of collecting single event electrons on an event-by-event basis. The largest uncertainty stems from the timing information due to the non-linear VMI effects. Generally, v_z contains the largest error compared to v_x and v_y since the timing resolution is ~200 ps over ~10 ns range. The overall error in energy calculations depends on the magnitude of the x, y, and z velocity vectors:

$$\frac{\delta E}{E} \propto \frac{2(v_x \delta v_x + v_y \delta v_y + v_z \delta v_z)}{v_x^2 + v_y^2 + v_z^2} \tag{2.16}$$

Decreasing the magnitude of the uncertainty in any of these velocity vectors therefore improves the overall energy resolution. Selecting for a narrow center distribution of v_z helps to

reduce error contributions, these are low-energy electrons and electrons parallel to the electric vector of the laser. This type of electron slicing significantly decreases the events for data analysis so it should only be used if there's sufficient event statistics. Additionally, a correction must be made known as the detector acceptance function (DAF)[27] to correct for changes in relative intensities of the photoelectron velocity vectors. An example of this gating process as well as the DAF correction can be seen in Figure 2.6.

2.5.5. Coincidence Calculations

After the energy calculations are performed and properly gated for photoelectrons and photofragments, the total energy of a dissociation event can be determined:

$$E_{tot} = eKE + KER \tag{2.17}$$

A coincidence spectrum can also be obtained by plotting the KER histogram versus the eKE histogram showing the probability of any combination of eKE and KER data. This plot, described in section 1.4. of Chapter 1, reveals distinct features along the diagonal axis corresponding to the Franck Condon region associated with the precursor anion and the repulsive monotonic asymptotic curve of the neutral surface. These coincidence plots contain valuable information about the partitioning of energy in a dissociation event such as the branching to other channels, vibrational excitation in the photofragments, autodetachment events (not addressed here), and photodissociation processes.

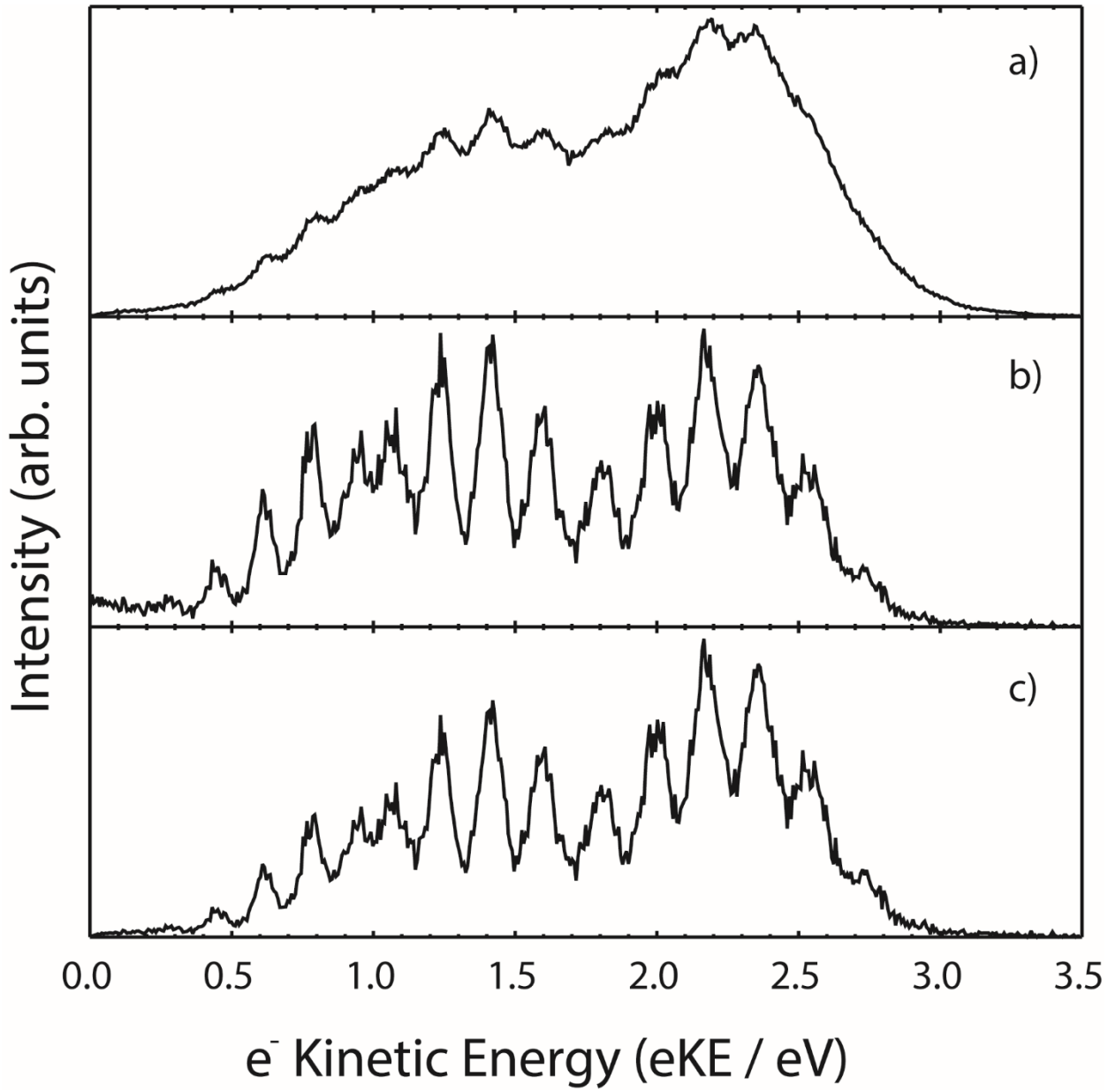

Figure 2.6. Photoelectron spectra of O_2^-. The photoelectron spectra for raw, electron sliced, and DAF correction after slicing are shown in a), b), and c), respectively.

2.6. References

1. Hanold, K. A.; Luong, A. K.; Clements, T. G.; Continetti, R. E., Photoelectron–multiple-photofragment coincidence spectrometer. *Review of Scientific Instruments* **1999,** *70* (5), 2268-2276.

2. Johnson, C. J.; Shen, B. B.; Poad, B. L. J.; Continetti, R. E., Photoelectron-photofragment coincidence spectroscopy in a cryogenically cooled linear electrostatic ion beam trap. *Rev. Sci. Instrum.* **2011,** *82* (10), 105105.

3. Shen, B. B.; Benitez, Y.; Lunny, K. G.; Continetti, R. E., Internal energy dependence of the photodissociation dynamics of O_3^- using cryogenic photoelectron-photofragment coincidence spectroscopy. *J. Chem. Phys.* **2017,** *147* (9), 094307.

4. Levy, D. H., The Spectroscopy of Very Cold Gases. *Science* **1981,** *214* (4518), 263-269.
5. van de Meerakker, S. Y. T.; Bethlem, H. L.; Meijer, G., Taming molecular beams. *Nature Physics* **2008,** *4* (8), 595-602.

6. Wiley, W. C.; McLaren, I. H., Time-of-Flight Mass Spectrometer with Improved Resolution. *Rev. Sci. Instrum.* **1955,** *26* (12), 1150-1157.

7. Shen, B. B.; Lunny, K. G.; Benitez, Y.; Continetti, R. E., Photoelectron-Photofragment Coincidence Spectroscopy With Ions Prepared in a Cryogenic Octopole Accumulation Trap: Collisional Excitation and Buffer Gas Cooling. *Front. Chem.* **2019,** *7*, 295.

8. Shen, B. B. Preparation of Hot and Cold Ions for Photoelectron-Photofragment Coincidence Spectroscopy. University of California, San Diego, San Diego, 2018.

9. Wester, R., Radiofrequency multipole traps: tools for spectroscopy and dynamics of cold molecular ions. *Journal of Physics B: Atomic, Molecular and Optical Physics* **2009,** *42* (15), 154001.

10, Endres, E. S.; Egger, G.; Lee, S.; Lakhmanskaya, O.; Simpson, M.; Wester, R., Incomplete rotational cooling in a 22-pole ion trap. *Journal of Molecular Spectroscopy* **2017,** *332*, 134-138.

11. Ray, A. W. Dissociation Dynamics of Transient Molecules Studied by Photoelectron-Photofragment Coincidence Spectroscopy. University of California, San Diego, San Diego, 2016.

12. Bakker, J. M. B., A beam-modulated time-of-flight mass spectrometer. II. Experimental work. *Journal of Physics E: Scientific Instruments* **1974,** *7* (5), 364-368.

13. Dahan, M.; Fishman, R.; Heber, O.; Rappaport, M.; Altstein, N.; Zajfman, D.; van der Zande, W. J., A new type of electrostatic ion trap for storage of fast ion beams. *Review of Scientific Instruments* **1998,** *69* (1), 76-83.

14. Johnson, C. J. Investigation of the reaction of OH and CO to form H and CO_2 by Photoelectron-Photofragment Coincidence spectroscopy in a cryogenic ion beam trap. University of California, San Diego, San Diego, 2011.

15. Lunny, K. G. Investigation of Reactive Oxides and Radical Dynamics by Photoelectron-Photofragment Coincidence Spectroscopy. University of California, San Diego, San Diego, 2019.

16. Continetti, R. E., Photoelectron-photofragment coincidence studies of dissociation dynamics. *International Reviews in Physical Chemistry* **1998,** *17* (2), 227-260.

17. Lai, M.; Lai, S. T.; Swinger, C., Single-grating laser pulse stretcher and compressor. *Applied Optics* **1994,** *33* (30), 6985-6987.

18. Hänsch, T. W., Nobel Lecture: Passion for precision. *Reviews of Modern Physics* **2006,** *78* (4), 1297-1309.

19. Siegmund, O. H. W.; Coburn, K.; Malina, R. F., Investigation of Large Format Microchannel Plate Z Configurations. *IEEE Transactions on Nuclear Science* **1985,** *32* (1), 443-447.

20. Martin, C.; Jelinsky, P.; Lampton, M.; Malina, R. F.; Anger, H. O., Wedge-and-strip anodes for centroid-finding position-sensitive photon and particle detectors. *Review of Scientific Instruments* **1981,** *52* (7), 1067-1074.

21. Siegmund, O. H. W.; Malina, R. F.; Coburn, K.; Werthimer, D., Microchannel Plate EUV Detectors for the Extreme Ultraviolet Explorer. *IEEE Transactions on Nuclear Science* **1984,** *31* (1), 776-779.

22. Friedman, P. G.; Cuza, R. A.; Fleischman, J. R.; Martin, C.; Schiminovich, D.; Doyle, D. J., Multilayer anode with crossed serpentine delay lines for high spatial resolution readout of microchannel plate detectors. *Review of Scientific Instruments* **1996,** *67* (2), 596-608.

23. Harrison, A. W.; Ryazanov, M.; Sullivan, E. N.; Neumark, D. M., Photodissociation dynamics of the methyl perthiyl radical at 248 and 193 nm using fast-beam photofragment translational spectroscopy. *The Journal of Chemical Physics* **2016,** *145* (2), 024305.

24. Sherwood, C. R. Dissociative Photodetachment and Photodissociation Dynamics of Cluster Anions. University of California, San Diego, San Diego, 1995.

25. Clements, T. G. Multi-Body Dissociative Photodetachment Dynamics of Small Molecular and Cluster Anions. University of California, San Diego, San Diego, 2002.

26. Hanold, K. A.; Continetti, R. E., Photoelectron–photofragment coincidence studies of the dissociative photodetachment of O_4^-. *Chem. Phys.* **1998,** *239* (1), 493-509.

27. Bowen, M. S.; Continetti, R. E., Photodetachment Imaging Study of the Vinoxide Anion. *J. Phys. Chem. A* **2004,** *108* (39), 7827-7831.

Chapter 3: Photoelectron-Photofragment Coincidence Studies on the Dissociation Dynamics of the OH-CH_4 Complex

3.1. Introduction

Radical-molecule reactions play an important role in understanding both atmospheric and combustion chemistry.[1] The elementary reaction OH + CH_4 → H_2O + CH_3 is the simplest reaction of the hydroxyl radical with an alkane. Methane is the most abundant saturated hydrocarbon in the troposphere, making this process atmospherically relevant as it governs the concentration of hydroxyl radicals by providing a chemical sink for both CH_4 and OH.[2,3] The high reactivity of OH is significant since it initiates radical-chain oxidation in the troposphere and is an important chain carrier in combustion processes of high temperature methane flames.[4] In addition, this reaction is one of the elementary steps involved in the oxidation of methane and is therefore important in understanding the oxidative characteristics of fuels. Because of the pertinence of this reaction in atmospheric and combustion chemistry, it has been studied experimentally[2,5–7] and at various levels of theory[8–18] to understand the reaction barrier and rate coefficients, as well as kinetic isotope effects. Although there are numerous kinetic studies on this reaction, there are few experimental studies on the reaction dynamics.

Lester and coworkers studied vibrational predissociation of OH-CH_4 in the entrance channel by selective vibrational excitation of the complex leading to production of either the reactants (OH + CH_4) or the products (H_2O + CH_3) of the reaction.[19–21] Interpretation of the experiments were aided by *ab initio* calculations on the structure of the minimum energy configuration of the entrance channel van der Waals complex, with the hydroxyl hydrogen oriented towards the tetrahedral face of methane. In those experiments, stimulated Raman or IR excitation of the symmetric or asymmetric stretches of CH_4 or the OH stretch were examined to determine if

the relatively low activation energy required for reaction could be overcome. It was determined that vibrational excitation was effective in promoting fission of the weak intermolecular bond, yielding the entrance channel reactants OH + CH_4. These studies produced the first IR spectra of the entrance channel complex *via* action spectroscopy, as well as insight into the decay dynamics.

A series of studies on the dynamics of the OH + $CH_4 \rightarrow H_2O$ + CH_3 reaction and isotopologs by Liu and coworkers[22–24] were performed using crossed-beam experiments over collision energies from 0.2-0.7 eV. These experiments used vibrationally state-resolved photoion imaging to characterize how energy partitioning in the H_2O + CH_3 product channel resulted in correlations in the modes excited in the product pairs. They found that the vibrational ground state of methyl radical was the dominant product and vibrational excitation in HOD/H_2O co-products was primarily localized in the newly formed OD/OH bond. These experiments inspired theoretical calculations to improve on knowledge of the potential energy surface (PES) of this reaction.

This seven-atom system is challenging to study theoretically since the construction of reliable PES's becomes difficult, especially for a system including two heavy atoms. Espinosa-Garcia and coworkers recently reported a full-dimensional analytical PES (PES-2014) for the OH + $CH_4 \rightarrow H_2O$ + CH_3 reaction.[25] This PES has been used to investigate the kinetics and dynamics of the reaction with good general agreement with experiment.[16,17,25,26] Quasi-classical trajectory (QCT) calculations were carried out to examine isotope effects in the reaction, inspired by the experimental studies of Liu and co-workers, calculating product translational and vibrational distributions at 10 kcal/mol and 298 K.[17,25] The agreement between theory and experiment was only qualitative, indicating that efforts to improve the accuracy and quality of the PES, as well as studies of the quantum dynamics of the system, would be worthwhile. Since then, several high-dimensional quantum dynamics studies have been reported using this PES.[27,28] However, the

relatively simple form used to fit PES-2014 remains as a source of uncertainty. Only regions near the minimum energy path of the reaction were well described in PES-2014, and the accuracy of the high-energy regions is limited.[16] To further improve the accuracy of the PES, Li and Guo constructed a globally accurate PES for this reaction based on a large number of high-level *ab initio* points along the reaction path, providing an accurate description of the PES in all relevant configurations of this system.[15] Rate coefficients and kinetic isotope effects, as well as dynamical results computed using this PES were found to agree well with available experimental data.[18,29]

In the present work, the dynamics of the $OH + CH_4 \rightarrow H_2O + CH_3$ reaction on the neutral PES are studied using photoelectron-photofragment coincidence (PPC) measurements at a photon energy $E_{h\nu} = 3.20$ eV. These experiments use photodetachment of a precursor anion to observe the ensuing neutral dynamics. This approach complements the crossed molecular beam and spectroscopic studies mentioned above because it probes dynamics initiated near the anion equilibrium geometry.[30] Recently, this approach has been successfully used to reveal key aspects of the dynamics of several prototypical reactions.[31] The photodetachment scheme for the current system is shown in Figure 3.1., detailing the relevant reaction pathway for the $OH + CH_4$ reaction with geometries and energies for the precursor anion, entrance and exit channel van der Waals complexes, and the transition state. In the present work, photoelectron spectra are reported for both dissociative, $OH^-(CH_4) + h\nu \rightarrow OH + CH_4 + e^-$, and stable, $OH^-(CH_4) + h\nu \rightarrow OH(CH_4) + e^-$, channels. The overall partitioning of kinetic energy in the dissociative photodetachment (DPD) processes is examined using PPC spectra for the $OH^-(CH_4)/OH^-(CD_4)/OD^-(CD_4)$ isotopologs at $E_{h\nu} = 3.20$ eV. These PPC experiments are complemented by theoretical studies using the neutral PES reported earlier[15] and a newly constructed anion PES. The dynamics on the neutral PES is simulated using QCT calculations with initial conditions sampled from the anion Wigner

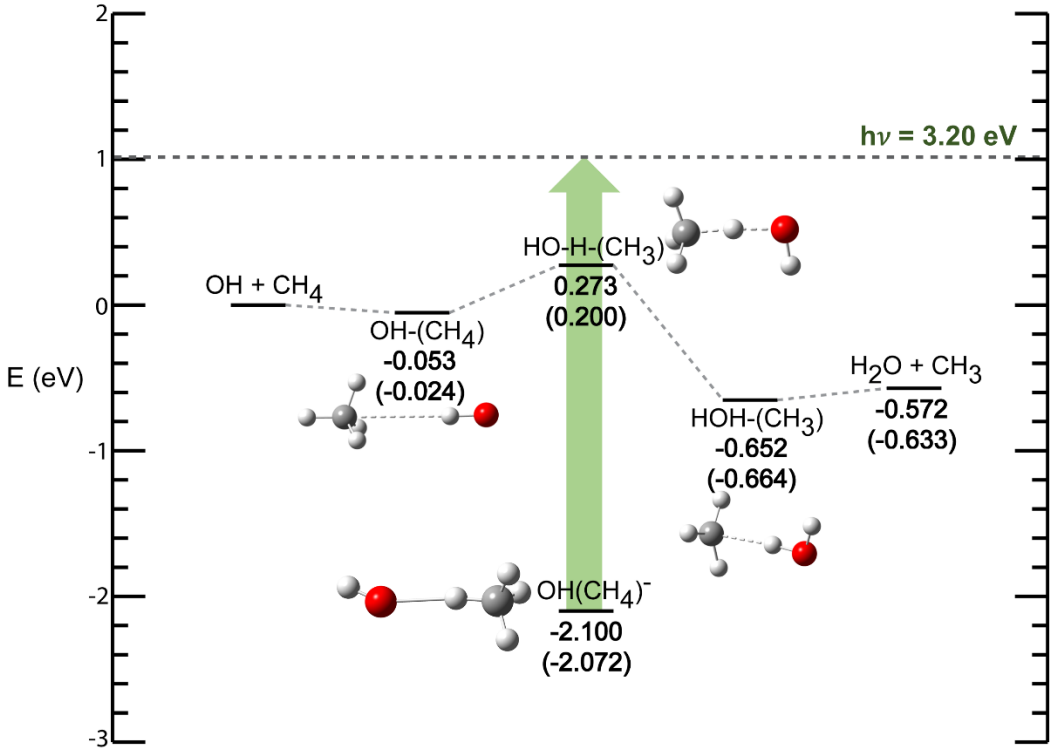

Figure 3.1. The reaction scheme for the OH + CH_4 → H_2O + CH_3 neutral reaction along with geometries and energetics for the entrance and exit channel van der Waals complexes and transition state.[15] Also included is the precursor anion calculated at the CCSD(T)-F12a/AVTZ level of theory. All energies are in eV relative to the reactant asymptote OH + CH_4 without zero-point energy corrections. (Zero-point energy corrected values are in parentheses).

distribution. The theoretical results provide insights that help interpret the experimental observations of stable and dissociative photodetachment and the energy partitioning.

3.2. Experiment

These experiments were carried out using the cryo-PPC spectrometer described previously.[32,33] This apparatus uses a radio frequency (RF) cryogenic octopole accumulation trap (COAT) for the preparation of internally cold precursor anions prior to injection into the electrostatic ion beam trap (EIBT) where the coincidence experiments are performed.[34] For these experiments, however, COAT was not utilized. In brief, anions were synthesized using a dual pulsed valve entrainment source at a 10 Hz repetition rate. The dual pulsed valve setup allowed for a plasma generated in a side discharge expansion to be entrained into the high density region of the main molecular expansion.[35] A low gas density flow of 5:45:50 N_2O, Ar, CH_4/CD_4, respectively, passed through a coaxial pulsed discharge generating a plasma that then intersected a pulsed supersonic beam of a 10% of CH_4/CD_4 in Ar, entraining hydroxide anions and allowing subsequent interactions with CH_4/CD_4. A 1 keV electron beam counterpropagating with the main expansion was used to stabilize the discharge. This setup can be seen in Figure 3.2. Using the dual pulsed valve source allowed for the creation of jet-cooled anions and a rational approach to synthesizing anions of interest, in particular $OH^-(CH_4)/OH^-(CD_4)/OD^-(CD_4)$ anion complexes.

The anions were perpendicularly extracted using a Wiley-McLaren time-of-flight (TOF) mass spectrometer,[36] accelerated to 7 keV, then re-referenced to ground using a fast potential switch. The anion packets (typically 2-5 μs long) were separated by TOF, focused, and steered into a cryogenically cooled EIBT where the mass selected ions were trapped for 100 ms. The trapped ions were then crossed with a 1037 Hz, 388 nm ($E_{h\nu}$ = 3.20 eV) laser pulse from a Ti:Sapphire regenerative amplifier (Clark MXR CPA-2000; 1.1 ps pulse width) over the course of

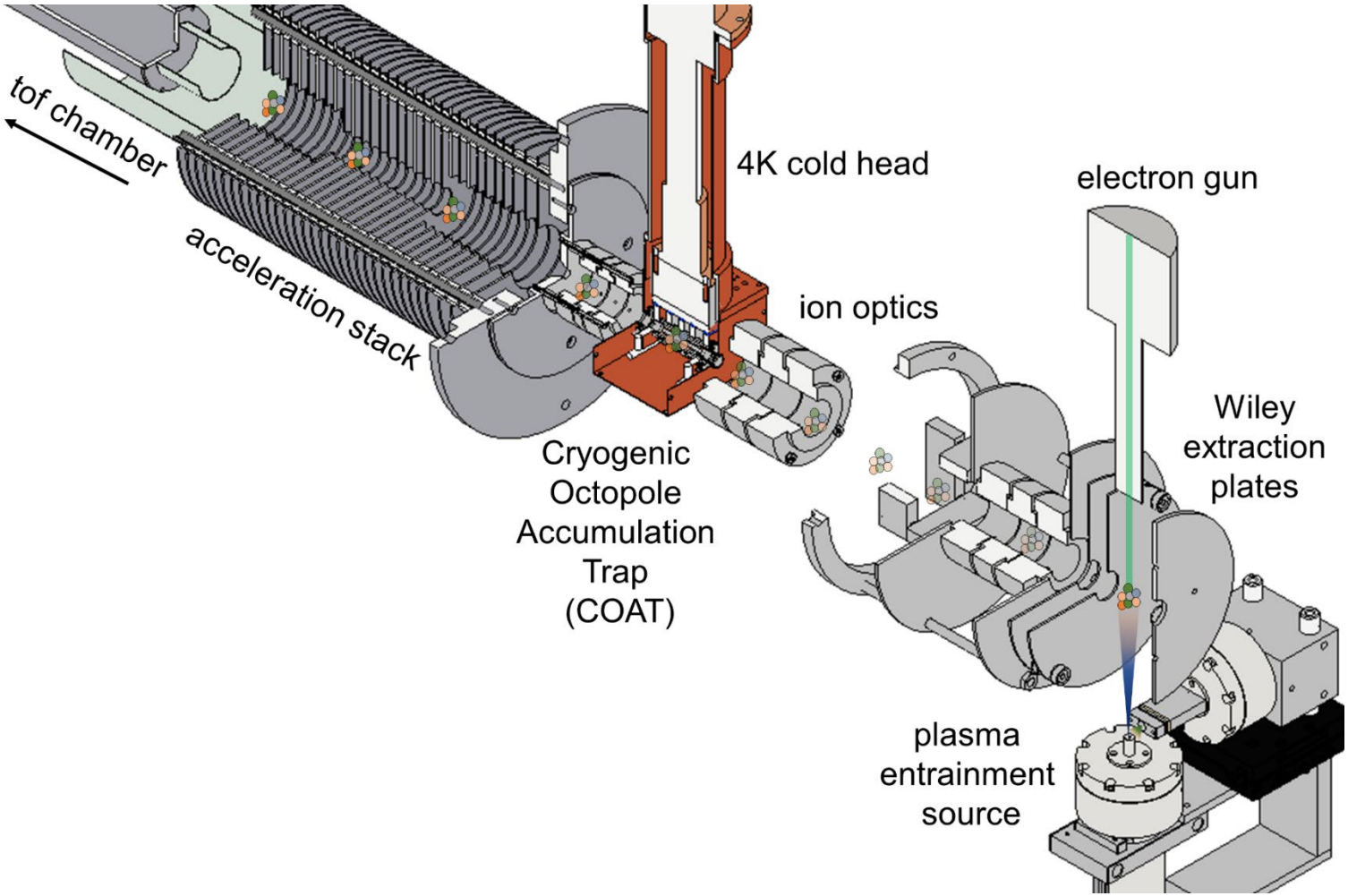

Figure 3.2. Schematic of source section comprising of the dual pulsed valve entrainment source, Wiley extraction plates, ion optics, COAT, and acceleration stack.

the 100 ms trapping period per experimental cycle, and the resultant electron and neutral fragment(s) were collected.

Photoelectrons were perpendicularly extracted from the laser-ion interaction region and mapped with electrostatic lenses onto a time and position sensitive detector that allowed the center-of-mass electron kinetic energy (eKE) for each one to be determined. Equatorially slicing the photoelectron spectra by selecting electrons with minimal z-velocities perpendicular to the face of the detector gives the best resolution. Correcting for relative intensities in the photoelectron spectra was achieved by dividing the sliced photoelectron spectra by the energy-dependent acceptance function of the z-velocity slice.[37] Calibration spectra of O_2^- and OH^- showed ΔeKE/eKE resolution of 4% full-width-half-max (FWHM) at eKE = 1.59 eV (using the $\boldsymbol{a}$(v=1) ← $\boldsymbol{X}$(v=0) transition) and 1.36 eV, respectively.

Upon photodetachment, the resultant neutrals are no longer constrained by the electrostatic fields and recoil out of the EIBT, impinging on a multiparticle time and position sensitive detector ~1.3 m downstream allowing the product mass ratio and kinetic energy release (KER) for dissociation events to be determined. This quad-crossed-delay-line (QXDL) detector was calibrated by collecting a dissociative photodetachment (DPD) spectrum of O_4^- showing a ΔKER/KER resolution of ~10% FWHM at 0.4 eV.[38] Stable events detected by the QXDL arrived in a spot ~4 mm in diameter. Dissociative events, on the other hand, are distributed across the face of the QXDL as determined by the KER and the fragment mass ratio. In the present study, the dissociative events have a very low KER which blend in with the stable events making it challenging to distinguish between low KER events and stable events. In addition, the center of mass distribution has limited mass resolution, so channels with fragment masses which differ by

1 amu are unresolvable. Thus, OH + CH_4 and H_2O + CH_3 fragment masses cannot be resolved experimentally.

3.3. Theory

In order to simulate the PPC process starting from the $OH^-(CH_4)$ anion equilibrium, PESs for both the anion and its corresponding neutral are required. In 2015, a globally accurate full-dimensional PES with fifteen internal coordinates for the neutral reaction, namely, OH + CH_4 → H_2O + CH_3, was developed by Li and Guo based on ~135,000 *ab initio* points at the explicitly correlated coupled cluster singles, doubles, and perturbative triples level with the augmented correlation corrected valence triple-zeta basis set (UCCSD(T)-F12a/AVTZ).[15] The zero point energy (ZPE) corrected barrier height for the reaction is 0.200 eV. The ZPE-corrected reaction enthalpy is -0.633 eV, which is consistent with the Active Thermochemical Tables (ATcT) value, -0.620 eV.[39] Note that the spin-orbit effect is not included in the reactant channel, which increases the barrier height by 0.009 eV, and shifts the reaction enthalpy to -0.624 eV. The *ab initio* points were fit using the permutation invariant polynomial-neural network (PIP-NN) approach,[40] resulting in a total root-mean square error (RMSE) of only 3.9 meV. Kinetic and dynamical calculations on the neutral PES indicated a good agreement with available experimental data, thus validating the global accuracy of the neutral PES.[15,18,29]

For the anion PES, it is sufficient for our purposes to sample only configurations around the local region near the anion equilibrium. Approximately 15,000 points were computed at the level of CCSD(T)-F12a/AVTZ and fit with the same PIP-NN method. With 3 and 100 neurons in the first and second hidden layers, resulting in 4497 parameters, the final anion PES has 5.1 meV

RMSE. Detailed information about the geometry and harmonic frequencies of the anion and the fitting error distribution can be found in the Supplemental Information (SI).

To simulate the photodetachment dynamics, the Condon approximation is assumed such that the positions and momenta of all atoms are conserved during the photon-induced ejection of the electron. A quantum mechanical treatment of the fifteen-dimensional dynamics is currently unattainable, so the photodetachment dynamics is simulated in this work by a QCT method. To account for quantum effects, the initial conditions of the trajectories were selected based on the Wigner approach, initially suggested by Heller.[41] This approach has been shown to provide a better description of initial conditions in photoexcited processes.[42,43]

For a system of n normal modes (here n=15), the vibrational energy is approximated as the sum of energies for separable harmonic oscillators, namely,

$$E = \sum_{i=1}^{n} E_i = \sum_{i=1}^{n} \frac{P_i^2 + \omega_i^2 Q_i^2}{2} \tag{1}$$

Note that in **Eq. (1)**, the mass weighted coordinate system is used, namely, $Q_i = \sqrt{\mu_i}\, x_i$ and $P_i = \sqrt{\mu_i}\dot{x}_i = \dot{Q}_i = dQ_i/dt$, where μ_i is the reduced mass of the normal mode. For this system, the corresponding Wigner distribution function W(**Q**, **P**) is approximated by a product of all one-dimensional harmonic oscillator distribution functions:[44]

$$W(\mathbf{Q},\mathbf{P}) = \prod_{i=1}^{n} W(Q_i, P_i) \tag{2}$$

For the ground vibrational state of the system, the Wigner distribution function is simple:

$$W^{v=0}(\mathbf{Q},\mathbf{P}) = \prod_{i=1}^{n} W^{v=0}(Q_i, P_i) = \prod_{i=1}^{n} \frac{1}{\pi\hbar} e^{-\left(P_i^2+\omega_i^2 Q_i^2\right)/(\omega_i\hbar)} \quad (3)$$

In this work, the sampling is carried out independently for each normal mode. Specifically, we follow the following protocol. For the i^{th} mode,

(i) A phase space point (P_i, Q_i) is first randomly selected. A +/- sign is randomly assigned.

(ii) Then, $W(P_i, Q_i)$ is calculated and compared to the most probable value of $W(P_i, Q_i)$, $W_{\max}$. If $W/W_{\max} > R$, which is a uniformly distributed fresh random number, accept this point. Otherwise go back to step (i) to choose another random phase space point.

(iii) For all normal modes, the (P_i, Q_i) are sampled and then transformed to Cartesian coordinates in the same manner as for quasi-classical sampling.

In the QCT simulations of the PPC experiment, no energy resolution was attempted because only comparison with the total KER is needed. Instead, trajectories with the aforementioned initial coordinates and momenta were propagated using combined fourth-order Runge-Kutta and sixth-order Adams-Moulton algorithms implemented in VENUS[45] and included in the final analysis. At the end of the trajectory, the vibrational quantum numbers were assigned using the normal mode analysis (NMA) method.[46–48] Since the uncoupled harmonic approximation was used in the NMA calculation, it may break down for highly excited states due to anharmonicity. Finally, the normal mode energies were used to find the vibrational quantum numbers, using histogram binning. A total of 4000 trajectories were calculated.

3.4. Results

In this section, photoelectron spectra for stable and dissociative OH-CH_4 complexes will be presented followed by PPC spectra that reveal the partitioning of kinetic energy between

photoelectron and photofragments. Finally, total kinetic energy release spectra, E_{TOT} = eKE + KER on an event-by-event basis, for the $OH^-(CH_4)/OH^-(CD_4)/OD^-(CD_4)$ isotopologs are presented.

3.4.1. Photodetachment of $OH^-(CH_4) + h\nu \rightarrow OH\text{-}CH_4 + e^-$

The photoelectron spectra for stable complexes are generated from the data set by enforcing coincidence of the detected photoelectron with a single heavy particle arriving at the position and time-of-arrival expected for the neutralized parent anion. This stable channel makes up ~26% of the total stable and dissociative events collected. In Figure 3.3. the stable photoelectron spectrum for OH^- (grey trace) is compared to $OH^-(CH_4)$ (black trace) at $E_{h\nu}$ = 3.20 eV. The peak at eKE = 1.36 eV corresponds to photodetachment of OH^- at m/z = 17, within 0.01 eV of the expected value given the 1.83 eV AEA for OH.[49] The $OH^-(CH_4)$ spectrum (m/z = 33) is dominated by a peak at eKE = 1.09 eV and a small shoulder at eKE = 0.70 eV. In addition, a minor broad feature is seen centered at ~2.2 eV due to HOO^- (m/z = 33) contamination. The photoelectron spectra of $OH^-(CH_4)$ and OH^- are similar, consistent with the electronic structure of $OH^-(CH_4)$ resembling a hydroxyl anion core. The dominant peak in the photoelectron spectra is broadened by 0.04 eV compared to OH^- because of excitation of low-frequency van der Waals modes of the neutral complex. The shoulder ~0.4 eV lower in eKE can be due to excitation of the symmetric and asymmetric CH_4 stretches (3070 or 3203 cm^{-1}, respectively, in CH_4) or the OH fundamental stretch (3821 cm^{-1} in OH).[20] The experimental VDE for the stable complexes is determined by the center of the dominant peak in the total (dissociative and stable) photoelectron spectrum, and found to be 2.14 eV. The total eKE peak center used for determining the experimental VDE is listed in Table 3.1.

Insight into the internal energy dependence of the dissociation dynamics of the $OH(CH_4)$ complexes can be gained by comparing the stable photoelectron spectrum for $OH(CH_4) + e^-$ to the

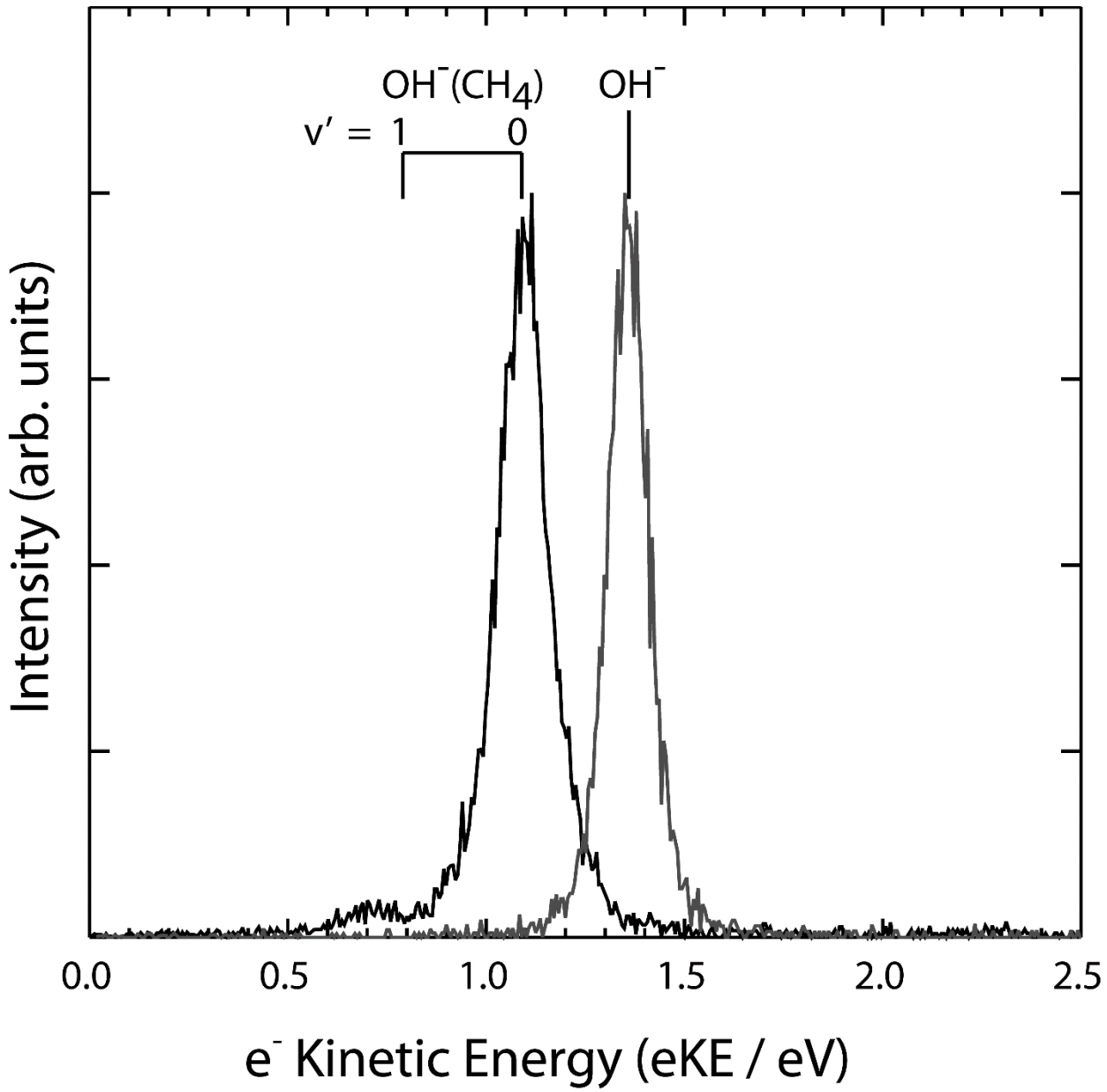

Figure 3.3. Overlaid photoelectron spectra of stable $OH^-(CH_4)$ (black) and OH^-(grey) with the main broad band centered on 1.09 and 1.36 eV, respectively. The shoulder peaking at 0.73 eV corresponds to v′=1 in the symmetric (ν_1) or asymmetric (ν_3) stretching modes of CH_4. This effectively also demonstrates the electron detector resolution $\Delta eKE/eKE \sim 4\%$.

Table 3.1. Dominant peak centers and their respective FWHMs for stable, dissociative, and total (stable + dissociative) photoelectrons.

Species	eKE centers (eV)	FWHM (eV)
$OH(CH_4)$	1.09[a]	0.16
	1.03[b]	0.21
	1.06[c]	-
$OH(CD_4)$	1.10[a]	0.19
	1.03[b]	0.21
	1.06[c]	-
$OD(CD_4)$	1.10[a]	0.20
	1.04[b]	0.20
	1.05[c]	-

[a]Value for stable photoelectrons

[b]Value for dissociative photoelectrons

[c]Value for total (stable + dissociative) photoelectrons

dissociative photoelectron spectra ($OH + CH_4 + e^-$) as shown in Figure 3.4. The top trace shows the stable spectrum previously seen, and the successive traces below are for the dissociative spectra integrated over a progressively wider range of the KER. Selecting for low KER gates of 0.00-0.02 eV, the main feature peaks at 1.095 eV and it shifts to 1.087 and 1.080 eV for KER gates of 0.00-0.03 and 0.00-0.04 eV, respectively. The main feature in the stable photoelectron spectrum peaks at 1.09 eV so the low-KER-gated photoelectron events are similar in energetics to the stable process. The striking similarities suggests contributions from the $OH(CH_4)$ complex predissociating to the $OH + CH_4$ channel along the 6.4 μs flight time from the interaction region to the QXDL.

3.4.2. Dissociative Photodetachment: $OH^-(CH_4) + h\nu \rightarrow OH + CH_4 + e^-$

The PPC spectrum corresponding to the dissociative $OH + CH_4 + e^-$ photoelectron spectrum reported is shown in Figure 3.5. This spectrum shows the correlation between eKE and the KER of the detected photofragments. Given the broadening observed in the experimental spectra, interpretation of the PPC spectrum is supported by the theoretical energetics reported in Figure 3.1. Using those energetics, two solid diagonal lines at 1.67 and 1.10 eV correspond to the maximum kinetic energies (KE_{max}) for the $H_2O + CH_3 + e^-$ and $OH + CH_4 + e^-$ channels, respectively. The dashed diagonal lines at 0.72 and 0.70 eV are the KE_{max} for one quantum of excitation in either the symmetric C-H stretch, ν_1, or asymmetric C-H stretch, ν_3, in the $OH + CH_4$ + e- reactant channel, respectively. The KE_{max} for excitation in the O-H fundamental stretch is not labeled but would only be slightly lower at 0.63 eV. At a photon energy of 3.20 eV there is enough energy to access both the reactant or exit channel products, so events that occur below the KE_{max} for the $H_2O + CH_3$ channel will also be discussed.

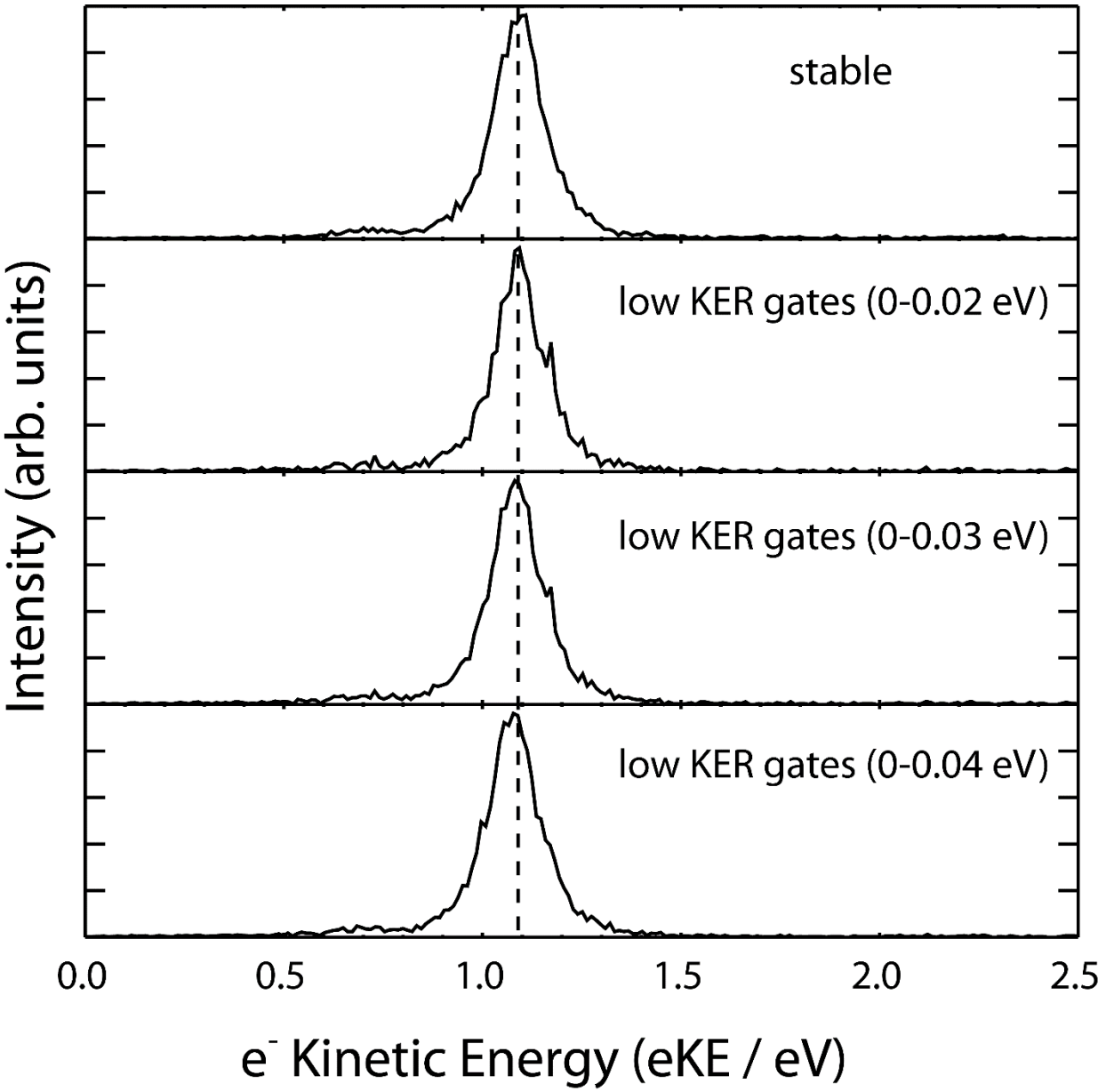

Figure 3.4. Kinetic energy release dependence of dissociative photoelectron spectra compared to photodetachment of stable $OH^-(CH_4)$. Peaks in the data are centered on 1.095, 1.087, and 1.080 eV for KER gates of 0.00-0.02, 0.03, and 0.04 eV, respectively. The photoelectron spectrum in the lowest KER range is indistinguishable from photoelectrons detected in coincidence with stable radicals.

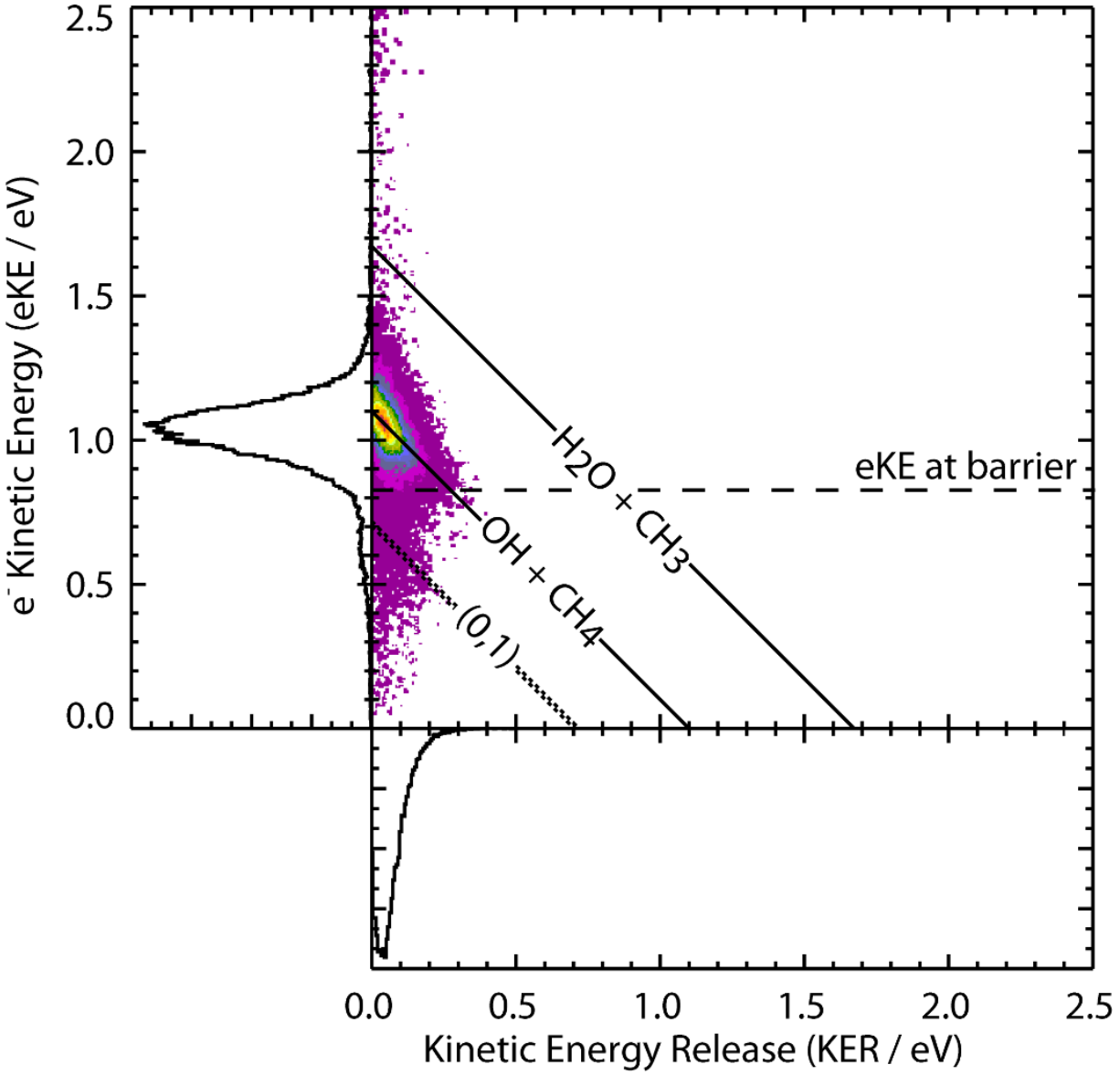

Figure 3.5. Photoelectron-photofragment coincidence plot for $OH^-(CH_4)$. Solid diagonal lines represent theoretical KE_{max} for OH + CH_4 and H_2O + CH_3 channels at 1.10 and 1.67 eV, respectively. Dashed diagonal lines represent excitation in the symmetric, ν_1, or asymmetric, ν_3, stretches (3077 and 3211 cm^{-1}, respectively).[20] No excitation in the OH fundamental stretch and 1 quanta of excitation in the CH_4 symmetric or asymmetric stretch denoted as (0, 1). The dashed horizontal line at eKE = 0.83 eV is the hydrogen abstraction barrier for the OH + $CH_4 \rightarrow H_2O$ + CH_3 reaction.

3.4.3. Dissociative photodetachment of $OH^-(CD_4)$ and $OD^-(CD_4)$ Isotopologs

To investigate isotope effects in this system, data was collected for the precursor anions $OH^-(CD_4)$ and $OD^-(CD_4)$. The total energy spectra (E_{TOT} = eKE + KER) for $OH^-(CH_4)$, $OH^-(CD_4)$ and $OD^-(CD_4)$ are shown in Figure 3.6. Both isotopes have similar features to the DPD of $OH^-(CH_4)$ consistent with formation of the entrance channel reactants, OH + CD_4 and/or OD + CD_4. The total energy spectrum for $OH^-(CD_4)$ has a lower energy peak centered at 0.16 eV with a FWHM of 0.21 eV which is contamination from DPD of $OH^-(D_2O)$.[50] The E_{TOT} for both isotopes have shoulders at ~0.25 eV lower in energy from the dominant feature because of the lower CD_4 symmetric and asymmetric stretching frequencies (0.26 and 0.28 eV, respectively).[51] The observance of similar DPD dynamics confirms that the C-H/C-D stretch excitation of CH_4/CD_4 is more significant than OH stretch excitation. The eKE peak centers for the isotopolog stable, dissociative, and total (stable + dissociative) photoelectron spectra are shown in Table 3.1. and show little evidence for zero-point energy shifts, suggesting that the anion and neutral isotope effects cancel each other out as confirmed by theory.

3.5. Discussion

PPC measurements, and the ability to separate stable versus dissociative photodetachment, provide a critical test of the energetics and dynamics of both bound and dissociative neutral states. Determination of the initial conditions, however, requires an anion potential energy surface in the vicinity of the anion bound state. Predictions of the subsequent neutral dynamics after photodetachment requires an approach to studying the evolution of the nascent neutral complex on the neutral potential energy surface. In the following, theoretical predictions will be used to analyze the energetics and energy partitioning observed in the photodetachment preparation and subsequent dissociation of the $OH(CH_4)$ complex.

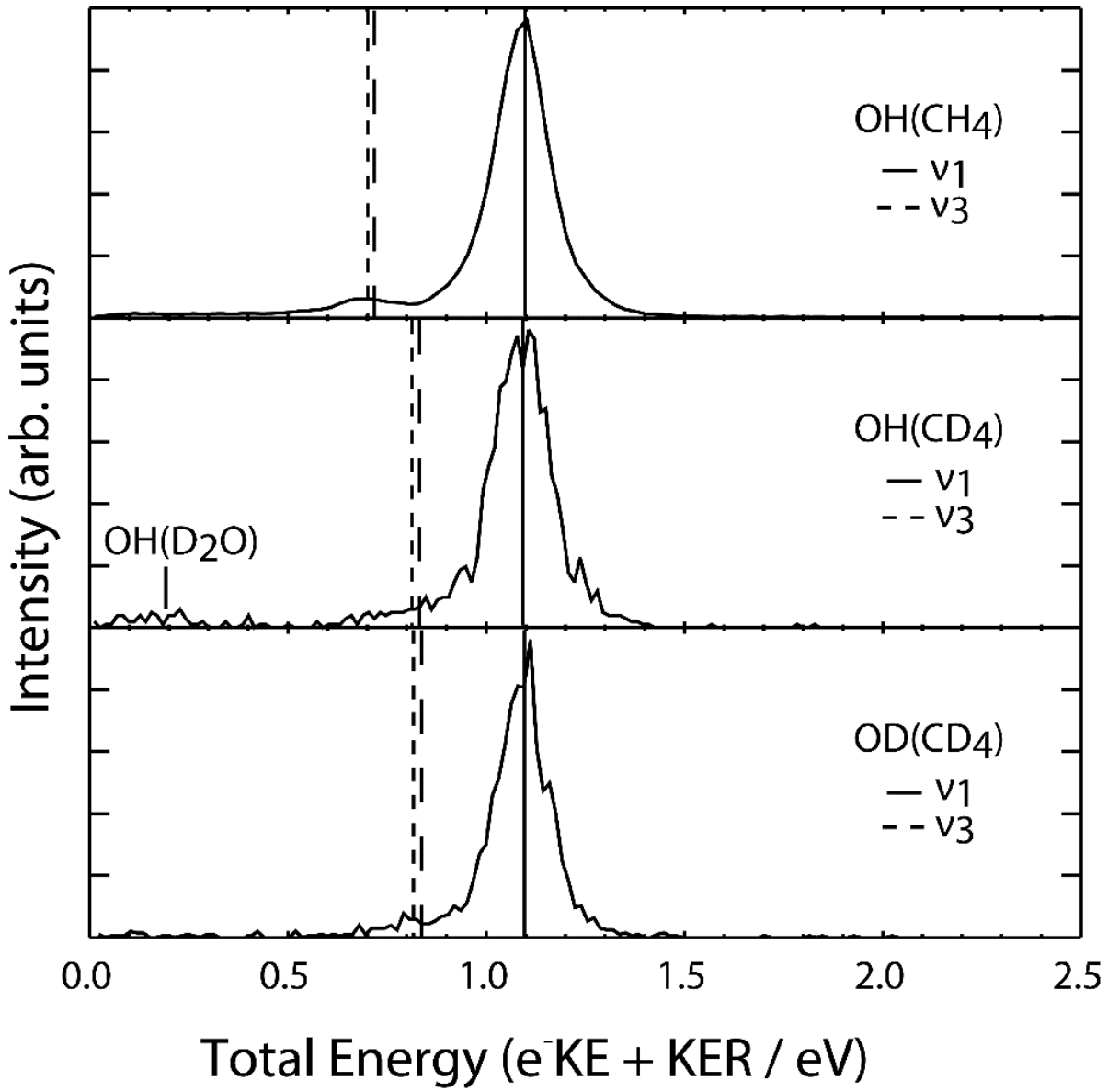

Figure 3.6. Total energy spectrum (eKE + KER) for $OH^-(CH_4)$, $OH^-(CD_4)$, and $OD^-(CD_4)$. Main feature centered on 1.099, 1.095, and 1.097 eV for $OH^-(CH_4)$, $OH^-(CD_4)$ and $OD^-(CD_4)$, respectively. Symmetric, ν_1, and asymmetric, ν_3, CH_4 stretches are labeled as well as the low energy isobar contamination in the $OH(CD_4)$ spectrum.

Using the potential energy surfaces and stationary points from the quantum chemical calculations discussed above, the energetics reported in Figure 3.1. were obtained. As seen in Figure 3.7., the geometry of the precursor anion resembles the transition state complex in the neutral reaction and has an O-H and H-C bond length of 1.980 Å and 1.102 Å, respectively. The shared hydrogen between the carbon and oxygen lies closer to the carbon as opposed to the more evenly shared hydrogen in the transition state complex. The geometry of the neutral transition state, reported previously,[15] has bond lengths of 1.321 and 1.206 Å, for O-H and H-C, respectively. The photoelectron spectrum for $OH(CH_4)$, shown in Figure 3.3., resembles the spectral fingerprint of OH shifted to lower eKE by the binding energy of the anion complex. With such a relatively low binding energy and the weak dipole of CH_4/CD_4, the electron density is mostly concentrated around the OH^- moiety. This is supported by the longer $HO\text{-}HCH_3$ bond (1.980 Å) and shorter $H\text{-}OHCH_3$ bond (0.964 Å) in the precursor anion compared to the transition state of the neutral surface. The precursor anion geometry is consistent with the stable species accessed by photodetachment lying in the entrance channel of the $OH + CH_4 \rightarrow H_2O + CH_3$ reaction pathway. In particular, the optimized anion equilibrium geometry, also shown in Figure 3.1., has a ZPE corrected energy of -2.072 eV relative to the neutral $OH + CH_4$ reactant asymptote and theoretical adiabatic electron affinity (AEA) = 2.05 and 1.41 eV from the anion to the stable entrance and exit channel van der Waals complexes, respectively. Therefore, the stable product formed upon photodetachment must lie in the entrance channel side of the neutral PES as there are no features at higher eKEs around 1.80 eV. An experimental vertical detachment energy (VDE) of 2.14 eV is obtained compared to the theoretical prediction of 2.18 eV, thus confirming good Franck-Condon overlap with the entrance channel.

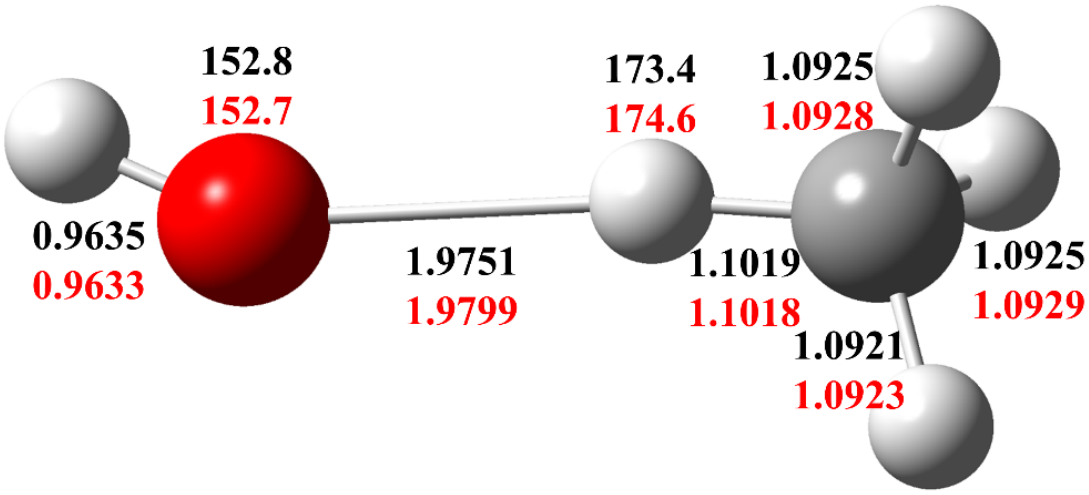

3775, 3093, 3089, 3056, 2897, 1575, 1573, 1374, 1374, 1291, 224, 218, 189, 101, 55
3772, 3099, 3095, 3057, 2902, 1574, 1572, 1378, 1376, 1283, 235, 233, 188, 123, 64

Figure 3.7. The geometries (distances in angstroms and angles in degrees) and harmonic frequencies (cm^{-1}) of the optimized $OH^-(CH_4)$ anion. The first entry is obtained on the PIP-NN anion PES, and the second is determined at the level of CCSD(T)-F12a/AVTZ.

The entrance channel van der Waals complex is 0.05 eV lower in energy than the entrance channel fragments ($OH + CH_4$) and has been discussed in the literature previously.[20] The geometry of this entrance channel complex is known to have the hydrogen of the OH group oriented towards the tetrahedral face of the methane unit as shown in Figure 3.1. The geometry of the entrance channel van der Waals complex differs greatly from the precursor anion where the hydrogen from the methane unit is oriented towards the oxygen of the OH unit. The anion would require significant rearrangement upon photodetachment to form the stable van der Waals complex, so it is expected to mostly dissociate.

Photodetachment of $OH^-(CH_4)$ at 3.20 eV yields two channels, (1) $OH(CH_4) + e^-$ and (2) $OH + CH_4 + e^-$. Channel (1) makes up ~26 % of total events (stable + dissociative) and is weakly bound (ground state binding energy of 0.026 eV previously determined from electronic spectroscopy[19] and 0.024 eV from theory with ZPE correction included). Upon photodetachment, some fraction of stable complexes are thought to be metastable and enveloped in the low kinetic energy release of the dissociating neutral fragments. This would result in slow dissociation over the 6.4 μs flight time, however, this process cannot be resolved in these experiments, and these events appear as stable complexes. Channel (2), DPD, is the dominant channel, yielding the entrance channel reactants with a minor channel corresponding to one quantum of excitation in the C-H stretching modes of the CH_4 reactant. This occurs because the interaction of OH^- with CH_4 distorts the monomers upon formation of the anion complex leading to excitation in the symmetric and asymmetric CH_4 stretching modes. The DPD dynamics of $OH^-(CD_4)$ and $OD^-(CD_4)$ are also consistent with excitation in the CD_4 ν_1 and ν_3 modes. The E_{TOT} spectra for $OH^-(CD_4)$ and $OD^-(CD_4)$ in Figure 3.6., show poorly resolved shoulders at ~0.8 eV (only ~0.25 eV from the main

feature). This is consistent with excitation of the C-D stretch in the products given the decrease in CD_4 stretching frequency compared to CH_4.

While the entrance reactant channel is the dominant channel accessed in the DPD of $OH^-(CH_4)$, the PPC spectrum shown in Figure 3.5. shows events occurring beyond the KE_{max} for $OH + CH_4$. At a photon energy of 3.20 eV, both the entrance and exit channels are energetically accessible. Photodetachment of the precursor anion, however, probes the weakly repulsive region in the entrance channel near the transition state. It is possible that upon photodetachment, the resultant neutral complex forms products via tunneling through the H-abstraction barrier. The barrier to dissociation into $H_2O + CH_3$ products lies at eKE = 0.83 eV, as shown by the dashed horizontal line in Figure 3.5. Events that occur below the H-abstraction barrier to the exit channel at higher eKE above the KE_{max} for $OH + CH_4$ might suggest tunneling as a pathway in the formation of the those products. PPC measurements on $OH(CD_4)$ and $OD(CD_4)$ yield similar dynamics, with the entrance channel reactants as the dominant channel and some excitation in the CH_4/CD_4 symmetric and asymmetric stretches. Although there appears to be fewer events beyond the KE_{max} for the $OD + CD_4$ channel (shown in Figure 3.8.), as would be expected for reduced tunneling in the deuterated complex, it is not substantial evidence for tunneling as a pathway to the exit channel ($H_2O + CH_3$) products given the inherent experimental resolution. Contributions beyond the entrance channel KE_{max} in the DPD of $OH^-(CH_4)$ may occur because of internal excitation in the precursor anions or isobaric contributions from HOO^-. Theoretical predictions elucidate the main processes involved in the reaction dynamics of $OH(CH_4)$.

QCT calculations on the neutral potential energy surface, with initial conditions determined by a Franck-Condon projection from the anion ground state were carried out as discussed in the theoretical section. Most of the 4000 trajectories on the neutral potential energy surface yielded

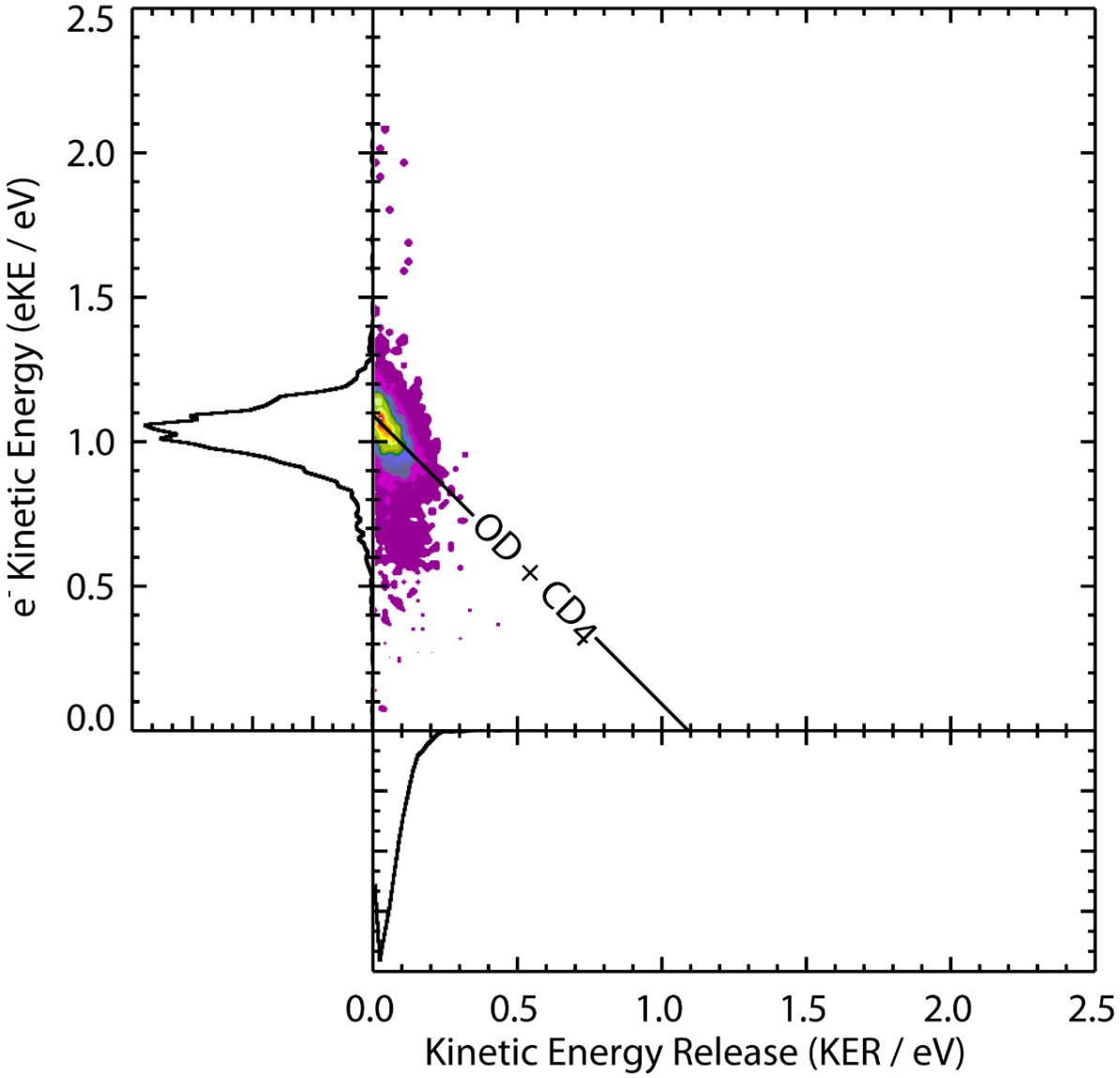

Figure 3.8. Photoelectron-photofragment coincidence plot for $OD^-(CD_4)$. The KE_{max} for OD + CD_4 channel is labeled with a theoretical isotope shift of -0.0080 eV relative to the $OH^-(CH_4)$ KE_{max} for OH + CH_4.

slowly recoiling OH + CH_4 fragments and only two were found in the H_2O + CH_3 channel. The fraction of the product channel might be underestimated because the QCT method does not account for tunneling. Among the rest of the trajectories, 10.4% were found to have energies below the ZPE of the OH + CH_4 channel, which correspond to the formation of the entrance channel van der Waals bound states. This is significantly smaller than the experimental value of 26%, but as discussed above, the experimental fraction contains populations of both bound and predissociative van der Waals complexes. In addition, false coincidences because of the low KER among dissociating fragments may be contributing to the registered stable events, thus increasing the percentage of stable channel contributions. These theoretical results are consistent with the experimental observations.

The kinetic energy partitioning can be examined in light of the QCT predictions of the dynamics for the neutral complexes produced by photodetachment. The KER distribution for the photofragments shown along the *x*-axis in Figure 3.5. displays a single narrow band that peaks at 0.04 eV and extends to ~0.3 eV. The repulsive energy in the neutral complex drives the energetics of this system. The low KER distribution is suggestive of minimal repulsion between OH and CH_4 on the neutral PES. The trajectory calculations indicate that the translational energy distribution between the OH and CH_4 fragments also peaks at 0.04 eV. The calculated KER is compared with the experimental results in Figure 3.9. While the peak positions of the two agree with each other, the experimental distribution is significantly broader. The small KER is due to the fact that most of the initial positions are in the entrance channel of the OH + CH_4 reaction. Specifically, the distance between the OH and CH_4 centers of mass is 3.13 Å in the anion, which is significantly larger than that of the transition state (2.47 Å). The neutral PES at the anion equilibrium geometry

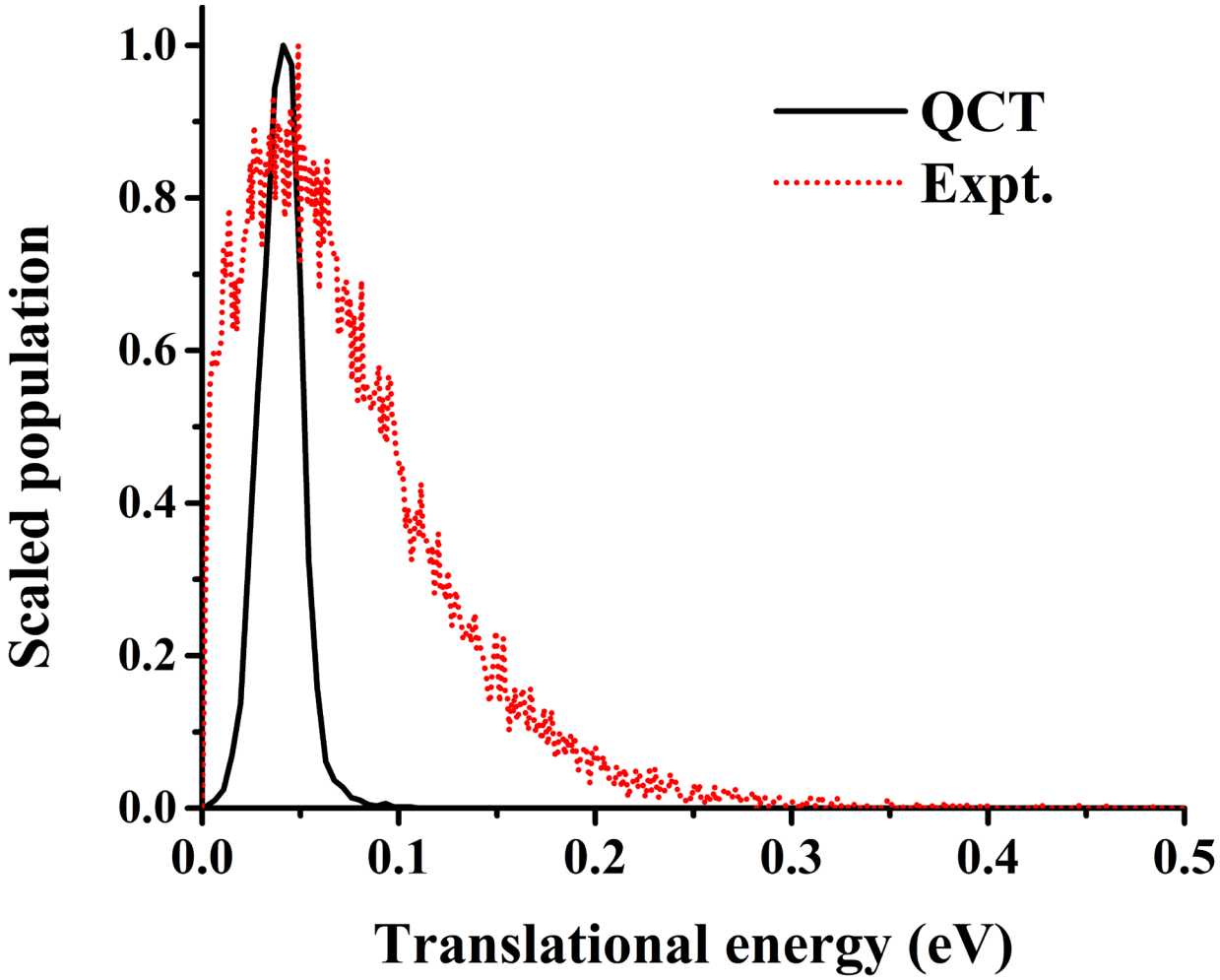

Figure 3.9. Comparison of the measured and calculated KER distribution in the OH + CH_4 channel.

is only 0.0826 eV above the reactant asymptote. Thus, the initial wave packet placed on the neutral PES by photodetachment of the anion is subjected to weak repulsion, leading to low KER.

The QCT calculations also found that the OH fragment in the OH + CH_4 channel is internally cold, with very small rotational and vibrational energies (see Figure 3.10.). This is reasonable as the O-H distance in the anion (0.964 Å) is very close to that of the free OH (0.971 Å). In addition, the anisotropy for the PES in the entrance channel is also quite weak. This agrees with the experimental results and further rules out possible OH vibrational excitation. In Figure 3.11., the calculated vibrational state distributions of all four modes of CH_4 are displayed. The figure shows that the CH_4 fragment is predominantly formed in its ground vibrational state. Some population is also found in the first excited states. Particularly noticeable is the excitation in the two excited C-H stretching vibrations. The averaged C-H bond length in the anion complex (1.095 Å) is almost identical to that in the free CH_4 (1.090 Å). The excitation is presumably from the slightly distorted CH_4 structure in the anion complex, as mentioned previously. Finally, the CH_4 rotational energy is also low (the average rotational energy is 0.017 eV), comparable to OH (0.026 eV). This picture is entirely consistent with the PPC spectrum shown in Figure 3.5.

3.6. Summary

Photoelectron-photofragment coincidence measurements were carried out on the $OH^-(CH_4)/OH^-(CD_4)/OD^-(CD_4)$ clusters. The main channel observed is dissociative photodetachment yielding the ground state photofragments, OH + CH_4 + e^- with a low KER ~0.04 eV. Excitation in the C-H symmetric and asymmetric stretch of CH_4 was also observed as a minor channel as shown by isotopic substitution and confirmed by QCT calculations. A significant fraction (~26%) of the products are found to be stable OH-CH_4 complexes. Given the low KER, this stable fraction is likely an upper limit as dissociation can occur over the 6.4 μs flight time

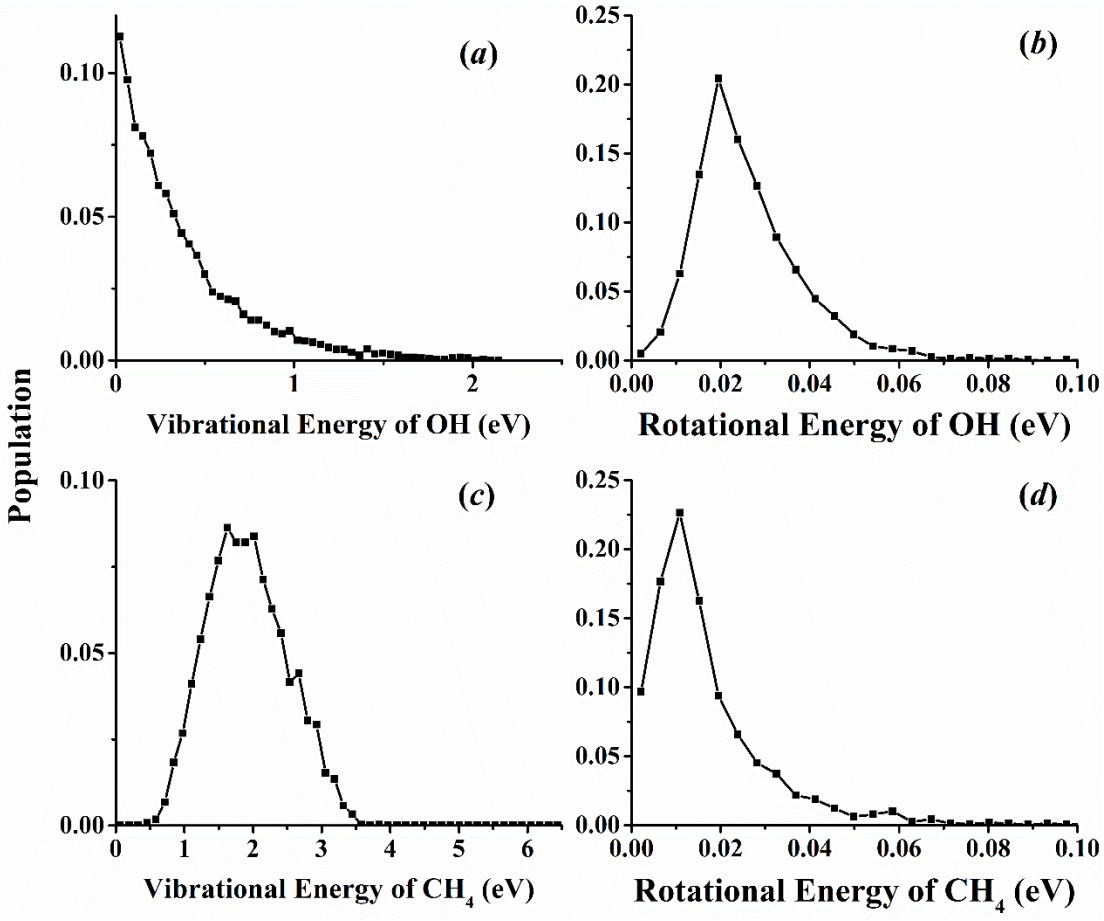

Figure 3.10. The vibrational and rotational energy populations of the OH and CH_4 species.

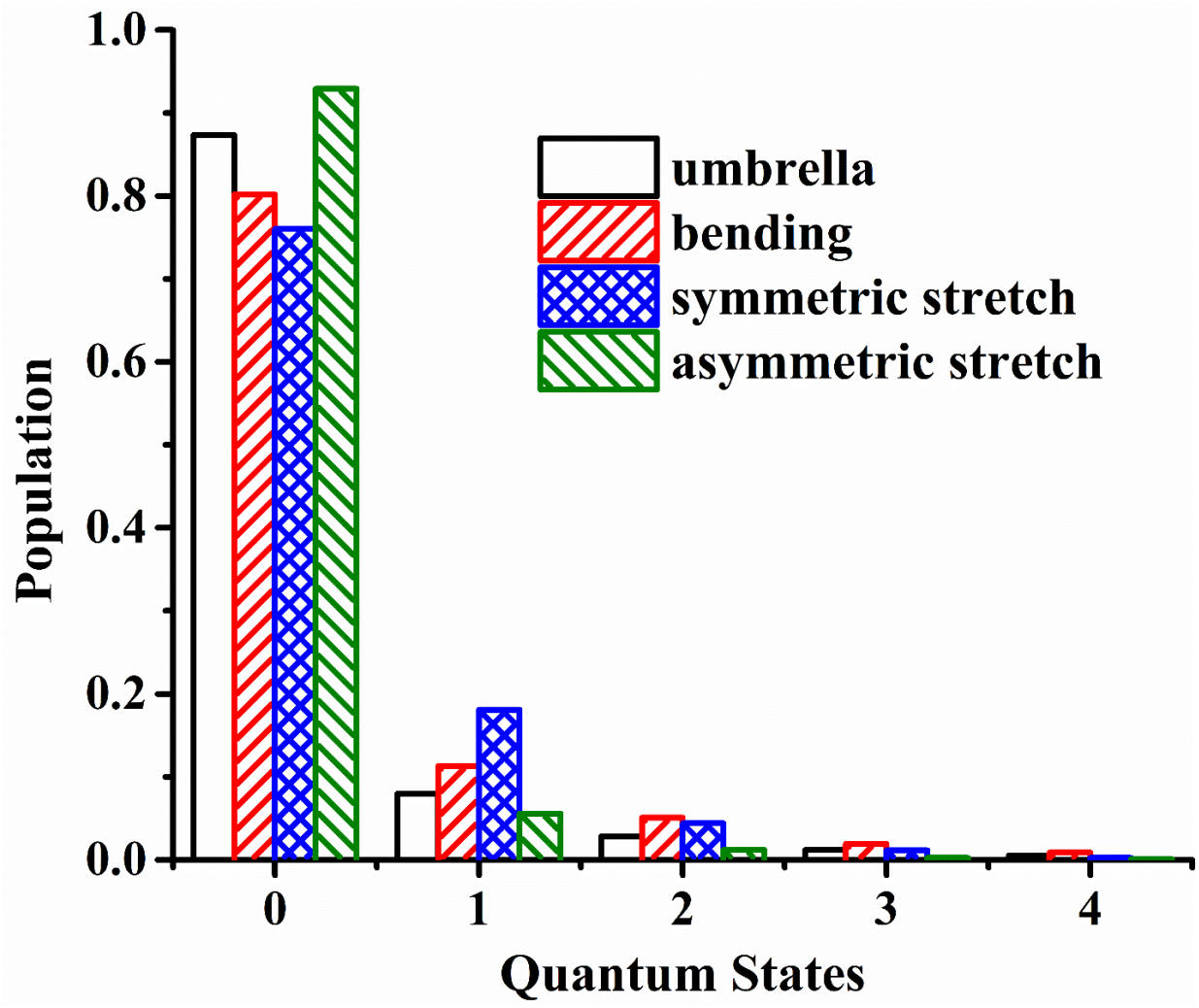

Figure 3.11. Calculated vibrational state distributions for the four vibrational modes of the CH_4 fragment.

from the interaction region to the neutral particle detector. A smaller fraction of the $OH(CH_4)$ complexes may also be tunneling through the H-abstraction barrier yielding the exit channel products $H_2O + CH_3$, however, this is not resolved in these experiments. These experimental observations have been qualitatively reproduced by QCT calculations sampled on the neutral state PES from a phase space Wigner distribution determined by the newly constructed anion PES. The combined experimental and theoretical results validates the accuracy of the PESs and helps shed new insight on the dynamics of this important reaction.

Associated Content

Supporting Information: Provides additional figures of the theoretical and experimental results.

Acknowledgements

This material is based on work supported by the U.S. Department of Energy, Office of Science, Office of Basic Energy Sciences under Award Number DE-FG03-98ER14879 to R.E.C. J.L. thanks the support from National Natural Science Foundation of China (Contract No. 21573027) and the Alexander von Humboldt Foundation (Humboldt Fellowship for Experienced Researchers for JL). H.G. acknowledges the generous support of the U.S. Air Force Office of Scientific Research (FA9550-15-1-0305).

Chapter 3 is a reprint of the material as it appeared in Benitez, Y.; Lu, D.; Lunny, K. G.; Li, J.; Guo, H.; Continetti, R. E., Photoelectron-Photofragment Coincidence Studies on the Dissociation Dynamics of the OH-CH_4 Complex, *J. Phys. Chem. A* **2019**, 123(23), 4825-4833.

Some of the supplemental figures were incorporated into the text. The dissertation author is the primary author. The corresponding authors are the dissertation advisor, R. E. Continetti, and Jun Li.

3.7. References

1. S. Monks, P. Gas-Phase Radical Chemistry in the Troposphere. *Chem. Soc. Rev.* **2005**, *34* (5), 376–395.

2. Vaghjiani, G. L.; Ravishankara, A. R. New Measurement of the Rate Coefficient for the Reaction of OH with Methane. *Nature* **1991**, *350* (6317), 406–409.

3. Hein, R.; Crutzen, P. J.; Heimann, M. An Inverse Modeling Approach to Investigate the Global Atmospheric Methane Cycle. *Glob. Biogeochem. Cycles* **1997**, *11* (1), 43–76.

4. Glassman, I.; Yetter, R. A.; Glumac, N. G. *Combustion*; Academic Press, 2014.

5. Sharkey, P.; Smith, I. W. M. Kinetics of Elementary Reactions at Low Temperatures: Rate Constants for the Reactions of OH with HCl ($298 \geq T/K \geq 138$), CH_4($298 \geq T/K \geq 178$) and C_2H_6($298 \geq T/K \geq 138$). *J. Chem. Soc. Faraday Trans.* **1993**, *89* (4), 631–637.

6. Srinivasan, N. K.; Su, M.-C.; Sutherland, J. W.; Michael, J. V. Reflected Shock Tube Studies of High-Temperature Rate Constants for $OH + CH_4 \rightarrow CH_3 + H_2O$ and $CH_3 + NO_2 \rightarrow CH_3O + NO$. *J. Phys. Chem. A* **2005**, *109* (9), 1857–1863.

7. Baulch, D. L.; Bowman, C. T.; Cobos, C. J.; Cox, R. A.; Just, T.; Kerr, J. A.; Pilling, M. J.; Stocker, D.; Troe, J.; Tsang, W.; et al. Evaluated Kinetic Data for Combustion Modeling: Supplement II. *J. Phys. Chem. Ref. Data* **2005**, *34* (3), 757–1397.

8. Truong, T. N.; Truhlar, D. G. Ab Initio Transition State Theory Calculations of the Reaction Rate for $OH+CH_4 \rightarrow H_2O+CH_3$. *J. Chem. Phys.* **1990**, *93* (3), 1761–1769.

9. Dobbs, K. D.; Dixon, D. A.; Komornicki, A. Ab Initio Prediction of the Barrier Height for Abstraction of H from CH_4 by OH. *J. Chem. Phys.* **1993**, *98* (11), 8852–8858.

10. Melissas, V. S.; Truhlar, D. G. Interpolated Variational Transition State Theory and Tunneling Calculations of the Rate Constant of the Reaction $OH+CH_4$ at 223–2400 K. *J. Chem. Phys.* **1993**, *99* (2), 1013–1027.

11. Espinosa-García, J.; Corchado, J. C. Potential Energy Surface for a Seven-Atom Reaction. Thermal Rate Constants and Kinetic Isotope Effects for CH_4+OH. *J. Chem. Phys.* **2000**, *112* (13), 5731–5739.

12. Ellingson, B. A.; Pu, J.; Lin, H.; Zhao, Y.; Truhlar, D. G. Multicoefficient Gaussian-3 Calculation of the Rate Constant for the OH + CH_4 Reaction and Its $^{12}C/^{13}C$ Kinetic Isotope Effect with Emphasis on the Effects of Coordinate System and Torsional Treatment. *J. Phys. Chem. A* **2007**, *111* (45), 11706–11717.

13. Wang, W.; Zhao, Y. Quantum Instanton Calculation of Rate Constant for CH_4 + OH → CH_3 + H_2O Reaction: Torsional Anharmonicity and Kinetic Isotope Effect. *J. Chem. Phys.* **2012**, *137* (21), 214306.

14. Allen, J. W.; Green, W. H.; Li, Y.; Guo, H.; Suleimanov, Y. V. Communication: Full Dimensional Quantum Rate Coefficients and Kinetic Isotope Effects from Ring Polymer Molecular Dynamics for a Seven-Atom Reaction OH + CH_4 → CH_3 + H_2O. *J. Chem. Phys.* **2013**, *138* (22), 221103.

15. Li, J.; Guo, H. Communication: An Accurate Full 15 Dimensional Permutationally Invariant Potential Energy Surface for the OH + CH_4 → H_2O + CH_3 Reaction. *J. Chem. Phys.* **2015**, *143* (22), 221103.

16. Suleimanov, Y. V.; Espinosa-Garcia, J. Recrossing and Tunneling in the Kinetics Study of the OH + CH_4 → H_2O + CH_3 Reaction. *J. Phys. Chem. B* **2016**, *120* (8), 1418–1428.

17. Espinosa-Garcia, J.; Corchado, J. C. Product Translational and Vibrational Distributions for the OH/OD + CH_4/CD_4 Reactions from Quasiclassical Trajectory Calculations. Comparison with Experiment. *J. Phys. Chem. B* **2016**, *120* (8), 1446–1453.

18. Li, J.; Guo, H. Thermal Rate Coefficients and Kinetic Isotope Effects for the Reaction OH + CH_4 → H_2O + CH_3 on an Ab Initio-Based Potential Energy Surface. *J. Phys. Chem. A* **2018**, *122* (10), 2645–2652.

19. Tsiouris, M.; Wheeler, M. D.; Lester, M. I. Stimulated Raman and Electronic Excitation of CH_4–OH Reactant Complexes. *Chem. Phys. Lett.* **1999**, *302* (1), 192–198.

20. Wheeler, M. D.; Tsiouris, M.; Lester, M. I.; Lendvay, G. OH Vibrational Activation and Decay Dynamics of CH_4–OH Entrance Channel Complexes. *J. Chem. Phys.* **2000**, *112* (15), 6590–6602.

21. Tsiouris, M.; Wheeler, M. D.; Lester, M. I. Activation of the CH Stretching Vibrations in CH_4–OH Entrance Channel Complexes: Spectroscopy and Dynamics. *J. Chem. Phys.* **2000**, *114* (1), 187–197.

22. Zhang, B.; Shiu, W.; Lin, J. J.; Liu, K. Mode Correlation of Product Pairs in the Reaction OH+CD_4→HOD+CD_3. *J. Chem. Phys.* **2005**, *122* (13), 131102.

23. Zhang, B.; Shiu, W.; Liu, K. Imaging the Reaction Dynamics of OH + CD_4. 2. Translational Energy Dependencies. *J. Phys. Chem. A* **2005**, *109* (40), 8983–8988.

24. Zhang, B.; Shiu, W.; Liu, K. Imaging the Reaction Dynamics of OH + CD_4. 3. Isotope Effects. *J. Phys. Chem. A* **2005**, *109* (40), 8989–8993.

25. Espinosa-Garcia, J.; Corchado, J. C. QCT Dynamics Study of the Reaction of Hydroxyl Radical and Methane Using a New Ab Initio Fitted Full-Dimensional Analytical Potential Energy Surface. *Theor. Chem. Acc.* **2015**, *134* (2), 6.

26. Espinosa-Garcia, J.; Rangel, C.; Corchado, J. C. Vibrational, Rotational and Translational Effects on the OH(v, j) + CH_4(v_1, v_2, v_3, v_4) Dynamics Reaction: A Quasi-Classical Trajectory Study. *Theor. Chem. Acc.* **2015**, *135* (1), 10.

27. Song, H.; Lee, S.-Y.; Yang, M.; Lu, Y. Six-Dimensional and Seven-Dimensional Quantum Dynamics Study of the OH + CH_4 → H_2O + CH_3 Reaction. *J. Chem. Phys.* **2013**, *139* (15), 154310.

28. Song, H.; Li, J.; Jiang, B.; Yang, M.; Lu, Y.; Guo, H. Effects of Reactant Rotation on the Dynamics of the OH + CH_4 → H_2O + CH_3 Reaction: A Six-Dimensional Study. *J. Chem. Phys.* **2014**, *140* (8), 084307.

29. Song, H.; Lu, Y.; Li, J.; Yang, M.; Guo, H. Mode Specificity in the OH + CHD_3 Reaction: Reduced-Dimensional Quantum and Quasi-Classical Studies on an Ab Initio Based Full-Dimensional Potential Energy Surface. *J. Chem. Phys.* **2016**, *144* (16), 164303.

30. Continetti, R. E. Coincidence Spectroscopy. *Annu. Rev. Phys. Chem.* **2001**, *52* (1), 165–192.

31. E. Continetti, R.; Guo, H. Dynamics of Transient Species via Anion Photodetachment. *Chem. Soc. Rev.* **2017**, *46* (24), 7650–7667.

32. Hanold, K. A.; Luong, A. K.; Clements, T. G.; Continetti, R. E. Photoelectron–Multiple-Photofragment Coincidence Spectrometer. *Rev. Sci. Instrum.* **1999**, *70* (5), 2268–2276.

33. Johnson, C. J.; Shen, B. B.; Poad, B. L. J.; Continetti, R. E. Photoelectron-Photofragment Coincidence Spectroscopy in a Cryogenically Cooled Linear Electrostatic Ion Beam Trap. *Rev. Sci. Instrum.* **2011**, *82* (10), 105105.

34. Shen, B. B.; Benitez, Y.; Lunny, K. G.; Continetti, R. E. Internal Energy Dependence of the Photodissociation Dynamics of O_3^- Using Cryogenic Photoelectron-Photofragment Coincidence Spectroscopy. *J. Chem. Phys.* **2017**, *147* (9), 094307.

35. Lu, Y.-J.; Lehman, J. H.; Lineberger, W. C. A Versatile, Pulsed Anion Source Utilizing Plasma-Entrainment: Characterization and Applications. *J. Chem. Phys.* **2015**, *142* (4), 044201.

36. Wiley, W. C.; McLaren, I. H. Time-of-Flight Mass Spectrometer with Improved Resolution. *Rev. Sci. Instrum.* **1955**, *26* (12), 1150–1157.

37. Bowen, M. S.; Continetti, R. E. Photodetachment Imaging Study of the Vinoxide Anion. *J. Phys. Chem. A* **2004**, *108* (39), 7827–7831.

38. Hanold, K. A.; Continetti, R. E. Photoelectron–Photofragment Coincidence Studies of the Dissociative Photodetachment of O_4^-. *Chem. Phys.* **1998**, *239* (1), 493–509.

39. Active Thermochemical Tables (ATcT) values based on ver. 1.22d of the Thermochemical Network (2018); available at ATcT.anl.gov.

40. Jiang, B.; Li, J.; Guo, H. Potential Energy Surfaces from High Fidelity Fitting of Ab Initio Points: The Permutation Invariant Polynomial - Neural Network Approach. *Int. Rev. Phys. Chem.* **2016**, *35* (3), 479–506.

41. Heller, E. J. Wigner Phase Space Method: Analysis for Semiclassical Applications. *J. Chem. Phys.* **1976**, *65* (4), 1289–1298.

42. Brown, R. C.; Heller, E. J. Classical Trajectory Approach to Photodissociation: The Wigner Method. *J. Chem. Phys.* **1981**, *75* (1), 186–188.

43. Arbelo-González, W.; Bonnet, L.; García-Vela, A. Semiclassical Wigner Theory of Photodissociation in Three Dimensions: Shedding Light on Its Basis. *J. Chem. Phys.* **2015**, *142* (13), 134111.

44. Sun, L.; Hase, W. L. Comparisons of Classical and Wigner Sampling of Transition State Energy Levels for Quasiclassical Trajectory Chemical Dynamics Simulations. *J. Chem. Phys.* **2010**, *133* (4), 044313.

45. Hu, X.; Hase, W. L.; Pirraglia, T. Vectorization of the General Monte Carlo Classical Trajectory Program VENUS. *J. Comput. Chem.* **1991**, *12* (8), 1014–1024.

46. Czakó, G.; Bowman, J. M. Quasiclassical Trajectory Calculations of Correlated Product Distributions for the F+CHD_3(v_1=0,1) Reactions Using an Ab Initio Potential Energy Surface. *J. Chem. Phys.* **2009**, *131* (24), 244302.

47. C. Corchado, J.; Espinosa-Garcia, J. Product Vibrational Distributions in Polyatomic Species Based on Quasiclassical Trajectory Calculations. *Phys. Chem. Chem. Phys.* **2009**, *11* (43), 10157–10164.

48. Xie, C.; Jiang, B.; Yang, M.; Guo, H. State-to-State Mode Specificity in F + CHD_3 → HF/DF + CD_3/CHD_2 Reaction. *J. Phys. Chem. A* **2016**, *120* (33), 6521–6528.

49. Schulz, P. A.; Mead, R. D.; Jones, P. L.; Lineberger, W. C. OH^- and OD^- Threshold Photodetachment. *J. Chem. Phys.* **1982**, *77* (3), 1153–1165.

50. Deyerl, H.-J.; Luong, A. K.; G. Clements, T.; E. Continetti, R. Transition State Dynamics of the OH+H_2O Hydrogen Exchange Reaction Studied by Dissociative Photodetachment of $H_3O_2^-$. *Faraday Discuss.* **2000**, *115* (0), 147–160.

51. Fox, K. Vibration-Rotation Interactions in Infrared Active Overtone Levels of Spherical Top Molecules; $2\nu_3$ and $2\nu_4$ of CH_4, $2\nu_3$ of CD_4. *J. Mol. Spectrosc.* **1962**, *9*, 381–420.

Chapter 4: Dissociation Dynamics of the $OH^-(C_2H_4)$ Anion Complex

4.1. Introduction

Radical-molecule reactions play an important role in understanding both atmospheric and combustion chemistry. In particular, the reactions involving the hydroxyl radical with alkenes are significant in atmospheric and combustion processes. Understanding this class of elementary reactions can help elucidate fundamental aspects of the addition of the OH radical to unsaturated carbon-carbon double bonds in the alkenes. The hydroxyl radical is also one of the dominant species involved in the atmospheric oxidation of alkenes leading to formation of a radical adduct that can then be further oxidized.[1] The decomposition of this adduct is important in hydrocarbon flames since it is the dominant source of ethanol.[2-4] As a result, numerous kinetic-based[5-11] and dynamics[12-18] studies have been performed on this system.

The OH + C_2H_4 reaction can proceed through hydrogen abstraction leading to H_2O + $CHCH_2$ products, or it can form a stable adduct via electrophilic addition of the hydroxyl radical to ethylene. Kinetic studies have found that at high temperatures, the reaction is dominated first by decomposition to the reactant channel, OH + C_2H_4, and then by H-abstraction and/or isomerization, however, at lower temperatures, formation of the radical adduct is favored.[5, 19-21] Experiments have shown that the consumption of OH radicals leading to formation of an addition complex, CH_2CH_2OH, exhibits negative activation energies, a property representative of hydroxide and alkene reactions.[22] This negative activation energy is consistent with the involvement of a weakly bound van der Waals (vdW) complex in the entrance channel, found to have C_{2v} geometry with the hydrogen of the hydroxyl group perpendicular to the C_2H_4 plane and oriented towards the π bond.[23] The inclusion of this complex in theoretical treatments of the

kinetics of the OH + C_2H_4 system has been shown to accurately model the addition reaction and agrees well with experiment.[21, 24]

To explain discrepancies in data from measurements obtained at low and high temperatures, a theoretical model was developed by Senosiain and co-workers[24] based on high level *ab initio* calculations of isomers and low energy saddle points on the C_2H_5O potential energy surface. A multichannel-master equation model using derived energies from their calculated potential energy surface (PES) and from the model proposed by Greenwald and co-workers[21] was used to compute rate coefficients over a large range of temperatures and pressures. Their calculations confirm the importance of H-abstraction at high temperatures (>800 K) and provide high-level calculations for all low-energy pathways of the title reaction as shown in Figure 4.1.

The CH_2CH_2OH adduct, also known as 2-hydroxyethyl radical, has been studied extensively due to its importance in combustion and atmospheric chemistry. This adduct has been formed photolytically from haloethanols,[12, 13, 15, 16, 18, 25] and dissociation of this adduct leads predominantly to the OH + C_2H_4 channel. The adduct has also been shown to contribute to a minor H_2O + $CHCH_2$ channel via a frustrated dissociation of CH_2CH_2OH leading to the OH + C_2H_4 channel.[17, 18] In this case, the weakly bound entrance channel vdW complex is thought to play a key role in forming the water and vinyl product channel, not through a direct H-abstraction mechanism but during a trajectory to OH + C_2H_4 where the weakly bound OH in the vdW complex can abstract a hydrogen via a roaming mechanism.[17] The dissociation of the adduct has also been shown to contribute to H + CH_2CHOH products.[16, 23, 24, 26]

The energy partitioning relevant to this system has been described previously through impulsive models.[13, 15, 18] Ratliff et al.[15] generated the 2-hydroxyethyl radical intermediate,

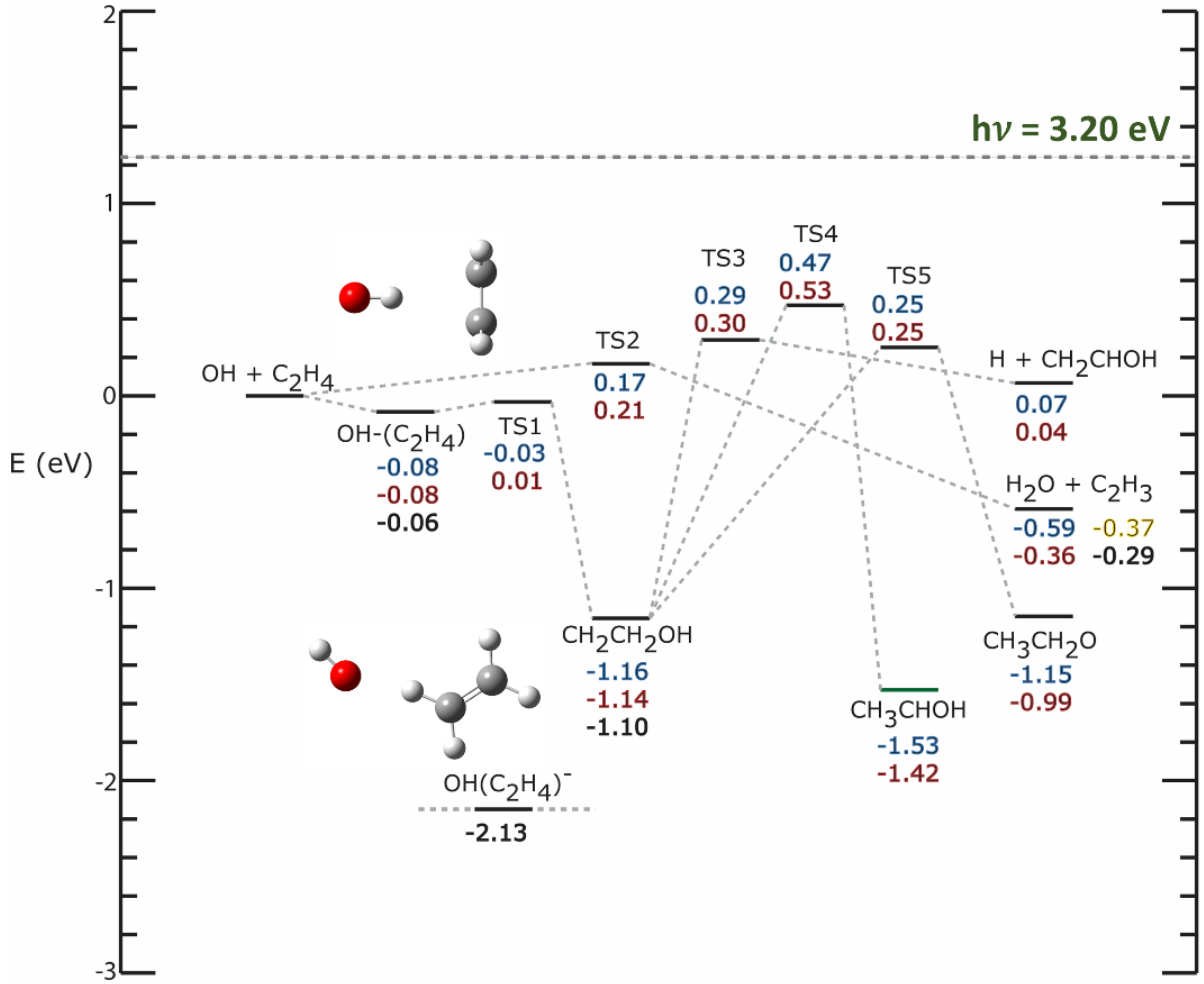

Figure 4.1. Relevant reaction scheme for the C_2H_5O system along with energetics for the entrance channel, OH + C_2H_4, exit channel, H_2O + $CHCH_2$, van der Waals complexes, isomers, transition states, and anion complex, OH-(C_2H_4). All energies are in eV relative to the reactant asymptote OH + C_2H_4 with zero-point energy corrections. The energetics in blue and red correspond to previously reported values at the B3LYP/cc-pVDZ[17] and RQCIT//QCI[24] level, respectively. The energetics in black are computed at the CCSD(T)/aug-cc-pVTZ level using MP2/aug-cc-pVDZ optimized geometries. Geometries for the neutral van der Waals and minimum energy configuration for the anion are shown.

CH_2CH_2OH, by photolysis of bromoethanol, $BrCH_2CH_2OH$, and used an impulsive model to derive the rotational energy distribution of the nascent CH_2CH_2OH radicals. This model allowed estimation of the vibrational energy distributed to the CH_2CH_2OH radicals leading to predictions of the product branching channels by averaging over the microcanonical rate constants. The impulsive model took into account the measured translational energy distribution as well as a theoretically predicted range of impact parameters accessed by the photolytic precursor zero-point and thermal vibrational motion. Even though the CH_2CH_2OH radicals had internal energies above the dissociation barrier for the $OH + C_2H_4$ channel, some of the radicals were stabilized because the energy was partitioned to rotation rather than vibration. The model gave a good fit to the measured translational energy distribution for the CH_2CH_2OH radicals. A more simplified version of this model is used in this study to predict the rotational energy partitioning in the dissociation photodetachment (DPD) dynamics of $OH^-(C_2H_4)$.

In the present work, the dynamics of the $OH + C_2H_4$ reaction on the neutral PES are studied using photoelectron-photofragment coincidence (PPC) measurements, complementing previous photodissociation studies of the neutral reaction.[12, 15, 18] These experiments use photodetachment of a precursor anion, $OH^-(C_2H_4)$, at a photon energy of $E_{h\nu} = 3.20$ eV to observe the resulting neutral dynamics. The photodetachment scheme for the current system, shown in Figure 4.1., details the relevant reaction pathway for the $OH + C_2H_4$ system. The dynamics initiated near the anion equilibrium geometry have the best Franck-Condon overlap with the entrance channel with a similar geometry to the transition state[17, 24] (TS2) leading to the product channel $H_2O + CHCH_2$. Many studies have focused on the CH_2CH_2OH intermediate however, that portion of the neutral surface is not accessed in this study and, instead, evidence for formation of a weakly bound vdW complex as well as the entrance channel reactants are observed. We report photoelectron spectra

for the DPD channel $OH^-(C_2H_4) + h\nu \rightarrow OH + C_2H_4 + e^-$, as well as the formation of stable OH-C_2H_4 complexes in the $OH^-(C_2H_4) + h\nu \rightarrow OH(C_2H_4) + e^-$ photodetachment pathway. In addition, some evidence is observed for accessing the product channel $H_2O + C_2H_3 + e^-$. The overall partitioning of kinetic energy in the primary DPD process is examined using the proposed minimum energy configuration of the precursor anion (Figure 4.2.) to estimate the rotational energy imparted to the C_2H_4 photofragments via an impulsive model.

4.2. Experiment

These experiments were carried out using the cryo-PPC spectrometer described previously.[27] This apparatus uses a radio frequency cryogenic octopole accumulation trap (COAT) for the preparation of internally cold precursor anions prior to injection into the electrostatic ion beam trap (EIBT) where the coincidence experiments are performed.[28] To summarize, anions were synthesized using a dual pulsed valve entrainment source at a 10 Hz repetition rate. The dual pulsed valve setup allows for a rational approach in forming cluster anions[29] and was used in a previous study to form $OH^-(CH_4)$ anions.[30] A low gas density flow of 5:45:50 N_2O, Ar, CH_4, respectively, passed through a coaxial pulsed discharge generating a plasma that intersected a pulsed supersonic beam of ~10% C_2H_4 in Ar, entraining hydroxide anions and allowing subsequent interactions with C_2H_4. A 1 keV electron beam counterpropagating the main expansion was used to stabilize the discharge.

The anions were perpendicularly extracted using a Wiley-McLaren time-of-flight (TOF) mass spectrometer,[31] focused, injected and stored in COAT for 40 ms, accelerated to 7 keV, and re-referenced to ground using a fast potential switch. The anion packets were separated by TOF, focused, and steered into a cryogenically cooled EIBT where the mass-selected ions were trapped and crossed with a 1037 Hz, 388 nm ($E_{h\nu}$ = 3.20 eV) laser pulse from a Ti:Sapphire regenerative

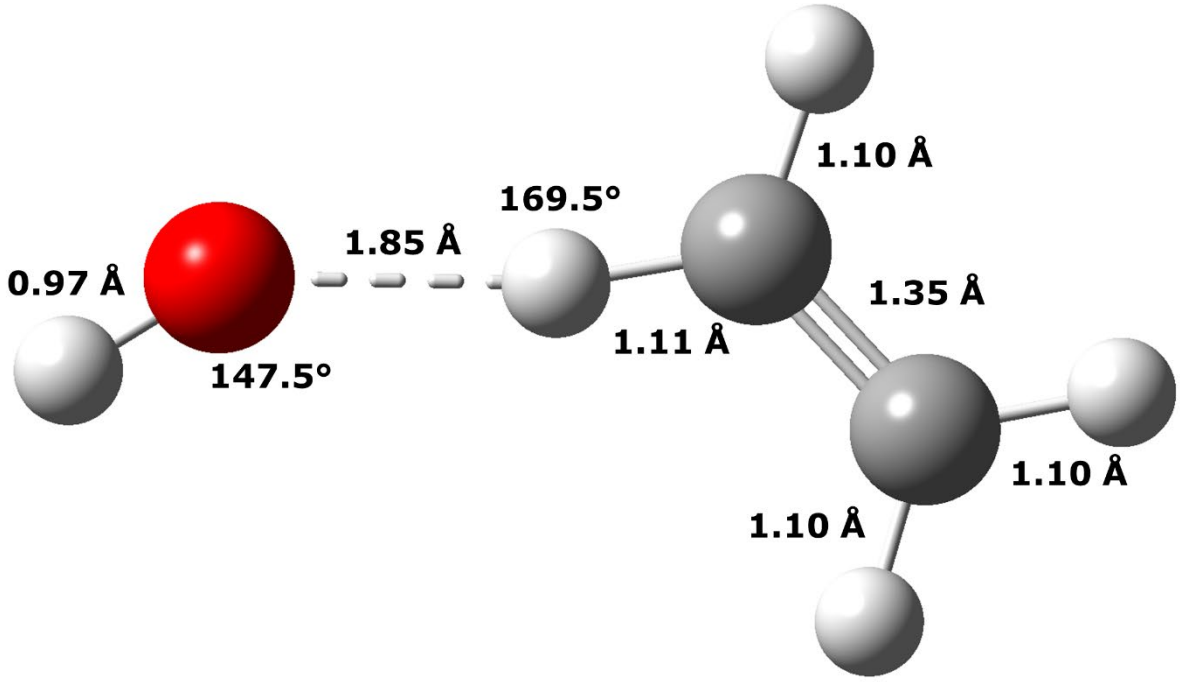

Figure 4.2. Minimum energy configuration determined at the MP2/aug-cc-pVDZ level for the $OH^{-}(C_2H_4)$ anion.

amplifier (Clark MXR CPA-2000; 1.1 ps pulse width) over the course of the 100 ms trapping period per experimental cycle. The resultant electron and neutral fragment(s) were collected.

Photoelectrons were perpendicularly extracted from the laser-ion interaction region and mapped onto a time- and position-sensitive detector for determination of the center-of-mass electron kinetic energy (eKE) for each event. Equatorially slicing the photoelectron spectra by selecting electrons with minimal z-velocities perpendicular to the face of the detector gives the best resolution. Correcting for relative intensities in the photoelectron spectra was achieved by dividing the sliced photoelectron spectra by the energy-dependent acceptance function of the z-velocity slice.[32] Calibration spectra of O^- and OH^- showed ΔeKE/eKE resolution of 5.6 % full-width-half-max (FWHM) at eKE = 1.74 and 1.36 eV, respectively.

Upon photodetachment, the resultant neutrals, no longer constrained by the electrostatic fields, recoil out of the EIBT, impinging on a multiparticle time and position sensitive detector ~1.3 m downstream allowing the product mass ratio and kinetic energy release (KER) for dissociation events to be determined. This quad-crossed-delay-line (QXDL) detector was calibrated by collecting a dissociative photodetachment (DPD) spectrum of O_4^- showing a ΔKER/KER resolution of ~10% FWHM at 0.4 eV.[33] Stable events detected by the QXDL arrived in a spot ~4 mm in diameter. Dissociative events, on the other hand, are distributed across the face of the QXDL as determined by the KER and the fragment mass ratio. In the present study, the dissociative events have a very low KER complicating the distinguishability between low KER events and stable events. In addition, the spread of the distribution of the centers of mass leads to a limited photofragment mass resolution, so channels with fragment masses differing by only 1 amu are unresolvable. Therefore, the OH + C_2H_4 and H_2O + $CHCH_2$ fragment masses cannot be resolved experimentally.

4.3. Results

In this section, photoelectron spectra for stable and dissociative complexes formed upon photodetachment of $OH^-(C_2H_4)$ will be presented followed by PPC spectra that reveal the partitioning of kinetic energy between photoelectron and photofragments.

4.3.1. Photodetachment of $OH^-(C_2H_4) + h\nu \rightarrow OH\text{-}C_2H_4 + e^-$

The photoelectron spectra for stable complexes are generated from the data set by enforcing coincidence of the detected photoelectron with a single heavy particle arriving at the position and time-of-arrival expected for the neutralized parent anion. Characterization of events as stable means that the neutral $OH\text{-}C_2H_4$ complexes do not dissociate with a significant KER (> 0.025 eV) during the ~8 μs flight time from the laser-ion interaction region to the neutral particle detector (QXDL) at the incident ion beam energy of 7 keV. In Figure 4.3. the stable photoelectron spectrum for $OH^-(C_2H_4)$ at $E_{h\nu} = 3.20$ eV is presented. The $OH^-(C_2H_4)$ spectrum (m/z = 45) is dominated by a peak at eKE = 0.91 eV and a small shoulder at eKE = 0.24 eV. In addition, a minor broad feature is seen at ~1.5 eV due to contributions from the ethoxide isomer.[34, 35] The photoelectron spectrum of $OH^-(C_2H_4)$ is similar to that previously reported for $OH^-(CH_4)$[30] consistent with a hydroxyl anion core inducing structural changes in the hydrocarbon. The dominant peak in the photoelectron spectra is broadened by 0.06 eV compared to OH^-, also shown in Figure 4.3., due to excitation of low-frequency van der Waals modes of the neutral complex. The shoulder ~0.37 eV lower in eKE is attributed to the symmetric (3149 or 3167 cm^{-1}) or asymmetric (3232 or 3258 cm^{-1}) stretches of the C_2H_4 moiety in the vdW.[24] These modes are unresolvable with our experimental resolution. The experimental vertical detachment energy (VDE) for the stable complexes is determined by the center of the dominant peak in the total (dissociative and stable) photoelectron spectrum and found to be 2.35 eV. The similarities of the photoelectron spectra for

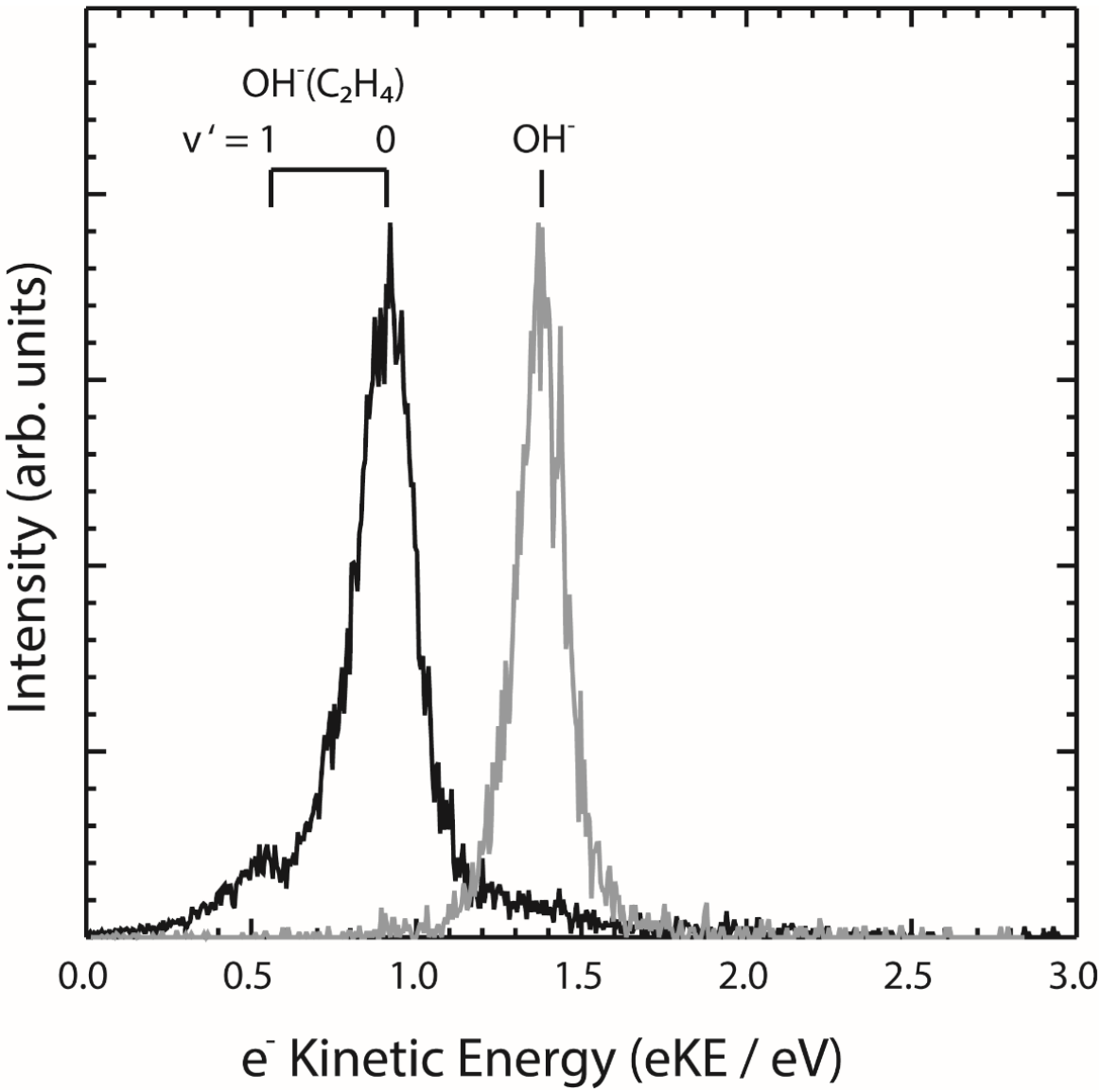

Figure 4.3. Overlaid photoelectron spectra of stable $OH^-(C_2H_4)$ (black) and OH^-(grey) with the main broad band centered on 0.91 and 1.38 eV, respectively. The shoulder peaking at 0.54 eV corresponds to v′=1 in the symmetric (3149 or 3167 cm^{-1}) or asymmetric (3232 or 3258 cm^{-1}) stretching modes of the C_2H_4 portion of the vdW.[24] This effectively also demonstrates the electron detector resolution ΔeKE/eKE ~ 5.6 %.

both stable and dissociative channels, shown in Figure 4.4., suggest that OH-C_2H_4 complexes may be predissociating along the 8 μs flight time contributing to the OH + C_2H_4 channel. With this caveat, it is noted that the stable channel makes up ~33% of the total stable and dissociative events collected.

4.3.2. Dissociative Photodetachment: $OH^-(C_2H_4) + h\nu \rightarrow OH + C_2H_4 + e^-$

The total energy spectrum corresponding to the dissociative OH + C_2H_4 + e^- photoelectron spectrum is shown in Figure 4.5. This spectrum shows the total energy, eKE + KER, for the photoelectron and photofragments detected in coincidence. Given the broadening observed in the experimental spectra, interpretation of the total energy spectrum is supported by the theoretical energetics reported in black in Figure 4.1. Using those energetics, two solid lines at 1.36 and 1.07 eV correspond to the maximum kinetic energies (KE_{max}) for the H_2O + $CHCH_2$ + e^- and OH + C_2H_4 + e^- channels, respectively. The dashed lines at 0.68-0.70 eV represent KE_{max} for one quantum of excitation in either the symmetric CH_2 stretches, ν_1 or ν_{11}, or asymmetric CH_2 stretches, ν_5 or ν_9, in the OH + C_2H_4 + e^- reactant channel, respectively.[36] Dashed lines at 0.30-0.33 eV correspond to two quanta of excitation in symmetric or asymmetric CH_2 stretching modes. At a photon energy of 3.20 eV there is enough energy to access the reactant, (1) OH + C_2H_4, or exit channel products, (2) H_2O + $CHCH_2$ and (3) H + CH_2CHOH. The center of mass spectrum of the 2-momentum matched products is shown in Figure 4.6. indicating photofragment masses centered at 17.8 and 27.1 amu. Due to the low kinetic energy release between the fragments and the QXDL resolution, photofragments of channels differing by 1 amu are unresolvable.

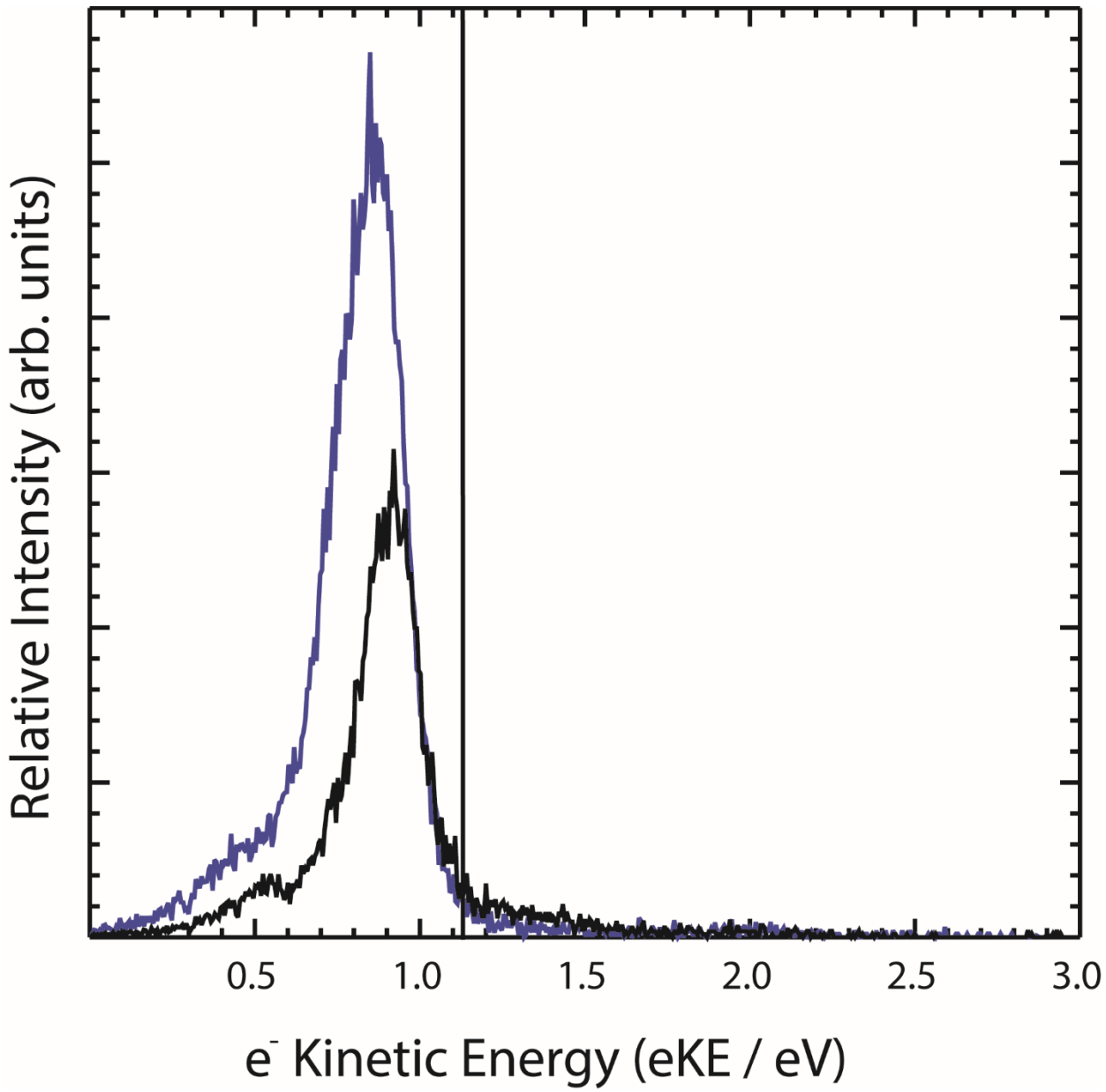

Figure 4.4. Overlaid photoelectron spectra of stable and dissociative channels. The stable contribution is shown in black and the photoelectrons for the dissociative channel are in blue. The vertical line at eKE = 1.13 eV corresponds to an adiabatic electron affinity of 2.07 eV for the entrance van der Waals complex.

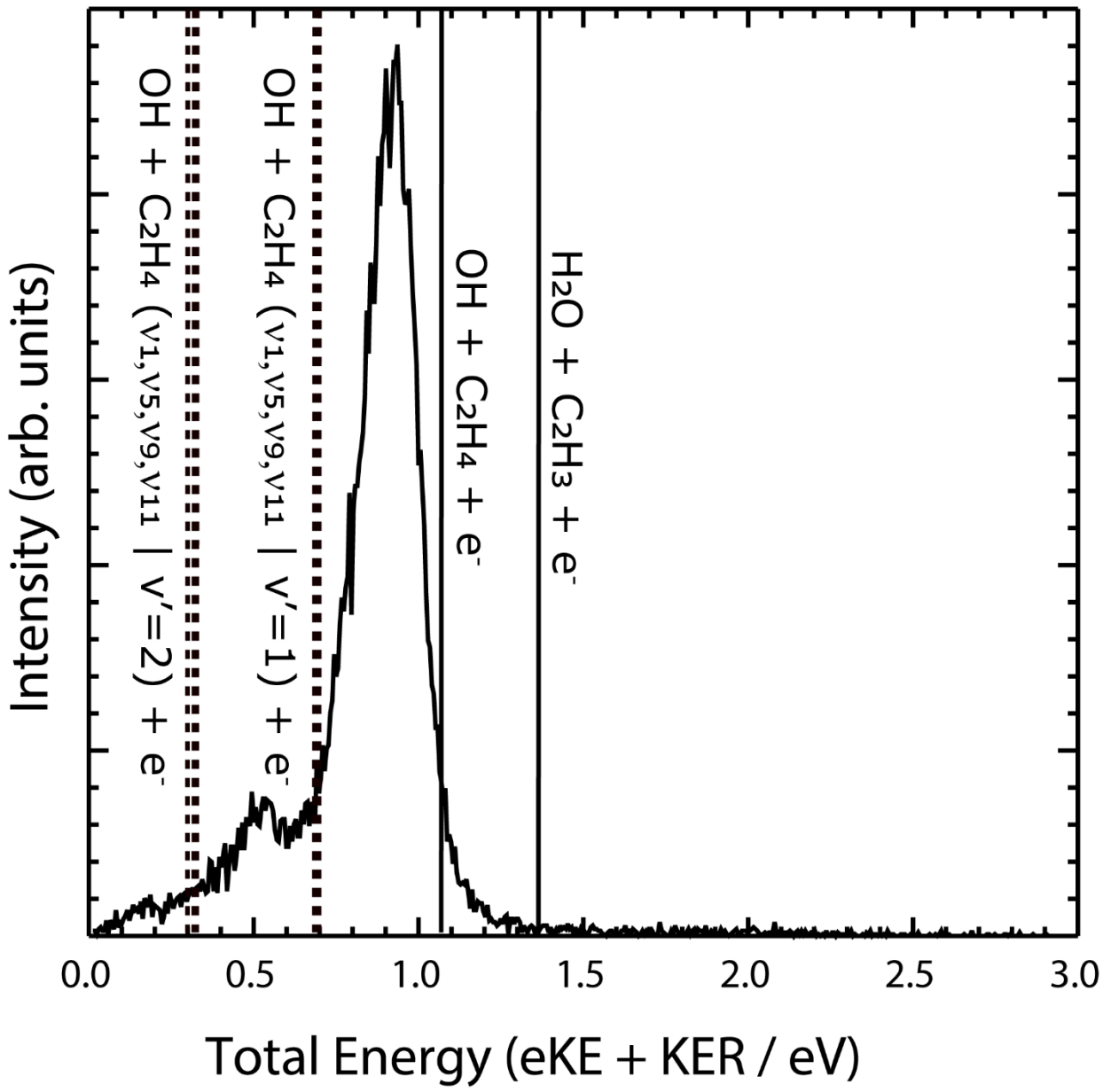

Figure 4.5. Total kinetic energy spectrum, eKE + KER, for dissociative photodetachment of $OH^-(C_2H_4)$. The solid vertical lines at 1.07 and 1.36 eV correspond to KE_{max} for the $OH + C_2H_4 + e^-$ and $H_2O + CHCH_2 + e^-$ channels, respectively. The dashed vertical lines at ~0.7 and ~0.3 eV correspond to the one and two quanta of excitation, respectively, in one of the two symmetric or two asymmetric CH_2 stretches of ethylene.

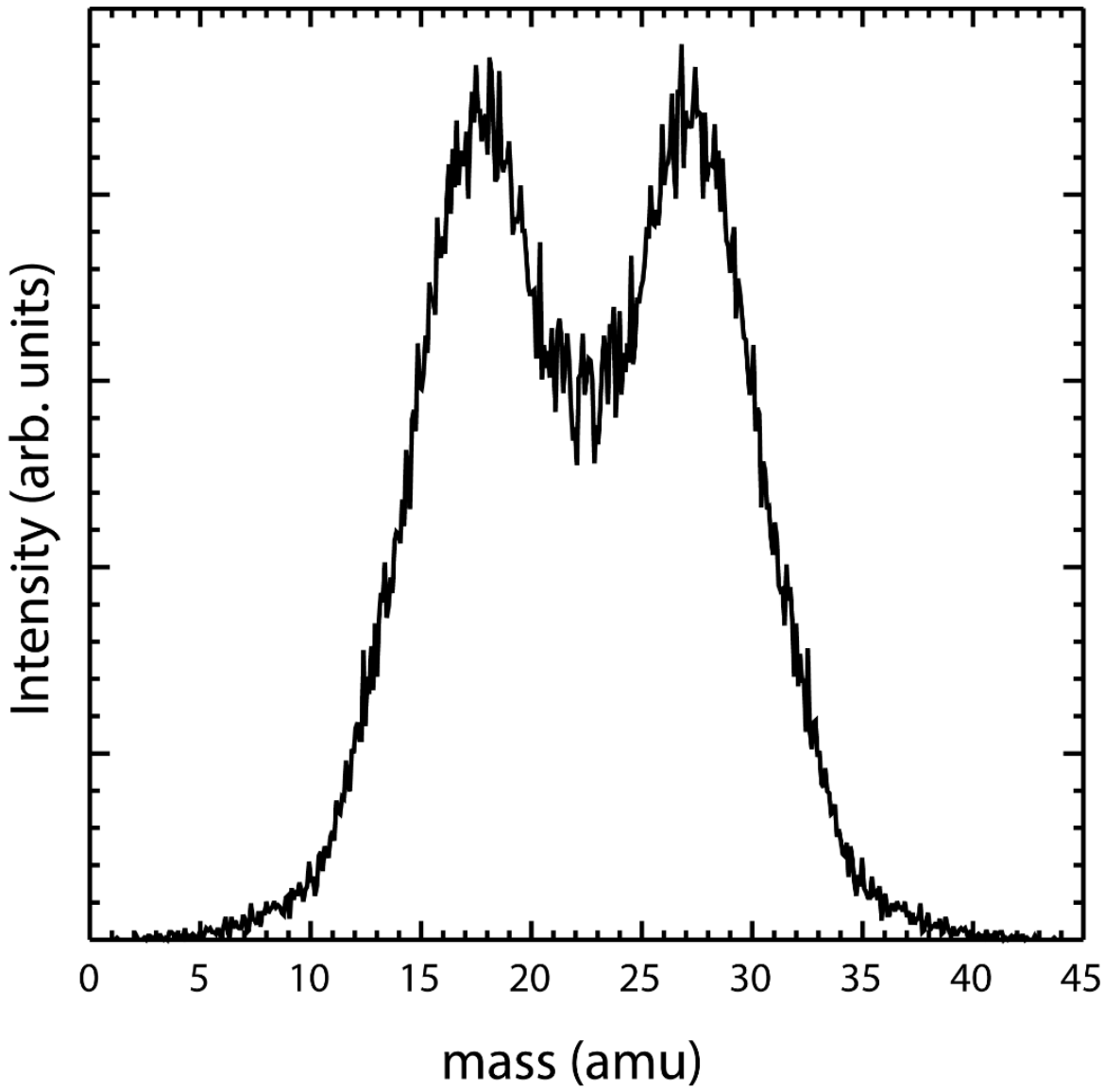

Figure 4.6. Center of mass spectrum for momentum matched photofragments, OH + C_2H_4. The photofragment masses are centered at 17.8 and 27.1 amu.

4.3.3. Ab initio Calculations

Geometry optimizations were computed using second-order MØller-Plesset (MP2) perturbation theory with correlation-consistent double-zeta basis set of Dunning augmented with diffuse functions (MP2/aug-cc-pVDZ) for the reactants, OH + C_2H_4, products, H_2O + $CHCH_2$ and H + CH_2CHOH, neutral van der Waals, CH_2CH_2OH adduct, and anion complexes. Single-point energy calculations were carried out at the coupled cluster singles, doubles, and perturbative triples level, CCSD(T), with the aug-cc-pVTZ basis set using the MP2/aug-cc-pVDZ optimized geometries. All calculations were performed using the Gaussian 09 package of programs.[37]

4.3.4. Impulsive Model

A simple impulsive model is used here to describe the energy partitioning of the nascent C_2H_4 photofragments formed upon DPD of $OH^-(C_2H_4)$. Simple impulsive models, assuming rigid or semirigid bonds in the resultant photofragment and that the state accessed is repulsive in the Franck-Condon region, have been used previously to account for the rotational energy partitioned to the photofragments. Here we use an impulsive model to qualitatively describe the DPD of $OH^-(C_2H_4)$ + hv → OH + C_2H_4 (v=0) + e^-. This model is a simplified version of that used by Ratliff and co-workers[8] for determining the angular momentum transferred to the resulting photofragments as a function of the measured recoil kinetic energy. Their prediction also included all the geometries along the zero-point level while here we only consider the minimum energy configuration of the anion. Additionally, we use this model to estimate rotational energy partitioning as a function of available energy. The available energy, E_{avail}, is 1.07 eV upon photon absorption of $OH^-(C_2H_4)$ yielding OH + C_2H_4 + e^- photofragments. This model assumes OH acts as a spectator and is rotationally cold, an assumption based on a previous DPD study on OH-CH_4 where OH fragments were found with minimal rotational excitation.[30] Thus, the rotational energy

is imparted to the C_2H_4 photofragment and the following expression for rotational energy, E_R, is used: $E_R = \frac{(\mu b^2)}{I} E_{avail}$

Where b is the impact parameter, μ is the reduced mass of OH and C_2H_4, and I is the moment of inertia about the axis of rotation of C_2H_4. Figure 4.7. shows the photoelectron-photofragment coincidence plot with the overlaid kinetic energy limit for this model.

4.4. Discussion

In this work, PPC spectroscopy was used to distinguish the energetics and dynamics of both stable and dissociative neutral states accessed from photodetachment of mass-selected precursor anions, $OH^-(C_2H_4)$. The precursor anion was generated in its ground vibrational state by using COAT to cool the internal degrees of freedom prior to photodetachment by 3.20 eV photons. Energy calculations carried out with Gaussian 09 were used to aid in the interpretation of the experimental findings and can be seen in Figure 4.1. compared to other energetics.[17, 24] The anion geometry for $OH^-(C_2H_4)$ is proposed and shown in Figure 4.2.

The results showed that the DPD of $OH^-(C_2H_4)$ yielded channels (1) $OH\text{-}C_2H_4 + e^-$ and (2) $OH + C_2H_4$ (v=0, 1, 2) + e^- at 3.20 eV photon energy. Channel (3), $H + CH_2CHOH$, however, is not accessed upon DPD due to the geometry structure of the precursor anion which has the electron density primarily focused on the OH moiety and has a similar geometry to TS2 on the $OH + C_2H_4 \rightarrow H_2O + CHCH_2$ neutral reaction surface. The dominant channel accessed was $OH + C_2H_4$ (v=0) + e^- with minor channels of 1 or 2 quanta of excitation in CH_2 symmetric or asymmetric stretching modes. Similar to the dissociation dynamics of $OH^-(CH_4)$, there is evidence for production of a long-lived weakly bound van der Waals complex in the entrance for the neutral reaction. Based on the experimental observations, the stable adduct CH_2CH_2OH was not formed

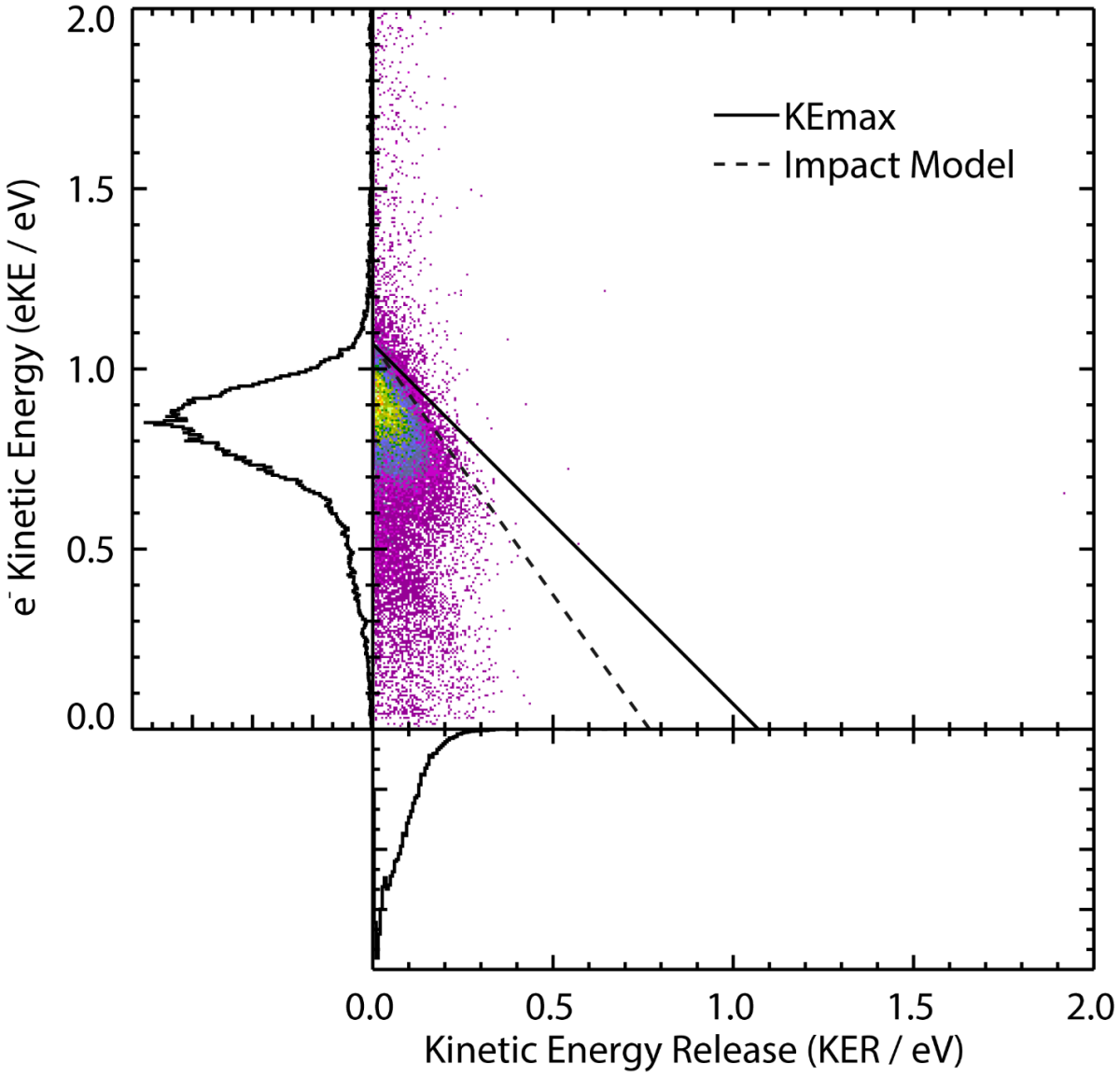

Figure 4.7. Photoelectron-photofragment coincidence plot of DPD of $OH^-(C_2H_4)$ at 3.20 eV photon energy. The KE_{max} and Impulsive model diagonal features corresponds to the energetic limit for OH + C_2H_4 (v=0) + e^- channel. The KE_{max} limit does not include rotational energy partitioning while the impulsive model limit does.

as no features appear in the photoelectron spectrum for stable events at 2.18 eV. The calculated structures for the anion and neutral complexes indicates that the Franck-Condon region for photodetachment of $OH^-(C_2H_4)$ lies near the van der Waals complex before the transition states, TS1 and TS2, leading to CH_2CH_2OH and $H_2O + CHCH_2$ channels, respectively. Due to the low kinetic energy release of the dissociating $OH + C_2H_4$ fragments, the stable contribution cannot be unambiguously separated from the dissociative channel. However, the observation of a stable component and the low kinetic energy release between the photofragments is consistent with the structural insights into the Franck-Condon region, explaining the dominance of the $OH + C_2H_4$ channel. Given the structure of the $OH^-(C_2H_4)$ precursor, the C_2H_4 photofragments from DPD are expected to be formed with rotational excitation proportional to the KER, supported by a simple impulsive model discussed below.

The photoelectron spectra for the stable van der Waals complex, $OH\text{-}C_2H_4$, has similar eKE features to the dissociative channel, shown in Figure 4.4., indicating that both are generated from the same state with the main broad features centered at 0.91 and 0.84 eV for stable and dissociative channels, respectively. The energetic shift of the peak positions of 0.07 eV is consistent with the expectation that higher degrees of internal excitation induced in the complex by photodetachment will lead to prompt dissociation. The dominant feature in the stable spectrum at 0.91 eV along with the shoulder at 0.24 eV, attributed to vibrational excitation of any one of the CH_2 symmetric and asymmetric modes, is strikingly similar to that of the $OH\text{-}CH_4$ system, and indicates that a long-lived complex exists on the excited vibrationally adiabatic surface, essentially a Feshbach resonance as observed in prior studies of $F + H_2O$ and $F + CH_3OH$.[38, 39] Many of the conclusions drawn here on the dynamics of $OH\text{-}C_2H_4$ are supported by observations made from the PPC studies on $OH\text{-}CH_4$. Using experimental results and the energetic calculations at the

CCSD(T)/aug-cc-pVTZ level, we calculate $D_0(OH^-\text{-}C_2H_4)$ = 0.30 eV compared to $D_0(OH^-\text{-}CH_4)$ = 0.24 eV. This is consistent with an expectation that the binding energy between OH^- and C_2H_4 would be stronger than that of $OH^-\text{-}CH_4$ due to the polarizability of the carbon-carbon double bond in C_2H_4. Since the interactions between OH^- and the simplest alkane and alkene are weak, it is expected that photodetachment of these solvated hydroxide clusters, would yield similar results.

Dissociative photodetachment of $OH^-(C_2H_4)$ primarily yields the $OH + C_2H_4 + e^-$ channel as expected from the proposed anion geometry resembling OH^- solvated with C_2H_4 and should therefore have the best Franck-Condon overlap with the transition state, TS2, between the entrance and exit channel. The minor channel for vibrational excitation derives from the expectation that the geometry change between the anion complex and the neutral products OH + C2H4 is not sufficient to induce significant amount vibrational excitation in the CH_2 symmetric and asymmetric modes, a result is also supported by the previous DPD and quasiclassical trajectory study on the $OH^-(CH_4)$ complex.[30] Additionally, for the v=0 case, significant rotational energy is expected to be partitioned to the C_2H_4 fragment owing to the direction of the impulse along the dissociating bond. To correctly model the DPD process, an accurate full-dimensional potential energy surface of the anion is required. However, theoretical construction of an accurate PES is a challenge for this eight-atom system containing three heavy atoms. Lacking theoretical treatment for the anion of this system, an impulsive model is used to account for rotational energy partitioning of the resulting photofragments in the dominant DPD process.

A simple impulsive model can account for rotational energy partitioned to the C_2H_4 photofragments as a function of the total energy available in DPD. The model used assumes that the geometry difference between the C_2H_4 moiety in $OH^-(C_2H_4)$ and the C_2H_4 photofragment is negligible, which is the case here. The C-H bond length in $OH^-(C_2H_4)$ and free C_2H_4 are 1.10 Å

and 1.08 Å,[40] respectively, so the dominant channel accessed is not expected to have significant symmetric/asymmetric stretching excitation in the resultant ethylene products. The impact parameter and moment of inertia at the anion equilibrium geometry are determined to be 0.31 Å and 3.57 amu Å^2, respectively. If there is no internal excitation induced in the photofragments, the KE_{max} is given by the solid diagonal feature at 1.07 eV in the PPC plot in Figure 4.7. Taking rotational excitation of the C_2H_4 fragments into account yields a KE limit that more closely resembles the observed slope for the OH + C_2H_4 channel. The weakly repulsive force between the dissociating fragments formed from DPD of $OH^-(C_2H_4)$ yields slowly recoiling fragments of low KER which also induces rotational excitation in the C_2H_4 fragment via a bending torque. These assumptions can be rationalized by geometric considerations of the minimum energy configuration of the precursor anion, shown in Figure 4.2., and does reflect the main features observed in the PPC plot.

Although OH + C_2H_4, H_2O + $CHCH_2$, and H + CH_2CHOH channels are accessible at the photon energy used in this study, the dominant channel accessed is the entrance channel reactants, OH + C_2H_4. Other DPD pathways must be considered, however. In a study of the fate of the hydroxyethyl radical (CH_2CH_2OH adduct) produced in the photodissociation of bromoethanol, quasiclassical trajectory calculations were reported that indicated a minor contribution for a roaming channel in the decomposition of the CH_2CH_2OH adduct leading to the H_2O + $CHCH_2$ channel at energies below the H-abstraction barrier.[17] The transition state (TS1) between the vdW and the adduct played a larger role in the H-abstraction than the outer transition state (TS2) because of the similarities in geometries between the vdW complex and the TS1. However, the precursor anion more closely resembles TS2 leading to H_2O + $CHCH_2$ so the DPD dynamics will differ. Even though the covalently bonded hydroxyethyl adduct was not accessed via PPC studies, the

entrance vdW complex was formed and could potentially contribute to the water channel through frustrated dissociation of OH leading to H-abstraction. Figure 4.5. shows higher energy events beyond the OH + C_2H_4 + e^- limit and below the threshold energy for the H_2O + $CHCH_2$ + e^- channel, so this may be a minor channel in the DPD of $OH^-(C_2H_4)$. Additionally, some portion of these long-lived vdW complexes may be in resonance with the vibrationally excited C_2H_4 products leading to dissociation to the reactants.

4.5. Conclusion

Photoelectron-photofragment coincidence measurements were carried out on the $OH^-(C_2H_4)$ clusters yielding channels (1) OH-C_2H_4 + e^- and (2) OH + C_2H_4 + e^-. The main channel observed is dissociative photodetachment yielding the ground state photofragments, OH + C_2H_4 + e^-. Excitation in the CH_2 symmetric and asymmetric stretches of C_2H_4 was also observed as a minor channel. A significant fraction (~33%) of the products are found to be stable OH-C_2H_4 vdW complexes but serves as an upper limit since some portion of these complexes may be predissociating. The similarities in photoelectrons for both stable and dissociative channels support vibrationally excited vdW complexes contributing to the formation of the OH and vibrationally excited C_2H_4 fragments via a resonance-mediated dissociation. Additionally, these vdW complexes may play a role in the formation of H_2O and $CHCH_2$, however that would be a much smaller channel. Upon photodetachment of $OH^-(C_2H_4)$, ethylene is expected to be formed with significant rotational excitation and is accounted for by using an impulsive model for DPD of OH + C_2H_4 (v=0) + e^-. Assuming the slowly recoiling C_2H_4 photofragments are imparted with some rotational motion via an impulsive model qualitatively explains the observed DPD dynamics of $OH^-(C_2H_4)$. This work helps elucidate relevant reaction pathways for the OH-C_2H_4 system via photodetachment of the precursor anion using the proposed minimum energy geometry for

$OH^-(C_2H_4)$. The dissociation dynamics for this $OH\text{-}C_2H_4$ system complements previous studies and demonstrates the ability to probe a different portion of the neutral PES via a rationalized precursor anion.

Acknowledgements

This material is based on work supported by the U.S. Department of Energy, Office of Science, Office of Basic Energy Sciences under Award Number DE-FG03-98ER14879.

Chapter 4 is in preparation for publication: Benitez, Y.; Parsons, A. J.; Lunny, K. G.; Continetti, R. E., Dissociation Dynamics of the $OH^-(C_2H_4)$ Complex. The dissertation author is the primary author. The corresponding author is the dissertation advisor, R. E. Continetti.

4.6. References

1. Ziemann, P. J., Effects of molecular structure on the chemistry of aerosol formation from the OH-radical-initiated oxidation of alkanes and alkenes. *Int. Rev. Phys. Chem.* **2011,** *30* (2), 161-195.

2. Cool, T. A.; Nakajima, K.; Mostefaoui, T. A.; Qi, F.; McIlroy, A.; Westmoreland, P. R.; Law, M. E.; Poisson, L.; Peterka, D. S.; Ahmed, M., Selective detection of isomers with photoionization mass spectrometry for studies of hydrocarbon flame chemistry. *J. Chem. Phys.* **2003,** *119* (16), 8356-8365.

3. Taatjes, C. A.; Hansen, N.; McIlroy, A.; Miller, J. A.; Senosiain, J. P.; Klippenstein, S. J.; Qi, F.; Sheng, L.; Zhang, Y.; Cool, T. A.; Wang, J.; Westmoreland, P. R.; Law, M. E.; Kasper, T.; Kohse-Höinghaus, K., Enols Are Common Intermediates in Hydrocarbon Oxidation. *Science* **2005,** *308* (5730), 1887.

4. Taatjes, C. A.; Hansen, N.; Miller, J. A.; Cool, T. A.; Wang, J.; Westmoreland, P. R.; Law, M. E.; Kasper, T.; Kohse-Höinghaus, K., Combustion Chemistry of Enols: Possible Ethenol Precursors in Flames. *J. Phys. Chem. A* **2006,** *110* (9), 3254-3260.

5. Tully, F. P., Hydrogen-atom abstraction from alkenes by OH, ethene and 1-butene. *Chem. Phys. Lett.* **1988,** *143* (5), 510-514.

6. Diau, E. W. G.; Lee, Y. P., Detailed rate coefficients and the enthalpy change of the equilibrium reaction $OH+C_2H_4=^{M}HOC_2H_4$ over the temperature range 544–673 K. *J. Chem. Phys.* **1992,** *96* (1), 377-386.

7. Yamada, T.; Bozzelli, J. W.; Lay, T., Kinetic and Thermodynamic Analysis on OH Addition to Ethylene: Adduct Formation, Isomerization, and Isomer Dissociations. *J. Phys. Chem. A* **1999,** *103* (38), 7646-7655.

8. Hippler, H.; Viskolcz, B., Addition complex formation *vs*. direct abstraction in the $OH+C_2H_4$ reaction. *Phys. Chem. Chem. Phys.* **2000,** *2* (16), 3591-3596.

9. Vakhtin, A. B.; Murphy, J. E.; Leone, S. R., Low-Temperature Kinetics of Reactions of OH Radical with Ethene, Propene, and 1-Butene. *J. Phys. Chem. A* **2003,** *107* (47), 10055-10062.

10. Cleary, P. A.; Romero, M. T. B.; Blitz, M. A.; Heard, D. E.; Pilling, M. J.; Seakins, P. W.; Wang, L., Determination of the temperature and pressure dependence of the reaction OH + C_2H_4 from 200-400 K using experimental and master equation analyses. *Phys. Chem. Chem. Phys.* **2006,** *8* (48), 5633-5642.

11. Zhang, J.; Yang, L.; Troya, D., Chemical Dynamics Simulations of the Hydroxyl Radical Reaction with Ethene. *Chin. J. Chem. Phys.* **2013,** *26* (6), 765-773.

12. Hintsa, E. J.; Zhao, X.; Lee, Y. T., Photodissociation of 2-bromoethanol and 2-chloroethanol at 193 nm. *J. Chem. Phys.* **1990,** *92* (4), 2280-2286.

13. Sapers, S. P.; Hess, W. P., Photodissociation of $BrCH_2CH_2OH$ and ICH_2CH_2OH: Formation and characterization of $OH(X\,^2\Pi)$. *J. Chem. Phys.* **1992,** *97* (5), 3126-3134.

14. Karpichev, B.; Koziol, L.; Diri, K.; Reisler, H.; Krylov, A. I., Electronically excited and ionized states of the CH_2CH_2OH radical: A theoretical study. *J. Chem. Phys.* **2010,** *132* (11), 114308.

15. Ratliff, B. J.; Womack, C. C.; Tang, X. N.; Landau, W. M.; Butler, L. J.; Szpunar, D. E., Modeling the Rovibrationally Excited C_2H_4OH Radicals from the Photodissociation of 2-Bromoethanol at 193 nm. *J. Phys. Chem. A* **2010,** *114* (14), 4934-4945.

16. Edwards, L. W.; Ryazanov, M.; Reisler, H.; Klippenstein, S. J., D-Atom Products in Predissociation of CD_2CD_2OH from the 202−215 nm Photodissociation of 2-Bromoethanol. *J. Phys. Chem. A* **2010,** *114* (17), 5453-5461.

17. Kamarchik, E.; Koziol, L.; Reisler, H.; Bowman, J. M.; Krylov, A. I., Roaming Pathway Leading to Unexpected Water + Vinyl Products in C_2H_4OH Dissociation. *J. Phys. Chem. Lett.* **2010,** *1* (20), 3058-3065.

18. Ratliff, B. J.; Alligood, B. W.; Butler, L. J.; Lee, S.-H.; Lin, J. J.-M., Product Branching from the CH_2CH_2OH Radical Intermediate of the OH + Ethene Reaction. *J. Phys. Chem. A* **2011,** *115* (33), 9097-9110.

19. Tully, F. P., Laser photolysis/laser-induced fluorescence study of the reaction of hydroxyl radical with ethylene. *Chem. Phys. Lett.* **1983,** *96* (2), 148-153.

20. Liu, A.; Mulac, W. A.; Jonah, C. D., Kinetic isotope effects in the gas-phase reaction of hydroxyl radicals with ethylene in the temperature range 343-1173 K and 1-atm pressure. *J. Phys. Chem.* **1988,** *92* (13), 3828-3833.

21. Greenwald, E. E.; North, S. W.; Georgievskii, Y.; Klippenstein, S. J., A Two Transition State Model for Radical−Molecule Reactions: A Case Study of the Addition of OH to C_2H_4. *J. Phys. Chem. A* **2005,** *109* (27), 6031-6044.

22. Alvarez-Idaboy, J. R.; Mora-Diez, N.; Vivier-Bunge, A., A Quantum Chemical and Classical Transition State Theory Explanation of Negative Activation Energies in OH Addition To Substituted Ethenes. *J. Am. Chem. Soc.* **2000,** *122* (15), 3715-3720.

23. Sosa, C.; Schlegel, H. B., Calculated barrier heights for OH + C_2H_2 and OH + C_2H_4 using unrestricted Moeller-Plesset perturbation theory with spin annihilation. *J. Am. Chem. Soc.* **1987,** *109* (14), 4193-4198.

24. Senosiain, J. P.; Klippenstein, S. J.; Miller, J. A., Reaction of Ethylene with Hydroxyl Radicals: A Theoretical Study. *J. Phys. Chem. A* **2006,** *110* (21), 6960-6970.

25. Shubert, V. A.; Rednic, M.; Pratt, S. T., Photodissociation of 2-Iodoethanol within the A Band. *J. Phys. Chem. A* **2009,** *113* (32), 9057-9064.

26. Xu, Z. F.; Xu, K.; Lin, M. C., Ab Initio Kinetics for Decomposition/Isomerization Reactions of C_2H_5O Radicals. *ChemPhysChem* **2009,** *10* (6), 972-982.

27. Johnson, C. J.; Shen, B. B.; Poad, B. L. J.; Continetti, R. E., Photoelectron-photofragment coincidence spectroscopy in a cryogenically cooled linear electrostatic ion beam trap. *Rev. Sci. Instrum.* **2011,** *82* (10), 105105.

28. Shen, B. B.; Benitez, Y.; Lunny, K. G.; Continetti, R. E., Internal energy dependence of the photodissociation dynamics of O_3^- using cryogenic photoelectron-photofragment coincidence spectroscopy. *J. Chem. Phys.* **2017,** *147* (9), 094307.

29. Lu, Y.-J.; Lehman, J. H.; Lineberger, W. C., A versatile, pulsed anion source utilizing plasma-entrainment: Characterization and applications. *J. Chem. Phys.* **2015,** *142* (4), 044201.

30. Benitez, Y.; Lu, D.; Lunny, K. G.; Li, J.; Guo, H.; Continetti, R. E., Photoelectron–Photofragment Coincidence Studies on the Dissociation Dynamics of the OH–CH_4 Complex. *J. Phys. Chem. A* **2019,** *123* (23), 4825-4833.

31. Wiley, W. C.; McLaren, I. H., Time-of-Flight Mass Spectrometer with Improved Resolution. *Rev. Sci. Instrum.* **1955,** *26* (12), 1150-1157.

32. Bowen, M. S.; Continetti, R. E., Photodetachment Imaging Study of the Vinoxide Anion. *J. Phys. Chem. A* **2004,** *108* (39), 7827-7831.

33. Hanold, K. A.; Continetti, R. E., Photoelectron–photofragment coincidence studies of the dissociative photodetachment of O_4^-. *Chem. Phys.* **1998,** *239* (1), 493-509.

34. Ramond, T. M.; Davico, G. E.; Schwartz, R. L.; Lineberger, W. C., Vibronic structure of alkoxy radicals via photoelectron spectroscopy. *J. Chem. Phys.* **2000,** *112* (3), 1158-1169.

35. Poad, B. L. J.; Ray, A. W.; Continetti, R. E., Dissociative Photodetachment of the Ethoxide Anion and Stability of the Ethoxy Radical CH_3CH_2O•. *J. Phys. Chem. A* **2013,** *117* (46), 12035-12041.

36. Shimanouchi, T., Tables of Molecular Vibrational Frequencies Consolidated Volume I. National Bureau of Standards, 1972; pp 1-160.

37. B.; Petersson, G. A.; al., e., Gaussian 09, revision A.02; . Gaussian Inc.: Wallingford, CT: 2009.

38. Otto, R.; Ma, J.; Ray, A. W.; Daluz, J. S.; Li, J.; Guo, H.; Continetti, R. E., Imaging Dynamics on the F + H_2O → HF + OH Potential Energy Surfaces from Wells to Barriers. *Science* **2014,** *343* (6169), 396.

39. Ray, A. W.; Agarwal, J.; Shen, B. B.; Schaefer, H. F.; Continetti, R. E., Energetics and transition-state dynamics of the F + $HOCH_3$ → HF + OCH_3 reaction. *Phys. Chem. Chem. Phys.* **2016,** *18* (44), 30612-30621.

40. Herzberg, G., *Electronic spectra and electronic structure of polyatomic molecules*. Van Nostrand New York, 1966.

Chapter 5: Probing the Exit Channel of the OH + $CH_3OH \rightarrow H_2O + CH_3O$ Reaction by Photodetachment of $CH_3O^-(H_2O)$

5.1. Introduction

The reaction between the simplest alcohol, CH_3OH, with the hydroxyl radical, OH, represents an interesting reaction relevant to cold interstellar chemistry.[1] Methanol is one of the most abundant organic molecules in space and is thought to desorb from icy grains in the interstellar medium (ISM) at low temperatures via photodesorption or chemically reactive processes.[2] It has been proposed to be one of the main sources for complex organic molecules in the ISM.[3] Additionally, the hydroxyl radical is the main oxidizer in both atmospheric and combustion processes so the reaction with methanol provides a sink for this simple alcohol in the troposphere. Owing to the importance of these species in various environments, many kinetic[1, 4-7] and theoretical studies[8-12] have been carried out over a range of temperatures and pressures. In particular, the negative temperature dependence of the total reaction rate at low temperatures has led to many investigations that highlight the significant role the pre-reactive complex has in the kinetics of this reaction. Namely, in facilitating tunnelling through the H-abstraction barrier to CH_3O products at low temperatures. This result[1] has motivated numerous studies[2, 7-9, 11-14] with significant implications towards bimolecular cold chemistry occurring in the ISM, which has previously been overlooked as a source for complex organic molecules.[9, 15, 16]

At low temperatures, this reaction is promoted by an association reaction which yields a weakly bound neutral complex or pre-reactive complex. This pre-reactive complex is thought to have a relatively long lifetime due to long-range interactions and leads to two different transition states producing water along witheither methoxy, OCH_3, or hydroxymethyl, CH_2OH, radicals.[1]

Relative to the reactant asymptote, OH + CH_3OH, the transition state (TS2) leading to methoxy radical has a larger barrier height of 0.10 eV compared to 0.02 eV for the TS1 leading to hydroxymethyl radical making the latter product thermodynamically more favorable. However, it was discovered[1] that the rate coefficients to product formation increased with decreasing temperature < 250 K yielding a V-shaped temperature dependence for the rate constant. This result was unexpected since the large barrier heights to product formation should, classically, inhibit product formation at lower temperatures. Thus the evaluation of the role that the pre-reactive complex played in the kinetics of this reaction became a point of interest motivating studies with significant implications towards bimolecular cold chemistry occurring in the ISM, previously largely overlooked as a source for complex organic molecules.[15, 16]

The deviation from Arrhenius behavior for this reaction can be explained by considering the pre-reactive complex and the role of quantum dynamical effects. Heard and co-workers showed that the experimental rate coefficient of OH + CH_3OH increases by 2 orders of magnitude from 200 K as the temperature decreases to 63 K.[1] This observation was supported by statistical rate theory master equation calculations using quantum mechanical tunneling (QMT) and the potential energy surface (PES) of Xu and Lin.[8] Their results showed that CH_3O becomes the dominant product at temperatures < 250 K likely owing to increased tunneling through a thinner energy barrier compared to the pathway leading to CH_2OH products. Experiments that followed were focused on the lower temperature regime and the pressure dependence of the rate coefficient of this reaction.[2]

The pressure dependence of this reaction has been studied in both the low-pressure limit and the high-pressure limit.[9] In the high-pressure limit, the pre-reactive complex can be stabilized and therefore help to facilitate tunnelling through the barrier to OCH_3 and water products.

However, in the low-pressure limit, collisional stabilization of the entrance channel complex is not favored, and therefore the reaction would proceed only via H-abstraction. It was determined, however, that below 120 K, the rate coefficient is essentially pressure independent. Using the competitive canonical united statistical (CCUS) model, Gao and co-workers[9] determined that the rate coefficients below 100 K are close to those in the high-pressure limit.[13] Lam and Stanton used 2D master equation methods to calculate pressure dependent rate constants between 10-100 K and found that the rate constants in the low-pressure limit depend less on pressure at 10 K than at 100 K.[14] Mazo-Sevillano and co-workers showed that using ring polymer molecular dynamics (RPMD) which accounts for zero-point energy (ZPE) and tunnelling effects, gave results that agreed with experiment in the low-pressure limit.[11]

While many studies on this reaction have focused on the pre-reactive complex and its influence on the rate coefficients at low temperatures, the reverse bimolecular reaction between $H_2O + CH_3O$ has not been studied as extensively as it is not as significant a reaction in atmospheric and combustion processes compared to, for example, $OH + CH_3OH$ or $CH_3O + O_2$ reactions. However, solvated neutral and ionic clusters relevant to these exit channel products and the roles they may play in the isomerization of methoxy radicals are still relevant in atmospheric and combustion contexts.[17, 18] Unimolecular decomposition and isomerization phenomena have been investigated for both the methoxy radical[19, 20] and the methoxide anion[21, 22] clustered with water. The relative stability of the anionic H-bonded network in methoxide clustered with water, $CH_3O^-(H_2O)_n$, was investigated and the stepwise replacement of water by methanol was found to be exoergic, suggesting methanol is a better solvent than water for RO^- centers.[21, 22] Solvated molecules have an influence on the dynamics in microsolvated reactions where a reduction in reaction rates is the observed trend.[23] However, it should be noted that microsolvation of S_N2

reactions have been shown to have more indirect mechanisms to reaction with pre-reaction complexes and intermediates playing a significant role as is the case with reactions involving $OH^-(H_2O)$ compared to OH^-.[24, 25] Additionally, the isomerization of CH_3O to CH_2OH is thought to be an important process in the loss of methoxy radical in the atmosphere. Previous studies have evaluated this unimolecular isomerization catalyzed by atmospherically relevant species, including H_2O, by reducing the barrier compared to direct isomerization.[19, 20] Using *ab initio* methods, this reaction was found to proceed via a pre-reactive complex where tunnelling may play a role at temperatures >210 K.[19] This pre-reactive complex formed by the association of CH_3O and H_2O, called the exit-channel complex in this work, may help facilitate other reaction pathways and is important in the reaction dynamics of the title reaction presented here (as will be discussed later). Although the methoxy radical primarily reacts with O_2 in the atmosphere, understanding other sink sources for this simplest alkoxy radical such as thermal decomposition or stabilization in an adduct can shed insights into its reactivity.[18]

In this work, the potential energy surface governing the $OH + CH_3OH \rightarrow H_2O + CH_3O$ reaction is studied by photoelectron-photofragment coincidence (PPC) spectroscopy where a precursor anion is prepared with a similar configuration to the transition state.[26] Photodetachment and/or dissociative photodetachment (DPD) of the precursor anion probes the dynamics near the transition state on the neutral PES governed by the Franck-Condon overlap between the neutral and the precursor anion. Using PPC spectroscopy, anions can be prepared, mass-selected, and interrogated with a fixed-frequency laser yielding electrons and the resultant neutral fragment(s) which are collected in coincidence on an event-by-event basis.[27] This approach allows for the separation of stable (1 particle + $1e^-$) and dissociative (2 momentum-matched fragments + e^-) events and can help unravel the dissociation dynamics occurring on the neutral potential energy

surface (PES). In the PPC studies reported here, anions at m/z = 49 were prepared and interrogated with a 3.20 eV photon energy to map onto the OH + CH_3OH → H_2O + CH_3O reaction. While the initial target was $HO^-(HOCH_3)$ to probe the entrance reactants, H_2O + CH_3OH, high-level coupled cluster calculations of the stationary points on the anion surface showed that this anion cannot be stabilized and the minimum energy configuration is instead $CH_3O^-(H_2O)$. The structure of the minimum energy configuration of $CH_3O^-(H_2O)$ shows that in PPC studies the best Franck-Condon overlap with the exit-channel complex is in the vicinity of TS2 on the repulsive neutral PES (as seen in Figure 5.1.). Photodetachment of the anions was found to yield both stable, (1) CH_3O-HOH + e^-, and dissociative (2) H_2O + CH_3O + e^-, exit channel products including minor channels with excitation in the relevant local and free water vibrational modes. Interpretation of the photodetachment and DPD processes were aided by new high-level coupled-cluster calculations for the anion and neutral potential energy surface and will be discussed in the sections that follow.

5.2. Experiment

The experiments were conducted using a cryo-PPC spectrometer that has previously been described.[28, 29] In brief, precursor anions were generated via a supersonic expansion from a pulsed valve passing through a coaxial discharge source with a counterpropagating electron beam. The expansion contained a gas mixture of 5:45:50 N_2O/Ar/CH_4, over methanol. A Wiley-McLaren type mass spectrometer[30] extracted the ion packet perpendicularly and focused the ions in a cryogenic octupole accumulation trap (COAT).[24] COAT was used to prepare the precursor anions in their ground vibrational state via buffer gas cooling of internal modes. After 40 ms, the ions are extracted and accelerated up to 6.8 keV beam energy and re-referenced to ground. A series of ion optics help to steer and focus the mass-selected precursor anions into an electrostatic ion beam trap

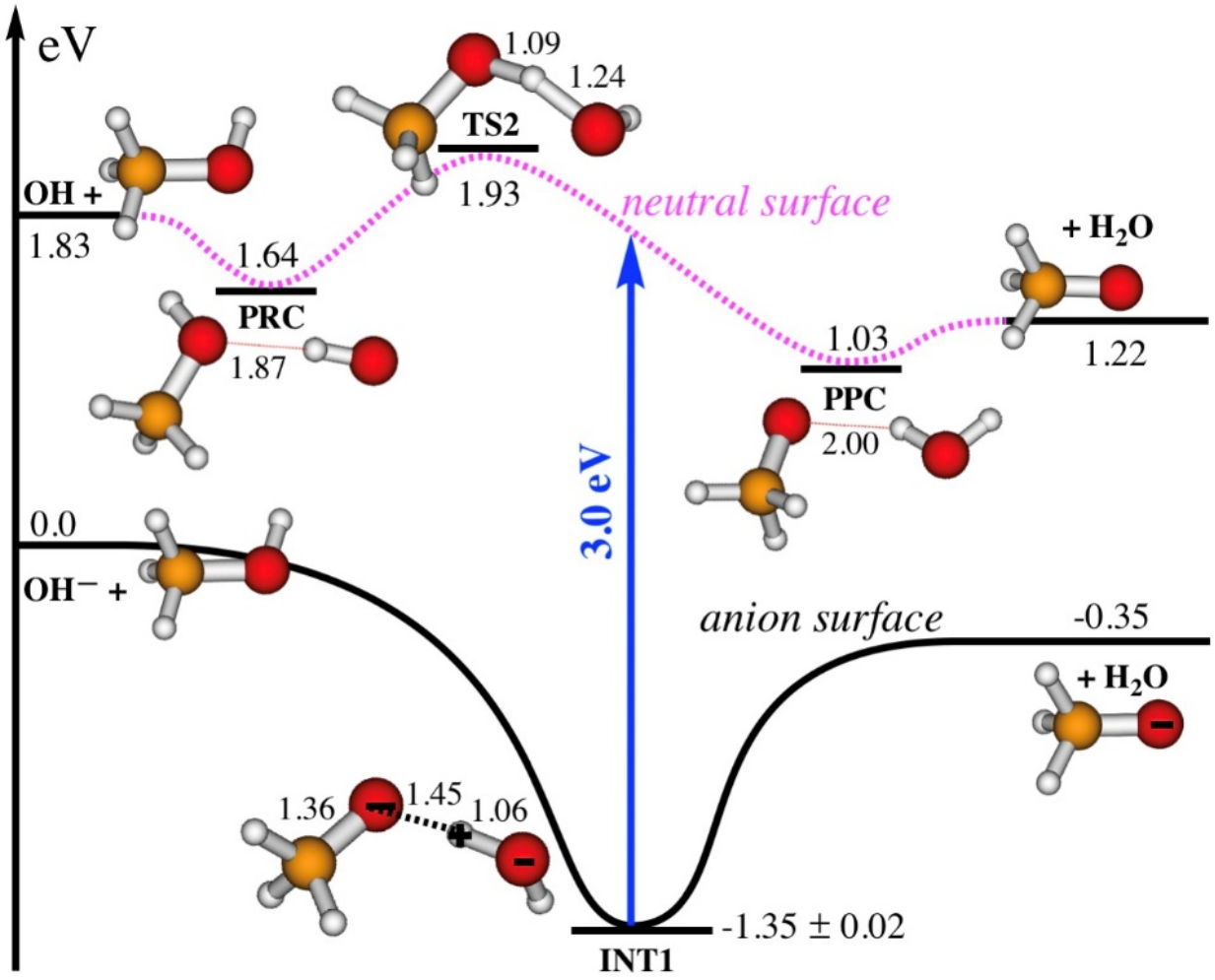

Figure 5.1. Relevant reaction diagram proposed for the anion and neutral potential energy surfaces calculated at the mHEAT-345(Q) method.

(EIBT). The EIBT is a linear storage device and upon entry, the entrance stack of mirrors are switched to repulsive potential from ground, thereby trapping and storing the ions for up to 100ms. During the trapping period, the ions are interrogated with a 388 nm (E_{hv} = 3.20 eV) laser pulse from a Ti:Sapphire regenerative amplifier (Clark MXR CPA-2010; 1.2 ps pulse width) at a 1 kHz repetition rate (decoupled from the 10 Hz rep rate of the source). The photodetached electrons are extracted perpendicular to the ion-laser interaction region and are velocity mapped onto a time and position sensitive detector. The resultant neutral fragment(s) recoil out of the EIBT at the parent beam energy and are detected by a multiparticle time and position sensitive detector ~1.3 m downstream. Using the measured time of arrival and positions of the photoelectrons and photofragment(s) the center-of-mass electron kinetic energies (eKE) and kinetic energy release (KER) and product mass ratios, respectively, can be determined. Calibration spectra of OH^- and CH_3O^- showed ΔeKE/eKE resolution of 5.5 % full-width-half-max (FWHM) at eKE = 1.36 and 1.62 eV, respectively. The neutral particle detector was calibrated by collecting a dissociative photodetachment (DPD) spectrum of O_4^- showing a ΔKER/KER resolution of ~10% FWHM at 0.4 eV.[31] Due to the low kinetic energy release between the fragments in this study and the QXDL resolution, photofragments of a different channel differing by 1 amu are unresolvable.

5.3. Quantum Chemical Calculations

High-level coupled-cluster calculations were computed for both neutral and anion potential energy surfaces (PES). Points along the neutral PES were calculated with an mHEAT-345(Q) method, as reported previously.[14] In brief, mHEAT is a composite method[32] based on high-level coupled-cluster calculations. First, the stationary point geometries are optimized with fc-CCSD(T)/ANO1 level of theory. Single-point energies are then done with CCSD(T) and Dunning's cc-pVXZ basis sets[33] (where X = T, Q and 5); and electronic energies are subsequently

extrapolated to the basis set limit. Next, higher-level energy corrections comprising full iterative triple excitations and non-iterative quadruple excitations arising from the perturbation theory are also included. In addition, the energies are corrected by anharmonic zero-point vibrational energies (ZPE), which are obtained with vibrational second-order perturbation theory (VPT2).[34] Lastly, other smaller corrections such as DBOC, scalar relativity effects, and spin-orbit coupling are also included.[32] It has been shown elsewhere that the mHEAT method can give an accuracy of better 2 kJ mol^{-1} for relative energies.[32]

For the OH^- + CH_3OH reaction occurring on the anion PES, a method similar to mHEAT-345(Q) is also used. However, to better treat an ionic species, suitable diffuse functions need to be added. In this work, Dunning's aug-cc-pVXZ basis sets (where X = T, Q and 5) have been used to replace cc-pVXZ in the original mHEAT protocol. As seen in Figure 5.1., two reaction enthalpies calculated for the OH^- + CH_3OH reaction agree well (within 0.5 kJ mol^{-1}) with the benchmark ATcT values.[35] A similar accuracy may be also expected for the other stationary points.

5.4. Results and Discussion

The OH + CH_3OH reaction neutral reaction coordinate was characterized using the mHEAT-345(Q) method, reported previously,[14] and a similar method was used to determine the energetics of the stationary points for the OH^- + $CH_3OH \rightarrow H_2O + CH_3O^-$ reaction. Figure 5.1. shows the association of OH^- and CH_3OH that occurs on the anion PES where OH^- can attack CH_3OH in different directions. The attack of OH^- on the OH-group takes place on an attractive surface and directly leads to the formation of the anion adduct $CH_3O^-(H_2O)$, where the CH_3O—HOH bond length is ~1.45 Å while that of the CH_3O-H—OH is ~1.06 Å, thus the geometry of the anion looks like TS2 on the neutral PES that has corresponding bond lengths of 1.09 and 1.24 eV,

respectively. A Milliken charge analysis shows that the anion is formed by dipole-dipole interactions with a positive charge located at the H-atom while two negative charges are located at the other two O atoms, $CH_3O^{\delta-}$—$H^{\delta+}$—$^{\delta-}$OH. These interactions result in a strongly bound complex with a binding energy of 1.01 eV relative to the CH_3O^- + H_2O asymptote. OH^- can also attack to the CH_3-group of CH_3OH to give another complex with a binding energy of 0.21 eV (not shown in Figure 5.1.). This complex is found to be thermally unstable and spontaneously converts to the $CH_3O^-(H_2O)$ anion. Furthermore, the vertical detachment energy (VDE) calculated with the mHEAT method is 3.0 eV, about 0.2 eV lower than the photon energy used in the experiment and, upon photodetachment and DPD, the resultant products are expected to lie on the exit side of the reaction, in agreement with experimental observations.

Photoelectron spectra for both stable and dissociative channels are shown in Figure 5.2. demonstrating similarities in the electron kinetic energies (eKE). The computed adiabatic electron affinity (AEA) for the exit-channel complex supports assignment of the exit-channel complex, CH_3O-H_2O, as the stable photoneutral accessed upon photodetachment. Dashed vertical lines at 0.33, 0.35, and 0.62 eV corresponds to 1 quanta of excitation in the asymmetric, ν_{18}, symmetric, ν_{17}, and bending, ν_{13}, modes of the water moiety in the exit-channel complex. It appears that the exit-channel complex is being formed predominantly with bending excitation in the local water moiety. From a geometric stand-point, these vibrational modes are relevant for the reaction coordinate upon photodetachment of $CH_3O^-(H_2O)$. As shown in Figure 5.1., the precursor anion has a geometry similar to TS2 but has a CH_3O—HOH bond length that lies between TS2 and the exit-channel complex. Additionally, the shared hydrogen is closer to the oxygen in the water moiety in the exit-channel complex by ~0.1 Å which could lead to O—H water stretching excitation and since it's a local mode, both symmetric and asymmetric excitations would be

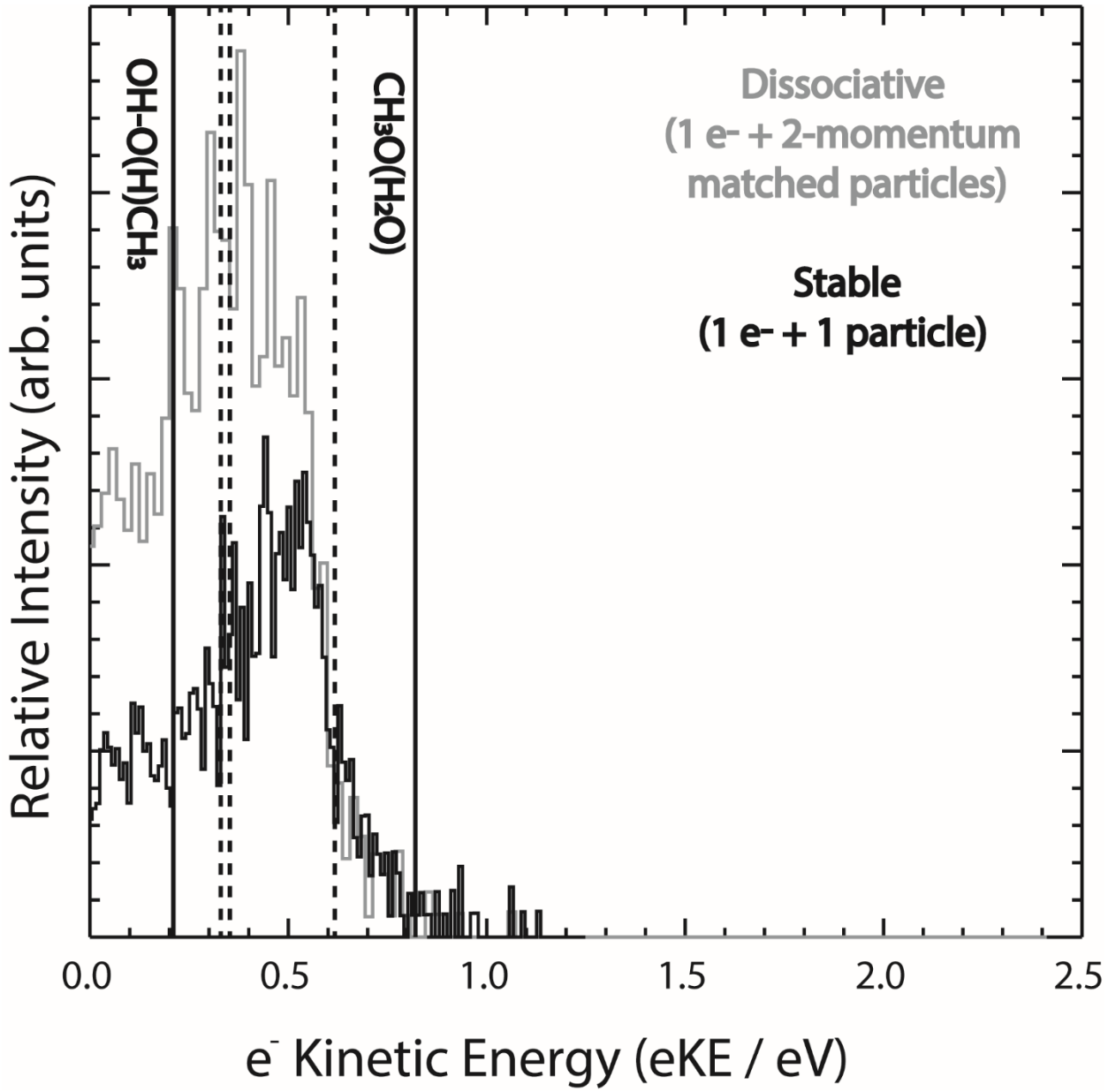

Figure 5.2. Photoelectron spectra for stable (black) and dissociative (grey) events. The solid vertical lines correspond to the computed AEAs for the pre-reactive complex and the exit-channel complex at 0.21 and 0.82 eV, respectively. The dashed vertical lines at 0.33, 0.35, and 0.62 eV correspond to excitation in the water asymmetric, symmetric, and bending local modes of the exit-channel complex, respectively.

involved as previously determined in a similar PPC study on OH-(CH_4).[36] Additionally, the H-O-H bond angle in the precursor anion and the exit-channel complex are 101.1° and 104.7°, respectively, so the resultant exit-channel complex is expected to have local water bending excitation in the exit-channel complex. The C—O and C—H bond lengths in the methoxy moiety for both the precursor anion and the exit-channel complex differ slightly by 0.02 Å so local methoxy modes are not expected to be vibrationally excited.

The lack of structure near 0.33-0.35 eV in Figure 5.2. corresponding to the local O-H stretching modes in the water moiety in the exit-channel complex does not rule out the formation of these vibrationally excited exit-channel complexes. The width of these peaks may be broadened causing a blurring of the photoelectron peaks due to low frequency excitations particularly from the water and methoxy rocking mode, ν_4. Additionally, there are no resolved features in the photoelectron spectra of the dissociative channel. This is not too surprising a result since the methoxy radical is known to be formed with significant rotational excitation as determined by the analogue studies on F-CH_3OH[37, 38] where HF products took away most of the energy in vibrations. The pre-reactive complex is energetically accessible in these experiments and the AEA limit is marked on the photoelectron spectra, however, due to its proximity to the O—H stretching excitations in the exit-channel complex and the lack of structure, the involvement of this pre-reactive complex is purely speculative, and unlikely given the structure of the precursor $CH_3O^-(H_2O)$ anion.

The stable channel makes up ~47 % of total events with the dominant channel being DPD to water and methoxy radical products. Comparing the photoelectron spectra for the stable and dissociative channels can yield important information about the nature of each channel. The stable peaks at 0.52 eV while the dissociative channel is shifted to lower eKE by ~0.1 eV. Both result in

broad indiscernible features that are strikingly similar. Since direct DPD yields slowly recoiling $H_2O + CH_3O$ fragments resulting in a low center-of-mass kinetic energy release (KER) peaking at 0.07 eV, fragments with low KER are difficult to distinguish from stable events. One approach, however, is to compare the photoelectron spectra of the stable and the low KER dependence on eKE of the dissociative channel as shown in Figure 5.3. Gating for low KER events, 0-0.05 eV, yields a photoelectron spectrum with a reduction in the dominant feature at 0.52 eV. This finding suggests that upon photodetachment, a portion of the stable photoneutrals formed with local vibrational excitation in the O—H symmetric and asymmetric modes in the water moiety may be trapped in the exit channel van der Waals (vdW). While these complexes are referred to as stable, it should be noted that all the experiment shows is that they are long-lived on the timescale of the flight time of 7.8 μs for the photofragment(s) to reach the detector given at the parent anion beam energy of 6.8 keV. These long-lived Feshbach resonances are associated with the vibrationally excited exit channel products, H_2O (ν_1, ν_3 | v=1) + CH_3O + e^-. Considering that the dominant eKE peak in the stable photoelectron spectrum is below the $H_2O + CH_3O + e^-$ asymptotic limit, it's likely that all of the "stable" fragments collected here are Feshbach resonances trapped in the vibrationally excited (symmetric and asymmetric stretching modes) $H_2O(v'=1)$-OCH_3 vdW well. In addition, it is noted that the involvement of the water bending mode in this process may not be as significant since the feature at 0.52 eV is not as prominent in the low-KER gated photoelectron spectrum compared to the stable spectrum.

The dominant direct DPD process can be examined in a PPC spectrum with correlation of the eKE and KER for each photoelectron-photofragment coincidence event plotted as a two-dimensional histogram in the DPD of $CH_3O^-(H_2O)$ as shown in Figure 5.4. The partitioning of kinetic energy in DPD between the photoelectron or photofragments is governed by energy

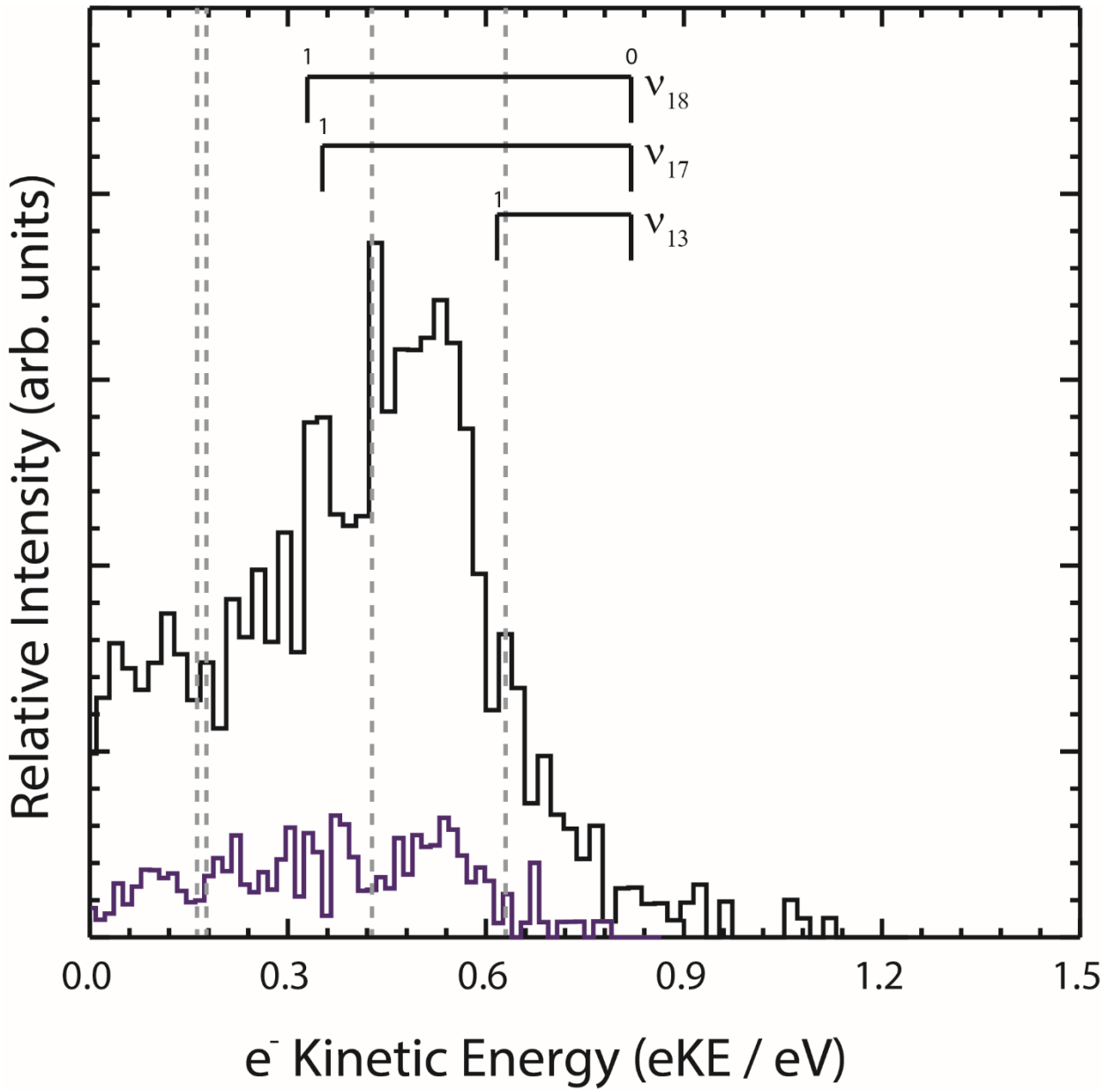

Figure 5.3. Photoelectron spectra for stable (black) and low KER gates of dissociative channel. The stable spectrum is binned differently than in Figure 5.2. The purple trace corresponds to 0-0.05 eV KER gates. The relevant vibrational modes in the exit-channel complex are noted by the vibrational combs. The grey dashed vertical lines at 0.63 corresponds to the KE_{max} for $H_2O + CH_3O + e^-$ product channel. The dashed vertical lines at 0.43, 0.18, and 0.16 eV are KE_{max} for one quanta of excitation in the water bend, symmetric stretch, and asymmetric stretching modes, respectively.

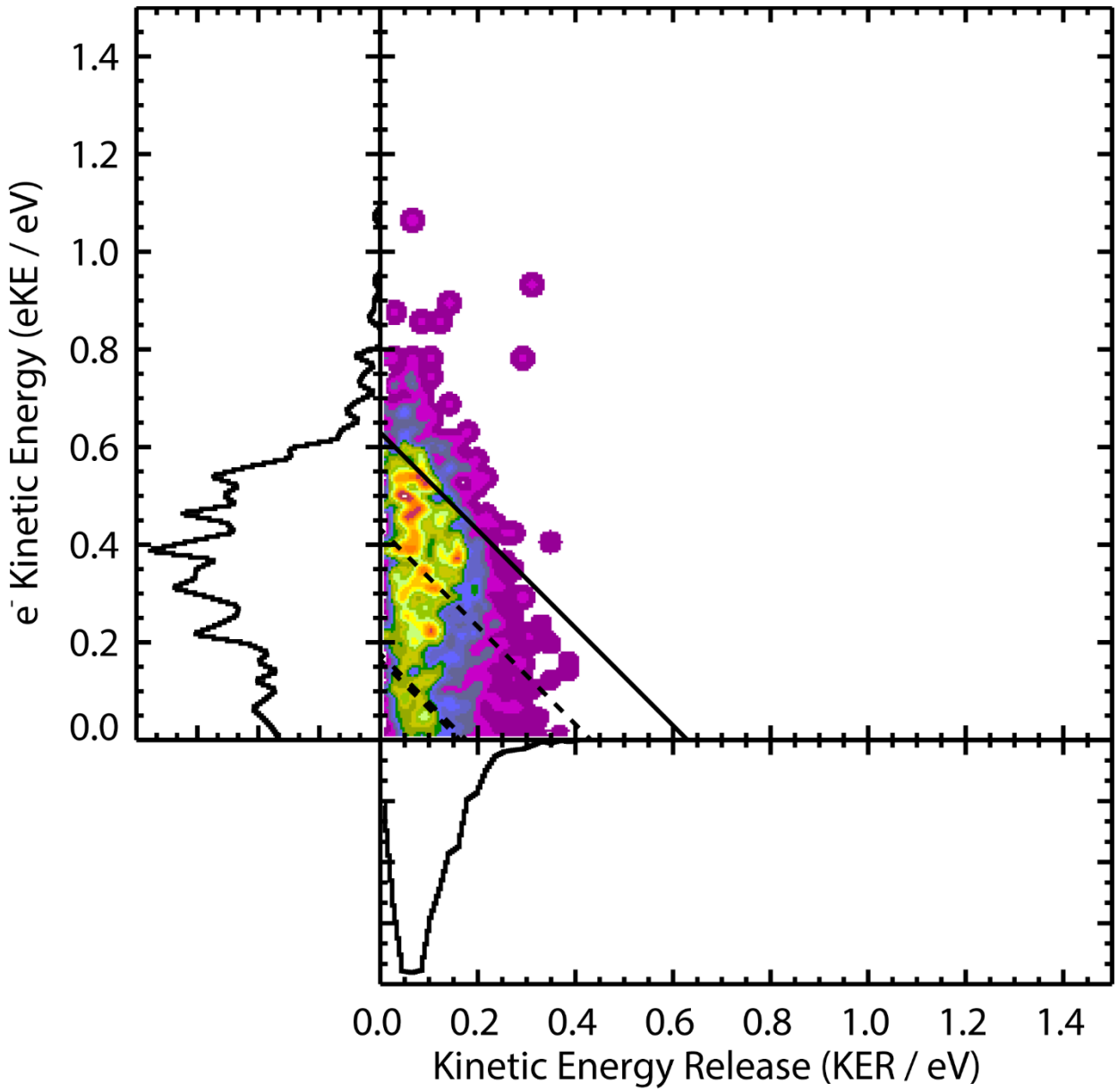

Figure 5.4. Photoelectron-Photofragment coincidence plot of DPD of $CH_3O^-(H_2O)$ at 3.20 eV photon energy. The solid diagonal line is the KE_{max} for $H_2O + CH_3O + e^-$ product channel. The dashed diagonal lines at 0.43, 0.18, and 0.16 eV are KE_{max} for one quanta of excitation in the water bend, symmetric stretch, and asymmetric stretching modes.

conservation, and the diagonal lines in this plot represent the kinetic energy maxima (KE_{max}) for a given channel. The KE_{max} limits are obtained from the computed energetics, shown in Figure 5.1., demonstrating good overall agreement with the experimental observations confirming the dominant channel accessed are the H_2O (ν_1, ν_2, ν_3 | v=0,1) + CH_3O + e^- products. The mass ratio of the photofragments can be examined in a center-of-mass spectrum, shown in Figure 5.5., supporting the production of fragment masses 18 and 31 amu. However, it should be noted that channels differing by 1 amu such as the OH + CH_3OH channel, cannot be resolved in this study due to the limited center-of-mass resolution. The dashed diagonal lines at 0.43 and 0.45-0.47 eV correspond to excitation in the water bending, ν_2, and local symmetric stretching, ν_1, and asymmetric stretching, ν_3, modes of the water products, respectively.[39] The free water product has an O—H bond length and H-O-H angle which differs from the corresponding configuration of the precursor anion by -0.1 Å and +3.3°, respectively, so excitation of these modes is expected. Another view of the coincidence plot with the same KE_{max} limits is a total energy spectrum, where E_{TOT} = eKE + KER on an event-by-event basis. In this spectrum, diagonal structure will appear as peaks or sharp cutoffs, as seen in Figure 5.6. The feature at low kinetic energies can be seen more clearly in this figure corresponding to excitation in the symmetric and asymmetric stretching modes of water products. Previous studies on the analogue reaction F + CH_3OH,[37, 38] found that excitation was primarily partitioned in the HF product with the methoxy radical playing the role of a spectator with 2% of available energy going towards vibrational excitation in the ν_3 C-O stretching mode of CH_3O.[40] This assumption is also made here and is supported in this study by the small conformational changes in geometry of the free methoxy product and the methoxy moiety in the anion.[41] The entrance channel is near threshold (KE_{max} = 0.02 eV) and is not accessed in this study.

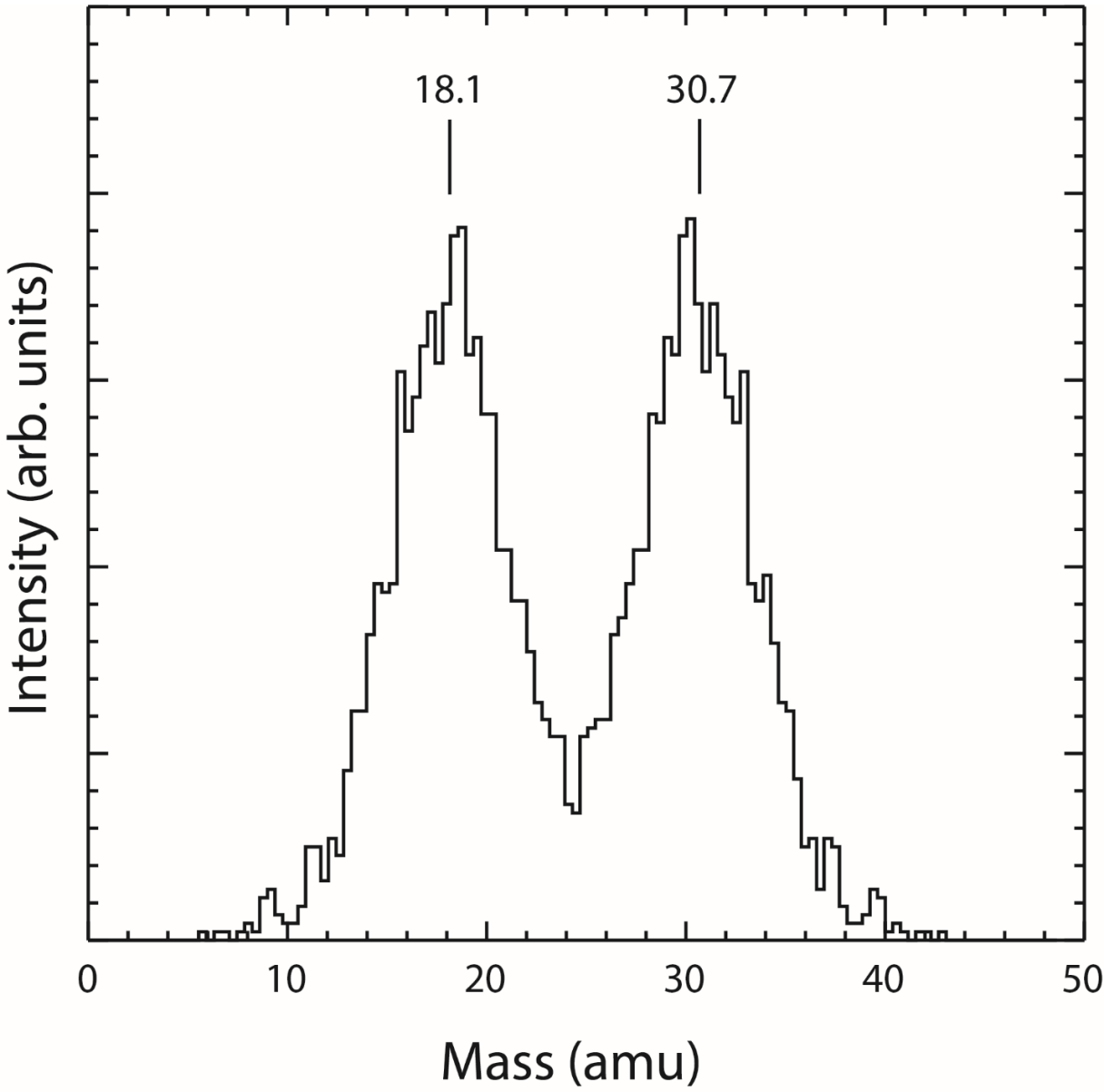

Figure 5.5. Center of mass spectrum for 2-momentum matched photofragments, OH (18 amu) + CH_3O (31 amu).

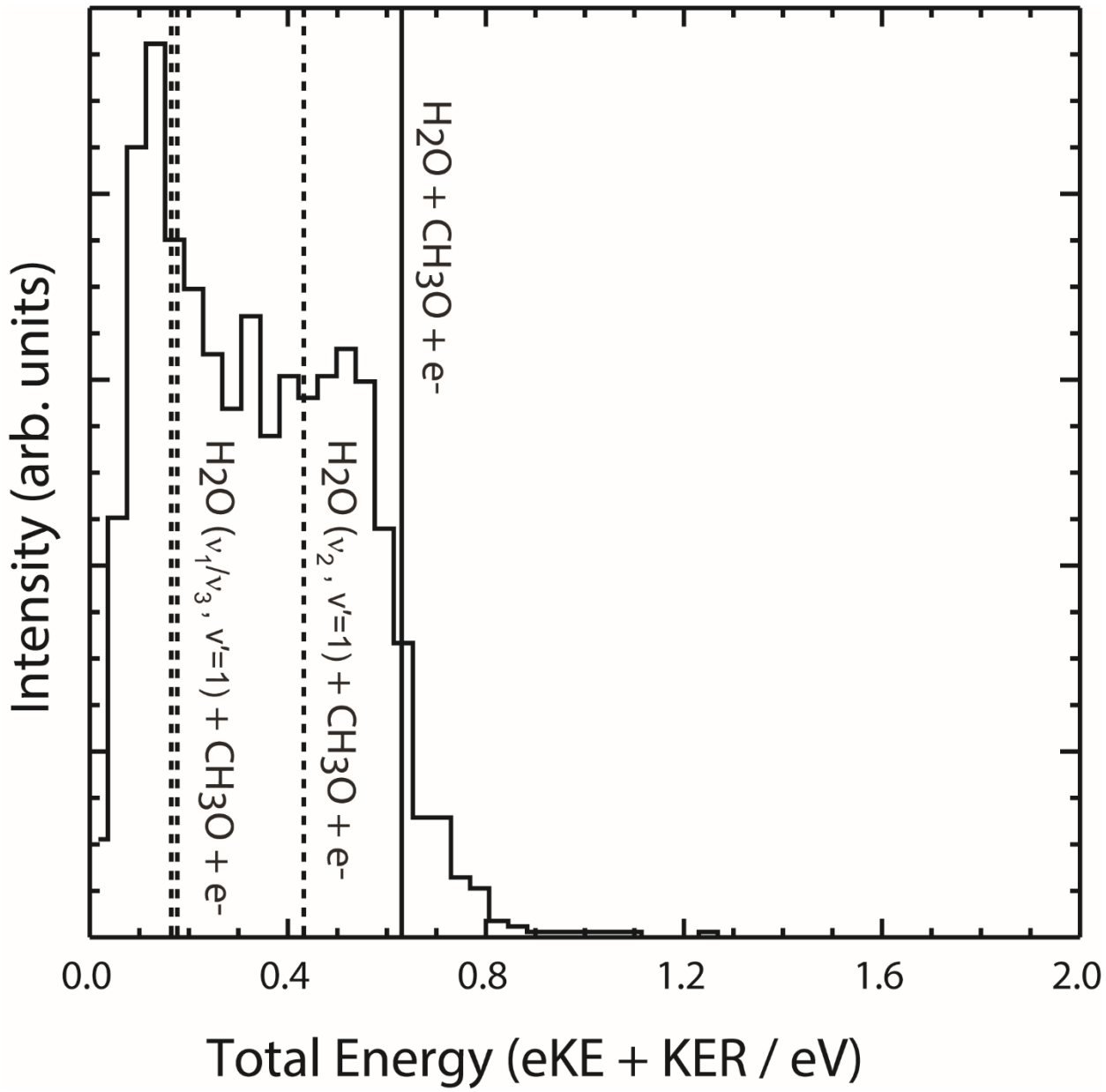

Figure 5.6. Total energy spectrum, eKE + KER, for dissociative photodetachment of $CH_3O^-(H_2O)$.

5.5. Summary

The dissociation dynamics of $CH_3O^-(H_2O)$ at 3.20 eV photon energy yielded both direct and resonance-mediated mechanisms to vibrationally excited $H_2O + CH_3O + e^-$ products with the dominant channel being DPD to the vibrational ground states of $H_2O + CH_3O + e^-$ products.

Our interpretation of our data is similar to analogous previous studies of hydroxyl radical reactions[36] and the reaction of $F + CH_3OH$.[37] The overall agreement between experimental observations and the computed energetics helped in aiding the analysis of the dissociation dynamics evolving on the neutral PES upon photodetachment of the precursor anion, in particular the confirmation that the wavefunction for the anion has overlap with configurations ranging from TS2 to the exit-channel complex well on the neutral surface. The entrance channel complex, or pre-reactive complex, for the title reaction has been studied extensively and has been shown to be significant in the forward reaction dynamics.[2] Although the present study does not probe this pre-reactive complex, the exit-channel complex was found to be important in the dissociation dynamics occurring on the exit channel and indicates that there may be a role for vibrationally excited Feshbach resonances in the bimolecular reactions of methoxy radicals. This system of 18 degrees of freedom represents a benchmark for studying increasingly complex reactions of this type. Considering the difficulty in full quantum dynamical simulations for this large system, the high-level coupled-cluster calculations performed here on both the neutral and anion potential energy surface, provide the first significant insights into the DPD of $CH_3O^-(H_2O)$ and the dissociation dynamics of $CH_3O(H_2O)$.

Acknowledgements

This material is based on work supported by the U.S. Department of Energy, Office of Science, Office of Basic Energy Sciences under Award Number DE-FG03-98ER14879.

Chapter 5 is in preparation for publication: Benitez, Y.; Nguyen, T. L.; Parsons, A. J.; Stanton, J. F.; Continetti, R. E., Probing the Exit Channel of the OH + CH_3OH → H_2O + CH_3O Reaction by Photodetachment of $CH_3O^-(H_2O)$ Complex. The dissertation author is the primary author. The corresponding author is the dissertation advisor, R. E. Continetti.

5.6. References

1. Shannon, R. J.; Blitz, M. A.; Goddard, A.; Heard, D. E., Accelerated chemistry in the reaction between the hydroxyl radical and methanol at interstellar temperatures facilitated by tunnelling. *Nature Chemistry* **2013,** *5* (9), 745-749.

2. Canosa, A., Gas phase reaction kinetics of complex organic molecules at temperatures of the interstellar medium: The OH + CH_3OH case. *Proceedings of the International Astronomical Union* **2019,** *15* (S350), 35-40.

3. Inostroza-Pino, N.; Mardones, D.; Ge, J. J. X.; MacLeod-Carey, D., Formation pathways of complex organic molecules: OH• projectile colliding with methanol ice mantle $(CH_3OH)_{10}$. *A&A* **2020,** *641*.

4. McCaulley, J. A.; Kelly, N.; Golde, M. F.; Kaufman, F., Kinetic studies of the reactions of atomic fluorine and hydroxyl radical with methanol. *The Journal of Physical Chemistry* **1989,** *93* (3), 1014-1018.

5. Zaczek, L. T.; Lam, K. Y.; Davidson, D. F.; Hanson, R. K., A shock tube study of CH_3OH+OH→Products using OH laser absorption. *Proceedings of the Combustion Institute* **2015,** *35* (1), 377-384.

6. Ocaña, A. J.; Blázquez, S.; Potapov, A.; Ballesteros, B.; Canosa, A.; Antiñolo, M.; Vereecken, L.; Albaladejo, J.; Jiménez, E., Gas-phase reactivity of CH_3OH toward OH at interstellar temperatures (11.7–177.5 K): experimental and theoretical study. *Physical Chemistry Chemical Physics* **2019,** *21* (13), 6942-6957.

7. Chao, W.; Jr-Min Lin, J.; Takahashi, K.; Tomas, A.; Yu, L.; Kajii, Y.; Batut, S.; Schoemaecker, C.; Fittschen, C., Water Vapor Does Not Catalyze the Reaction between Methanol and OH Radicals. *Angewandte Chemie International Edition* **2019,** *58* (15), 5013-5017.

8. Xu, S.; Lin, M. C., Theoretical study on the kinetics for OH reactions with CH_3OH and C_2H_5OH. *Proceedings of the Combustion Institute* **2007,** *31* (1), 159-166.

9. Gao, L. G.; Zheng, J.; Fernández-Ramos, A.; Truhlar, D. G.; Xu, X., Kinetics of the Methanol Reaction with OH at Interstellar, Atmospheric, and Combustion Temperatures. *Journal of the American Chemical Society* **2018,** *140* (8), 2906-2918.

10. Roncero, O.; Zanchet, A.; Aguado, A., Low temperature reaction dynamics for CH_3OH + OH collisions on a new full dimensional potential energy surface. *Physical Chemistry Chemical Physics* **2018,** *20* (40), 25951-25958.

11. Naumkin, F.; del Mazo-Sevillano, P.; Aguado, A.; Suleimanov, Y. V.; Roncero, O., Zero- and High-Pressure Mechanisms in the Complex Forming Reactions of OH with Methanol and Formaldehyde at Low Temperatures. *ACS Earth and Space Chemistry* **2019,** *3* (7), 1158-1169.

12. Wu, J.; Gao, L. G.; Varga, Z.; Xu, X.; Ren, W.; Truhlar, D. G., Water Catalysis of the Reaction of Methanol with OH Radical in the Atmosphere is Negligible. *Angewandte Chemie International Edition* **2020,** *59* (27), 10826-10830.

13. Cooke, I. R.; Sims, I. R., Experimental Studies of Gas-Phase Reactivity in Relation to Complex Organic Molecules in Star-Forming Regions. *ACS Earth and Space Chemistry* **2019,** *3* (7), 1109-1134.

14. Nguyen, T. L.; Ruscic, B.; Stanton, J. F., A master equation simulation for the •OH + CH_3OH reaction. *The Journal of Chemical Physics* **2019,** *150* (8), 084105.

15. Acharyya, K.; Herbst, E.; Caravan, R. L.; Shannon, R. J.; Blitz, M. A.; Heard, D. E., The importance of OH radical–neutral low temperature tunnelling reactions in interstellar clouds using a new model. *Molecular Physics* **2015,** *113* (15-16), 2243-2254.

16. Balucani, N., Gas-Phase chemistry and molecular complexity in space: how far do they go? *Memorie della Societa Astronomica Italiana* **2019,** *90*.

17. Knewstubb, P. F.; Sugden, T. M., Mass-Spectrometric Observations of Negative Ions in Flame Gases. *Nature* **1962,** *196* (4861), 1311-1312.

18. Long, B.; Bao, J. L.; Truhlar, D. G., Kinetics of the Strongly Correlated CH_3O + O_2 Reaction: The Importance of Quadruple Excitations in Atmospheric and Combustion Chemistry. *Journal of the American Chemical Society* **2019,** *141* (1), 611-617.

19. Wei, M.-L.; Tan, X.-F.; Long, Z.-W.; Long, B., Atmospheric chemistry of CH3O: its unimolecular reaction and reactions with H_2O, NH_3, and HF. *RSC Advances* **2017,** *7* (89), 56211-56219.

20. Buszek, R. J.; Sinha, A.; Francisco, J. S., The Isomerization of Methoxy Radical: Intramolecular Hydrogen Atom Transfer Mediated through Acid Catalysis. *Journal of the American Chemical Society* **2011,** *133* (7), 2013-2015.

21. Meot-Ner, M., Multicomponent cluster ions. 2. Comparative stabilities of cationic and anionic hydrogen-bonded networks. Mixed clusters of water-methanol. *Journal of the American Chemical Society* **1986,** *108* (20), 6189-6197.

22. Meot-Ner, M.; Sieck, L. W., Relative acidities of water and methanol and the stabilities of the dimer anions. *The Journal of Physical Chemistry* **1986,** *90* (25), 6687-6690.

23. Chabinyc, M. L.; Craig, S. L.; Regan, C. K.; Brauman, J. I., Gas-Phase Ionic Reactions: Dynamics and Mechanism of Nucleophilic Displacements. *Science* **1998,** *279* (5358), 1882.

24. Xie, J.; Otto, R.; Wester, R.; Hase, W. L., Chemical dynamics simulations of the monohydrated $OH^-(H_2O)$ + CH_3I reaction. Atomic-level mechanisms and comparison with experiment. *The Journal of Chemical Physics* **2015,** *142* (24), 244308.

25. Jing, X.; Michael, J. S.; William, L. H.; Peter, M. H.; Albert, A. V., Determination of the Temperature-Dependent $OH^-(H_2O)$ + CH_3I Rate Constant by Experiment and Simulation. *Zeitschrift für Physikalische Chemie* **2015,** *229* (10-12), 1747-1763.

26. Continetti, R. E.; Guo, H., Dynamics of transient species via anion photodetachment. *Chem. Soc. Rev.* **2017,** *46* (24), 7650-7667.

27. Continetti, R. E., Coincidence Spectroscopy. *Annu. Rev. Phys. Chem.* **2001,** *52* (1), 165-192.

28. Johnson, C. J.; Shen, B. B.; Poad, B. L. J.; Continetti, R. E., Photoelectron-photofragment coincidence spectroscopy in a cryogenically cooled linear electrostatic ion beam trap. *Rev. Sci. Instrum.* **2011,** *82* (10), 105105.

29. Shen, B. B.; Benitez, Y.; Lunny, K. G.; Continetti, R. E., Internal energy dependence of the photodissociation dynamics of O_3^- using cryogenic photoelectron-photofragment coincidence spectroscopy. *J. Chem. Phys.* **2017,** *147* (9), 094307.

30. Wiley, W. C.; McLaren, I. H., Time-of-Flight Mass Spectrometer with Improved Resolution. *Rev. Sci. Instrum.* **1955,** *26* (12), 1150-1157.

31. Hanold, K. A.; Continetti, R. E., Photoelectron–photofragment coincidence studies of the dissociative photodetachment of O_4^-. *Chem. Phys.* **1998,** *239* (1), 493-509.

32. Thorpe, J. H.; Lopez, C. A.; Nguyen, T. L.; Baraban, J. H.; Bross, D. H.; Ruscic, B.; Stanton, J. F., High-accuracy extrapolated ab initio thermochemistry. IV. A modified recipe for computational efficiency. *J Chem Phys* **2019,** *150* (22).

33. Dunning, T. H., Gaussian-Basis Sets for Use in Correlated Molecular Calculations .1. The Atoms Boron through Neon and Hydrogen. *J Chem Phys* **1989,** *90* (2), 1007-1023.

34. Mills, I. M., Vibration-Rotation Structure in Asymmetric- and Symmetric-Top Molecules. In Molecular Spectroscopy: Modern Research; Rao, K. N.; Mathews, C. W., Ed.; Academic Press: New York. **1972,** *Vol. 1*, 115.

35. Ruscic, B.; Bross, D. H. Active Thermochemical Tables (ATcT) values based on ver. 1.122d of the Thermochemical Network (2018), available at ATcT.anl.gov.

36. Benitez, Y.; Lu, D.; Lunny, K. G.; Li, J.; Guo, H.; Continetti, R. E., Photoelectron–Photofragment Coincidence Studies on the Dissociation Dynamics of the OH–CH_4 Complex. *J. Phys. Chem. A* **2019,** *123* (23), 4825-4833.

37. Ray, A. W.; Agarwal, J.; Shen, B. B.; Schaefer, H. F.; Continetti, R. E., Energetics and transition-state dynamics of the F + $HOCH_3$ → HF + OCH_3 reaction. *Phys. Chem. Chem. Phys.* **2016,** *18* (44), 30612-30621.

38. Bradforth, S. E.; Arnold, D. W.; Metz, R. B.; Weaver, A.; Neumark, D. M., Spectroscopy of the transition state: hydrogen abstraction reactions of fluorine. *The Journal of Physical Chemistry* **1991,** *95* (21), 8066-8078.

39. Shimanouchi, T., Tables of Molecular Vibrational Frequencies Consolidated Volume I. National Bureau of Standards: 1972; pp 1-160.

40. Agrawalla, B. S.; Setser, D. W., Infrared chemiluminescence and laser-induced fluorescence studies of energy disposal by reactions of F and Cl atoms with H_2S (D_2S), H_2Se, H_2O (D_2O), and CH_3OH. *Journal of Physical Chemistry* **1986,** *90* (11), 2450-2462.

41. Herzberg, G., *Electronic spectra and electronic structure of polyatomic molecules*. Van Nostrand New York, 1966.

Appendix A: Construction of a Dual Pulsed Valve Setup

A.1. Operating Principle and System Design

A dual pulsed valve setup was constructed inspired by Lineberger's group[1] to synthesize precursor anion clusters. The dual pulsed valve setup operates by entrainment of a plasma generated in a side discharge into the high-density region of the primary supersonic expansion. This method has been found to generate vibrationally cold anions[1] and provides a rational approach to synthesizing anions of interest, particularly hydroxide cluster anions. In brief, a plasma is generated in a side expansion via an electrical discharge using a custom piezoelectric[2] pulsed valve to generate a molecular beam under low backing pressures (~20 psig). This plasma intersects the main molecular beam which has a higher backing pressure (40-50 psig) and higher driving voltages. The side expansion does not disrupt the main expansion so the cluster anions formed can proceed along the main expansion towards the Wiley-McLaren mass spectrometer to be extracted perpendicularly along the beam line. An example of this process is shown in Figure A.1. A typical timing diagram can be seen in Figure A.2. The side and main pulsed valves typically operate 520-460 μs and 520-380 μs, respectively, before the Wiley plates are pulsed. The discharge is typically triggered 300 μs before Wiley. It should be noted that the discharge was switched with a (insert Behlke switch here) with a fixed width. Future utilization of this source should switch to a variable width switch as this will add more range in generating precursor anions of interest. Additionally, a larger TMP with a higher pumping speed (>240 l/s) should also be used to ensure adequate beam densities for generating cluster anions of interest.

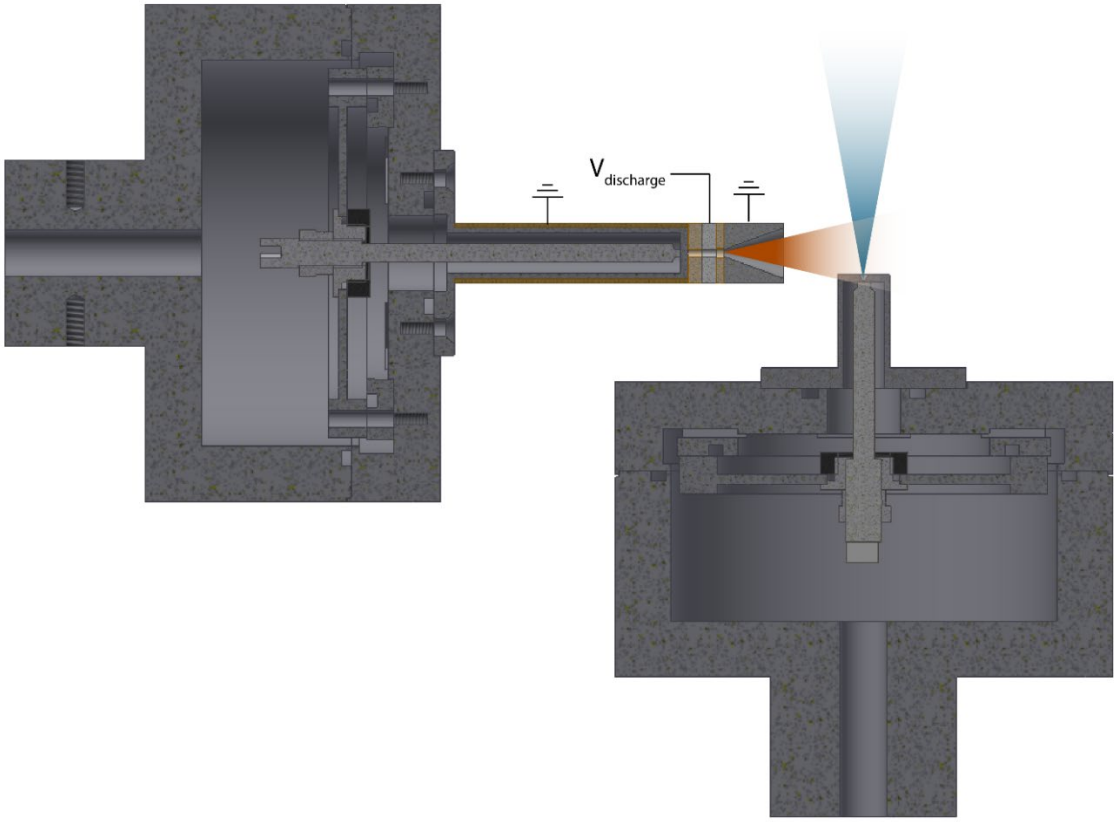

Figure A.1. Cross-sectional illustration of the dual pulsed valve setup. The dual pulsed valves operate independently. The side expansion (orange) intersects the high-density region of the main expansion (blue). The potential difference applied to the stainless steel (SS) plates can be reversed from that shown here. MACOR insulators separate the poppet nozzle and the first SS plate and the two SS plates. Typical discharge voltages are in the range 500-2000 V.

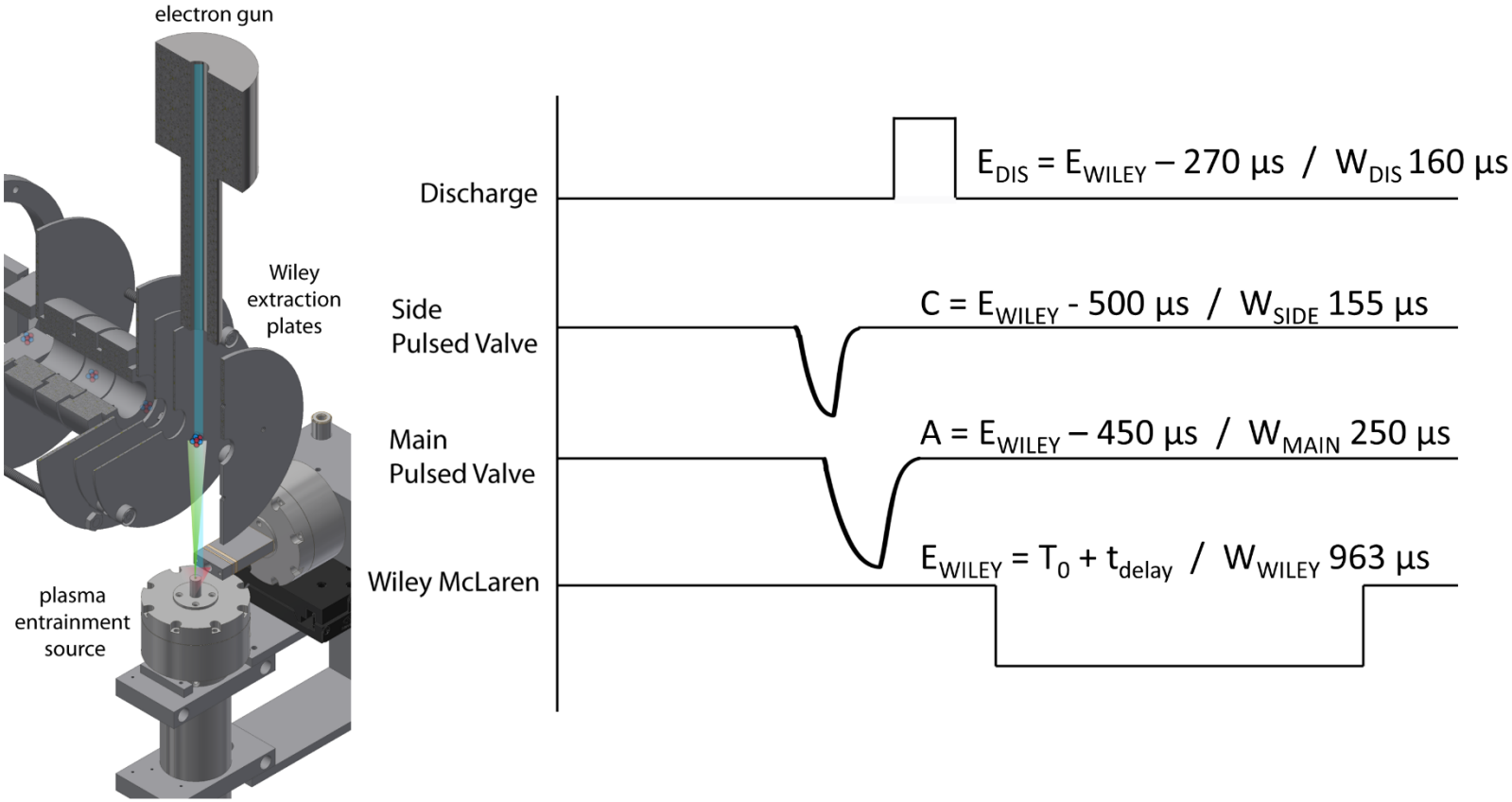

Figure A.2. Typical timing diagram for the dual pulsed valve along with an angled view of the dual pulsed valve setup for context. A Stanford research systems DG645 is triggered at 10 Hz by the scaled laser modelocking rep rate TTL, T_0. The SRS DG controls E_{WILEY}, A, and C channels. A Quantum composer DG 9518, triggered by the SRS, controls channel E_{Dis}. (t_{delay} is an experimental offset)

When using the dual pulsed valve, the main pulsed valve poppet is replaced with a longer poppet and poppet nozzle (as seen in Figure A.3.) and the side pulsed valve has a longer poppet and poppet nozzle so that the two beams can intersect at closer distances. The side pulsed valve is secured on the aluminum blocks that secure the main pulsed valve to the source chamber flange. The side pulsed valve is on a translation stage to allow optimization of the distance between the side pulsed valve poppet nozzle from the centerline of the main pulsed valve. The side pulsed valve is mounted on an aluminum block containing two 0.5 in. thru holes to slide over two optical posts secured on the translation stage. Two ¼-20 tapped holes are on each side of the 0.5 in. holes for securing the side pulsed valve height with set screws, allowing the translation parallel to the main pulsed valve beam line. A schematic of this can be seen in Figure A.3. The discharge plates are mounted on an aluminum block that slices onto the long poppet of the side discharge. A schematic and description of this discharge stack can be seen in Figure A.4.

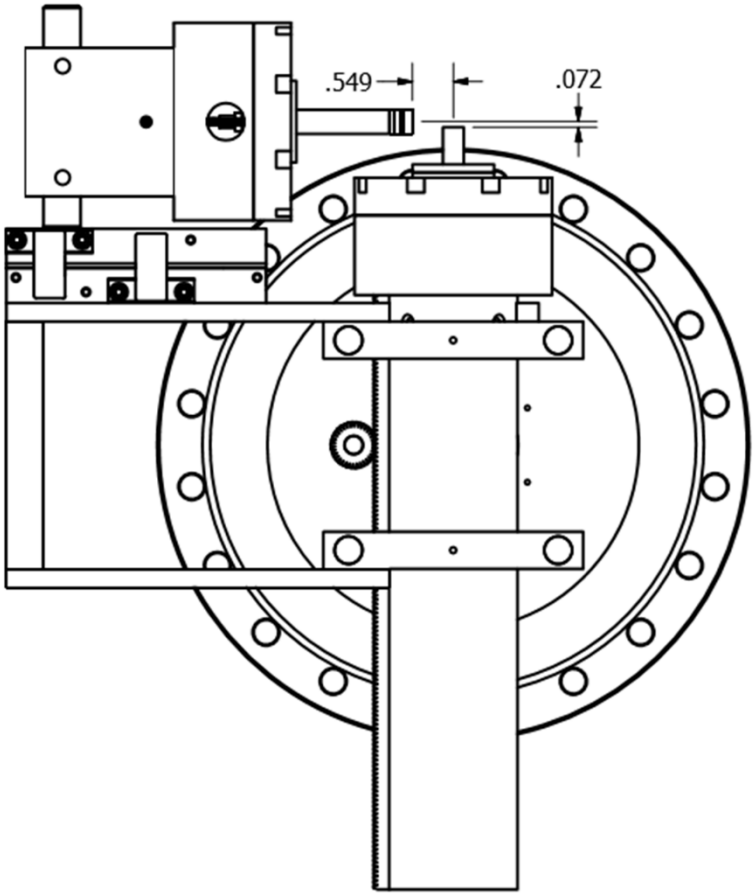

Figure A.3. Dual pulsed valve assembly. Relevant dimensions are reported in inches.

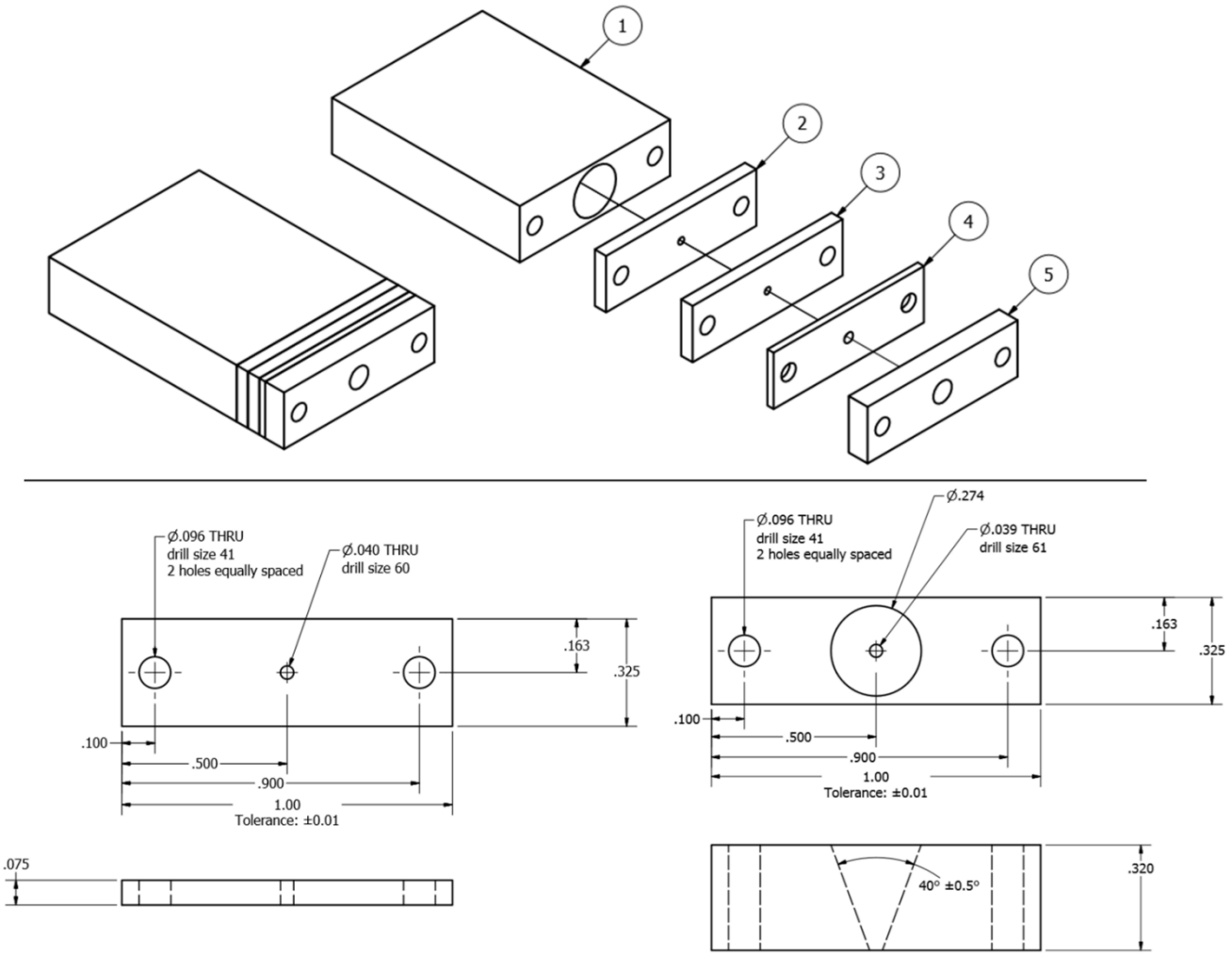

Figure A.4. Discharge assembly for side discharge. 1) aluminum block mount for discharge plates. 2) and 4) are thick and thin MACOR plates, respectively. 3) thin stainless steel electrode plate typically help at potential. 5) conical discharge plate typically held at ground. The bottom left and bottom right drawings show the thin SS electrode and the conical discharge plate electrode dimensions, respectively.

A.2. References

1. Lu, Y.-J.; Lehman, J. H.; Lineberger, W. C., A versatile, pulsed anion source utilizing plasma-entrainment: Characterization and applications. *J. Chem. Phys.* **2015,** *142* (4), 044201.

2. Proch, D.; Trickl, T., A high-intensity multi-purpose piezoelectric pulsed molecular beam source. *Review of Scientific Instruments* **1989,** *60* (4), 713-716.

Appendix B: Interlock for Machine C

Replacement of the Edwards turbomolecular pumps for the COAT, accel, and TOF chambers with Osaka TMPS required some minor changes to the pre-existing interlock logic. This appendix outlines those changes and provides an overview of the interlock logic as it relates to the Osaka TMPs for COAT, accel, and TOF chambers.

B.1. Interlock Logic for Integration of Osaka Turbomolecular Pumps

The TOF (Osaka TG900M) and Accel (Osaka TG2400MBWB) TMPs, used the same controller (Osaka TC010M) and did not require any changes to the interlock logic in place for the Edwards controllers for the replaced TMPs. The interlock logic for these TMPs can be seen in Figure B.1. Brief descriptions under different operations are as follow:

Under normal operating conditions: The backing pressure is low enough, relay A is actuated (closed) causing 3 and 5 to be connected. +24 VDC will then be sent to pin 5 on the D-sub 37 connector which goes to the Edwards controller. When pin 5 and pin 6 are closed, the pump is in normal operation and +24 VDC will be sent to the enable switch via pin 6. When enable switch is switched, this supplies +24 VDC to the coil in relay B. This actuates relay B, and 3 and 5 are connected—this is a protection signal to the controller via pins 33 and 34. On Relay B, 4 and 6 are also connected which keeps the FLV open between the backing pump and the respective chamber (TOF/Accel/COAT chambers are not separated by gate valves).

If backing pressure rises above set point pressure while everything else running under normal conditions: Relay A will not actuate as there will be no ground provided to A. This will cause the relay to open, thus 3 and 5 will no longer be connected. This will interrupt the +24 VDC supplied to the Edwards controller via pin 5. As a result, + 24 VDC will not be sent back to relay

B, causing relay B to open. This results in the FLVs to close since 4 is no longer connected to 6. 3 and 5 are also no longer connected causing pin 33 and pin 34 to open. When these pins are open while the pump is in rotation, the pump will stop.

If backing pressure ok but normal out not ok: The backing pressure is low enough, relay A is actuated (closed) causing 3 and 5 to be connected. +24 VDC will then be sent to pin 5 on the D-sub 37 connector which goes to the Edwards controller. Pin 5 and pin 6 will open caused by the controller. This will disrupt the +24 VDC supplied via pin 5 and it will not be sent back to relay B (via pin 6) causing that relay to open. This results in the FLVs to close since 4 is no longer connected to 6. 3 and 5 are also no longer connected causing pins 33 and pin 34 to open. When these pins are open while the pump is in rotation, the pump will stop.

If at room pressure and need to pump down: All the relays will be open. Once the backing pressure falls $< 10^{-3}$ torr flip the backing override switch for TOF first. This causes +24 VDC to be supplied to the coil in relay B. As a result, 4 and 6 will be connected which supplies the power to the FLV. Now open the manual valve slowly leading to the chamber. Pump out the TOF, Accel, and COAT chamber in the same manner until the backing pressure is $< 10^{-3}$ torr. Switch the enable switch and manually turn on the TOF and accel controllers. Once the pumps have spun up and backing pressure is ok, everything should be under normal operating conditions (see above). Proceed to unoverride the backing override switch since it is no longer needed because pin 6 is supplying the + 24 VDC to relay B.

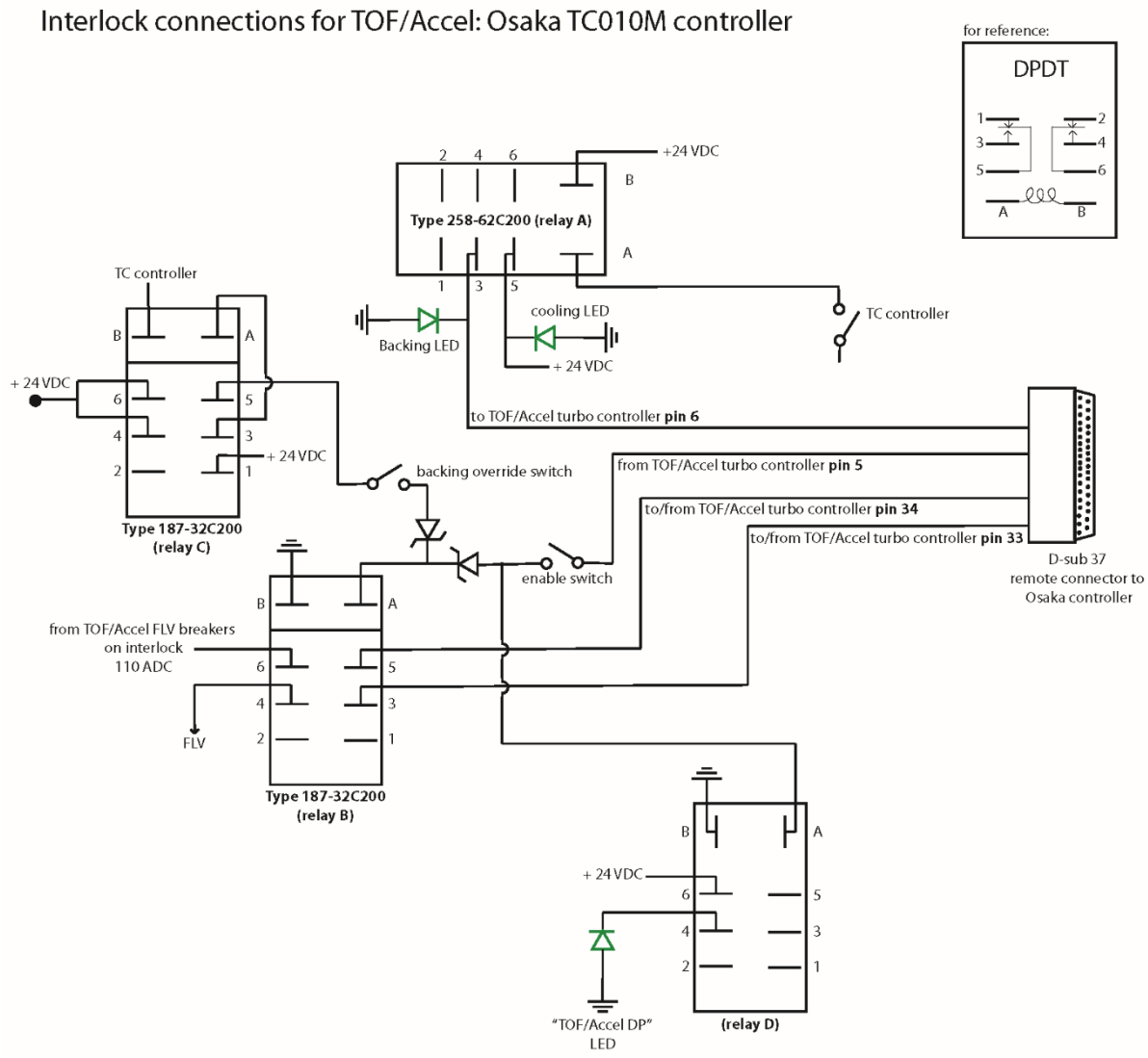

*When pin 5 and pin 6 are closed, pump is in normal operation.
*When pin 33 and pin 34 are set to open, the STP pump does not rotate. When these pins are set to open while pump is in rotation, the pump will stop.

Figure B.1. Interlock connections for TOF/Accel: TC010M controller

The interlock logic had to be modified to incorporate the COAT Osaka TMP which has a TGkine series integrated controller. A control circuit was included comprising of several MOSFETs for low power switching. A schematic of this logic can be seen in Figure B.2.

Under normal operating conditions: The backing pressure is low enough, relay A is actuated (closed) causing 3 and 5 to be connected. +24 VDC will then be sent to A on relay E. When the pump is in normal operation, pin 8 and pin 15 are at ground. Pin 15 is always at ground externally on the interlock. Pin 8 is the ground connection for the coil on relay E causing it to actuate. (The green LED in the control circuit is on during normal operation, if it is not on, inspect the control circuit.) This will connect 3 and 5 resulting in +24 VDC to be sent to the enable switch. When the enable switch is switched, this supplies +24 VDC to the coil in relay B. This actuates relay B, and 3 and 5 are connected. This sends +24 VDC via pin 1 to the D-sub 15 connector to the Osaka integrated controller. The potential across pin 1 and pin 15 is 24 V and the pump is spun up. On Relay B, 4 and 6 are also connected which keeps the FLV open between the backing pump and the respective chamber (TOF/Accel/COAT chambers are not separated by gate valves).

If backing pressure rises above set point pressure while everything else running under normal conditions: Relay A will not actuate as there will be no ground provided to A. This will cause the relay to open, thus 3 and 5 will no longer be connected. This will interrupt the +24 VDC supplied to the coil on relay E and causes 3 and 5 to not be connected. As a result, + 24 VDC will not be sent back to relay B, causing relay B to open. This results in the FLVs to close since 4 is no longer connected to 6. 3 and 5 are also no longer connected disrupting the + 24 VDC supply via pin 1 to the controller. When the potential across pins 1 and 15 drops from 24 V to 0 V, the pump will stop.

If backing pressure ok but normal out not ok: The backing pressure is low enough, relay A is actuated (closed) causing 3 and 5 to be connected. +24 VDC will then be sent to A on relay E. There will no longer be any continuity between pin 8 and 15 (opened on the controller end). This will disrupt the ground supplied to the coil at B on relay E. This causes the relay to open and 3 and 5 will no longer be connected. This disrupts the +24 VDC supply to relay B causing that relay to open. This results in the FLVs to close since 4 is no longer connected to 6. 3 and 5 on relay B are no longer connected disrupting the + 24 VDC supply via pin 1 to the controller. When the potential across pins 1 and 15 drops from 24 V to 0 V, the pump will stop.

If at room pressure and need to pump down: All the relays will be open. Once the backing pressure falls $< 10^{-3}$ torr flip the backing override switch for TOF first. This causes +24 VDC to be supplied to the coil in relay B. As a result, 4 and 6 will be connected which supplies the power to the FLV. Now open the manual valve slowly leading to the chamber. Pump out the tof and accel chamber in the same manner until the backing pressure is $< 10^{-3}$ torr. Switch the backing override for COAT (does not have a manual valve). Once the backing switch is switched it causes 24 VDC to be sent to relay B. This closes the relay and connects pins 4 and 6 as well as pins 3 and 5. This leads +24 VDC to be sent to the integrated controller via pin 1. As a result, this causes the pump to start. Switch the enable switch and manually turn on the tof and accel controllers. Once the pumps have spun up and backing pressure is ok, everything should be under normal operating conditions (see above). Proceed to unoverride the backing override switch since it is no longer needed because + 24 VDC is being supplied to relay B via relay E.

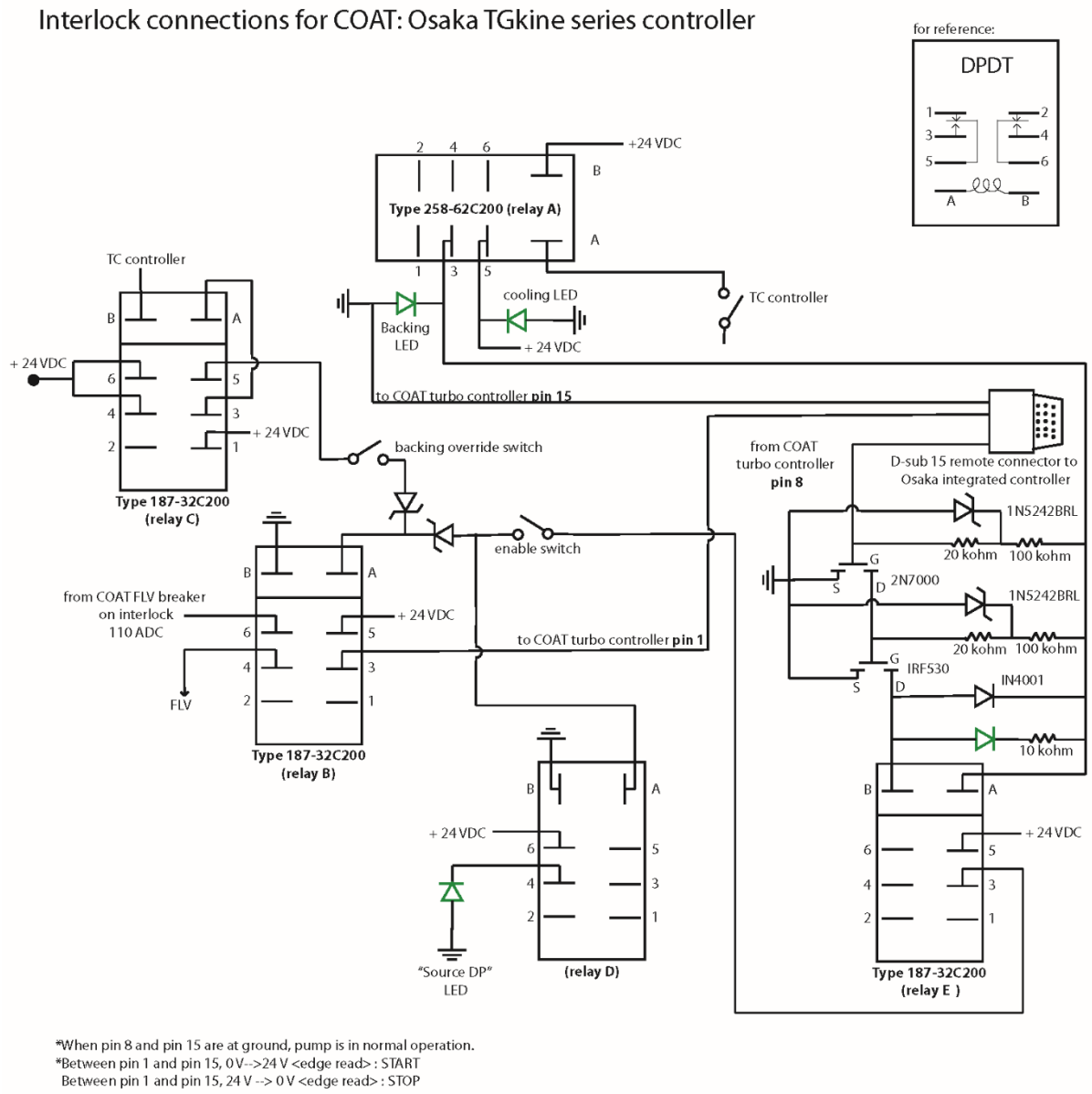

Figure B.2. Interlock connections for COAT: Osaka TGkine series controller